University of Alberta

Development of a Novel Electro-thermal Anti-icing System

for Fiber-reinforced Polymer Composite Airfoils

by

Maryam Mohseni

A thesis submitted to the Faculty of Graduate Studies and Research
in partial fulfillment of the requirements for the degree of

Master of Science

Mechanical Engineering

Fall 2012
Edmonton, Alberta

Abstract

Given the trend towards expanded use of polymeric composites for wind turbine blades and aircrafts wing, icing of polymer composite airfoils is a challenge; this thesis is addressing this issue from a conceptual perspective. For the first time, the concept of embedded thermal elements as an anti-icing system for polymer composite airfoils is investigated experimentally and numerically. A manufacturing technique was developed to implement the electro-thermal anti-icing system. Thermography was used to understand surface temperature distribution of the composite airfoil surface in cold (dry) and icing (wet) condition tests. The effect of thermal elements' spacing and input power on the airfoils' surface temperature distribution, and the effectiveness of the thermal elements' pattern for icing mitigation were studied. Also, a methodology based on IR image analysis was developed for obtaining simultaneous information about airfoils' temperature field and ice accretion; such information is imperative for energy efficient design of an anti-icing system.

Acknowledgments

I would like to express my greatest thanks to my supervisor, Prof. Alidad Amirfazli; for his guidance, patience, and constant support. I am very grateful for his invaluable contributions to my personal and professional development.

I would like to thank the Mechanical Engineering workshop staff, in particular: Bernie Faulkner and Rick Conrad who helped me with technical assistance and fabricating apparatus in the equipment setup. Also, I thank my labmates and friends for helpful comments, general encouragement, and interesting discussions, in particular: Sara Madani, Mina Karimi, Maninderjit Singh, Andrew Milne, Farchid Chini, and David Barona.

I would also like to thank Marcy Frioult for helping me with the experiments, figures, and image processing and Siobhan O'Connor for assisting with experiments.

Special thanks go to my parents Mitra and Ahmad Mohseni and my brothers Mehdi and Amir for their love, inspiration, and unconditional support all throughout my life. Also, my sincere appreciation is given to my husband Emad Geramian for his encouragement, continues support, and understanding which made all this possible.

Table of Contents

Page

List of Tables

Page

List of Figures

Page

List of Symbols, Nomenclature and Abbreviations

Name	Unit	Definition
IR	-	infrared
LWC	-	Liquid Water Content
VMD	-	Volumetric Median Diameter
$k_{c,11}$	[W/m.K]	Thermal conductivity of composite in longitudinal direction of fibers
$k_{c,22}$	[W/m.K]	Thermal conductivity of composite in perpendicular direction of fibers
k_p	[W/m.K]	Thermal conductivity of polymeric matrix
k_f	[W/m.K]	Thermal conductivity of fiber
V_f	%	Fiber volume fraction
W_f	-	Fiber weight fraction
m_f	[g]	Weight of fiber in a composite sample
m_c	[g]	Weight of composite sample
x, y	[m]	Position coordinates
T	[˚C]	Temperature of the composite flat plate
k_x	[W/m.K]	Thermal conductivity of the composite plate in *x* direction (fiber direction)
k_y	[W/m.K]	Thermal conductivity of the composite plate in *y* (transverse to fiber direction) direction
$\dot{Q}$	[W]	Thermal energy

S	[m]	Conduction shape factor of the composite plate
$R_{cond.}$	[˚C/W]	Conduction thermal resistance through the composite plate
$R_{conv.}$	[˚C/W]	Thermal resistance of convection on the top and bottom surfaces of the composite plate
q_x	[W/m^2]	Heat flux in *x* direction
q_y	[W/m^2]	Heat flux in *y* direction
h	[W/m^2.˚C]	Convection heat transfer coefficient
T_∞	[˚C]	Ambient room temperature
T_S	[˚C]	Surface temperature of the composite plate
Nu_{ave}	-	Average Nusselt Number over the entire plate
Nu_{stag}	-	Nusselt Number on the stagnation point of the cylinder, where φ=0
Nu_φ	-	local Nusselt Number around the periphery of the cylinder
Pr	-	Prandtl Number
Re_D	-	Reynolds Number of the cylinder with diameter of D
D	[m]	Cylinder diameter which the leading edge is replaced by
k	[W/m . K]	Thermal conductivity of the air

U	[m/s]	Airflow velocity outside the thermal boundary layer (free stream velocity)
s	[m]	The curvilinear length over the airfoil measured from stagnation point on the leading edge region
S	[m]	Total length of the circumference of leading edge region
Δs_i	[m]	Difference between curvilinear lengths of two consecutive points measured along the airfoil surface from stagnation point over the leading edge region
h_i	[W/m^2.˚C]	Local convection heat transfer coefficient of the selected points (i) on the leading edge surface
v	[kg/m . s]	Dynamic viscosity of the air
ρ_c	[g/cm^3]	Composite density
ρ_f	[g/cm^3]	Fiber density
ρ_m	[g/cm^3]	Resin (matrix) density
φ	[˚]	Angle of airflow direction hitting the cylinder and different points on the cylinder surface

1. Introduction

1.1 Background

Icing is a serious problem in aerodynamic structures such as aircrafts' wing and wind turbine blades. The accreted ice adversely affects the aerodynamic performance of an airfoil by changing the airfoil's shape and increasing its surface roughness.

Icing on aircraft disturbs the smooth air flow, increasing the drag, and decreasing the lift [1, 2]. Sharp components such as thin leading edges gather ice more readily than blunt components, so aircrafts' wing is a susceptible part to ice accumulation [1].

Ice accretion on wind turbine blades reduces the torque and aerodynamic efficiency; and even a light ice can create sufficient surface roughness to increase the drag coefficient, reducing the power production. The change of drag to lift ratio decreases the efficient power production. Also, ice accumulation increases the blade's weight and changes the mass distribution along the airfoil. The increased weight and mass imbalance cause additional loading and vibration which decrease the fatigue life of the blade and can pose a serious safety issue [3-5].

Polymer composite materials are now widely used in aerodynamic structures such as wind turbine blades and aircrafts' wing to reduce their weight, manufacturing and maintenance costs and improve performance [6]. Polymer composite aerodynamic

structures suffer from icing similar to metal structures. As such, it is necessary to develop a proper icing mitigation system for polymer composite airfoils.

In this thesis a novel electro-thermal anti-icing system was developed for an aircraft grade polymer composite airfoil. The main idea was to embed tailor made discrete thermal elements in polymeric composite laminates for icing protection. Work needed to be done to understand temperature distribution at the surface, i.e. thermal characterization, thermal element design/pattern, fabrication techniques, as well as testing and quantifying energy consumption. This concept was studied experimentally, and numerically. Also, using the established image analysis methods, a novel methodology was developed based on IR imaging for simultaneous monitoring of ice accretion and thermography of airfoils. The main subject of this research is a thermal study of the composite airfoil with the anti-icing system, and issues related to mechanical strength, system reliability, induced thermal stresses, etc. are not considered within the scope of this thesis.

This chapter presents the necessary background for better understanding of this thesis; a general description of polymer composite materials, traditional icing mitigation techniques, especially anti-icing systems, and their application for composite materials, and a literature review about especially developed anti-icing systems for polymeric composites are presented. Also, thermal conductivity and thermal modeling of fiber-reinforced polymer composites, which are used in this thesis, are generally described. In the last part, the specific objectives and the scope of this thesis are provided.

1.2 Icing Mitigation Systems

Over the years, a number of in-flight icing mitigation techniques have been developed for aircraft and aerospace industry and are categorized as anti-icing and de-icing systems [2, 3, 7]. The icing mitigation techniques of the wind turbine blades are also derived from those developed for the aircraft industry.

De-icing is a process to remove the ice from the structure after formation to provide a clean surface [1]. There are various methods for de-icing, including pneumatic boots, thermal and chemical techniques using heating systems and chemical fluids for ice removal, respectively [1, 3]. The methods stated are mainly for in-flight de-icing; the topic of on-ground de-icing is a separate domain, mainly handled by spraying warm de-icer fluid.

In-flight anti-icing systems prevent the formation of ice or frost for a limited period of time, and they are activated before entering the icing conditions to prevent the adhesion of ice to the airfoil surface [1]. Anti-icing systems are mainly categorized into two methods: passive and active. Passive anti-icing systems such as black paint and so-called "ice-phobic" and superhydrophobic coatings do not require energy supply for ice removal. These coatings have non-wetting properties which prevent ice from sticking to the surface and do not allow water to remain on the surface [7, 8]. In practice, these coatings cannot prevent icing completely, and a combination of coatings and active anti-icing systems should be used for preventing ice accretion [9]. Active Anti-icing systems require an energy supply, and mainly categorized into three types of anti-icing systems

including chemical system, hot-air system, and electrical resistance heating (electro-thermal) system [2].

In chemical systems, which a liquid with low freezing point is used, an extra weight is posed to the airfoil; so, it is not a viable option for light-weight polymer composite airfoils [2, 7]. Thermal anti-icing systems including hot-air and electro-thermal systems should provide enough energy to maintain the surface temperature of a structure above freezing and also melt the ice formed at impact of supercooled water drops [8].

Hot-air systems are the most prevalent thermal anti-icing systems for conventional aircrafts wings. In hot-air systems, hot bleed air is ducted from the compressor of the engine to the wings through piccolo tubes (narrow gas passages) to transfer thermal energy to the surface and thus heat the wing surface [3]. This is a highly reliable and well developed technology for the conventional aircraft wings. But, it uses a large amount of fuel due to the volumetric flow of hot air which adversely affects the aircraft efficiency [2]. Use of hot-air inside the polymer composite airfoils can be challenging due to maximum operating temperature, low thermal conductivity and high thermal resistance of the polymer composites which pose a temperature limit for the hot air [4, 10, 11-14]. In wind turbine blade, the fiber reinforced polymer composite materials are good insulators, and as the size and thickness of the blades increase, more heat required to be pushed and transferred through the surface [4]. This will also increase the power consumption of the anti-icing system.

Ciardullo *et al.* [14] developed a method for heating the surface of the composite structures using hot-air as an anti-icing system. The concept involves conducting hot air through embedded glass capillary tubes on the surface of the composite flat coupon rather than conducting heat through thick composite walls. Surface heating of composite coupons employing this method was investigated, but its energy consumption and its effect on surface roughness which can lead to increased aerodynamic drag, was not assessed. It was also neither implemented for a polymer composite airfoil profile, nor tested in icing conditions.

Electro-thermal anti-icing systems are simple methods and their response time is very short compared to hot air or chemical systems; however, the power consumption can be very high, especially for evaporating anti-icing [2]. Electrical resistance heating systems in aircraft industry are mostly used in the form of electro-thermal pads, which are mostly consists of several layers. Electro-thermal pads are applied onto the surface of a structure or as close as possible to the skin surface to heat the surface and prevent ice accretion [2, 15]. Different types of electro-thermal pad systems with various electrical heating elements such as metal foils, carbon fibers, and graphite fiber/epoxy composites have been developed for different structures [3, 11, 12, 16, 17].

Hung *et al.* [11] developed an electro-thermal pad made from graphite composite material in the form of flat coupons to be used as a surface electro-thermal heater. The heating element in this system was a graphite fiber/epoxy composite layer which was claimed to have high thermal and electrical conductivity. This system, which can be

formed on irregular surfaces, was found to have acceptable heating performance in room temperature tests, but it has not been tested in wind tunnel icing experiments. This heater has not being used for an airfoil's shape as well.

In wind turbine blades, electro-thermal anti-icing systems are used in the form of thermal pads, electrically heated foils, and metal and carbon fiber electrical heating elements on the composite blades' surface or laminated into the blades' structure [3]. These systems have serious drawbacks which limited their use as reliable anti-icing systems [3, 12, 17]. Since they are mostly mounted on the surface of the blade, they increase the surface roughness which changes the aerodynamic performance of the airfoil, and disturb the air flow around the blade. Also, metal and carbon heating elements can attract lighting strikes at the surface of the blade. Carbon fiber elements mounted to the blades near the surface has been used in 18 turbines at various sites, and performed well [3]. Carbon fibers as the thermal elements, which are positioned at the leading edge can also cause additional problems for polymer composite blades. In the case of mechanical load, some cracks may form in the heating elements, i.e. carbon fibers, due to high mechanical stress transferred to the fibers of the heating elements [3]. Carbon fibers have higher Young's modulus than fiberglass in the polymer composite turbine blade, so they bear a larger portion of the loads which leads to form cracks in the heating system [3, 4, 12]. Moreover, use of the thermal pads on the inner surface of the airfoil profile [5] , rather than on the airfoil's surface, consumes high amount of power as an anti-icing system due to low thermal conductivity and high thermal resistance of polymer composite materials.

Early works in Europe showed that in wind turbine blades, the required power for the currently used electro-thermal anti-icing systems equals to at least 25% of the turbine maximum power [3]. Recent woks claim that the required power for smaller commercial scale turbines ranges between 6% and 12% of the output power [3].

1.3 Polymer Composite Materials

Composite materials are consisting of two or more components. The constituents are mixed in such a way that they keep their individual properties in the mixture. Polymeric composite materials consist of a polymer as the matrix phase and fibers and/or particles as the reinforcement phase.

Polymeric composite materials are widely used in aircraft and wind turbine industries due to their high specific stiffness and strength compared to metals. This property allows producing lighter and stronger structures. Composite materials also provide the unique ability to tailor material's properties considering the required mechanical, thermal or electrical properties. So the local strength, stiffness, thermal conductivity, and other properties of the component can be tailored [18]. Also, they can be shaped into the desired profile.

In fiber-reinforced polymer composite materials, fibers as the reinforcement phase increase the strength, dimensional stability and thermal properties of the composite. The main role of the polymer phase is transferring the load to the fibers, holding the fibers and also carrying transverse and shear loads [19].

Polymer composites are categorized as orthotropic materials which is a subclass of anisotropic materials. Composites as orthotropic materials have different thermal and mechanical properties in three mutually perpendicular directions.

The most common manufacturing methods for fiber-reinforced polymer composites are hand lay-up (wet lay-up and dry lay-up), spray-up, compression and resin transfer molding (RTM), pultrusion and filament winding. The manufacturing method is selected based on the reinforcement type, the shape of the final composite structure, quality and the required properties of the structure and production rate [19].

Most of polymer composite materials used in aircraft and wind turbine industries are made of glass or carbon fibers with a thermoset resin. Glass fiber/epoxy resin (GFRP) and carbon fiber/epoxy resin (CFRP) composites are mainly used in aircrafts' components. While, glass-fiber/polyester resin composites are mainly used in wind turbine blades due to its low cost [19]. These materials are commercially available in the form of prepregs which are pre-impregnated reinforcing fibers with a partially cured polymer matrix resin. Prepregs are in the form of sheets which can readily be applied to make the structure; hence, experimental uncertainties due to composite sample fabrication will be minimized. The manufacturing method in using prepregs is dry lay-up, in which a specific number of prepreg sheets are cut and laid up into the mold to shape the structure profile.

Conventional glass-fiber/epoxy or polyester resin composite materials have low thermal conductivity, and specific thermal stability (defined as the maximum operating temperature). Thermal characteristics of polymer composite materials including their thermal conductivity and thermal stability depend upon the type of the polymer as the matrix phase and fiber fraction in the composite [20]. Thermal stability increases with increasing glass transition temperature (Tg) of the polymer matrix [10]. Carbon fibers and glass fibers have higher thermal stability than resins, i.e. matrix phase; so composites with higher fiber fraction show higher thermal stability based on the rule of mixture in composite materials [20].

1.4 Thermal Conductivity of Fiber-Reinforced Polymer Composites

Thermal conductivity of fibrous composites depends on the thermal conductivities of fiber and matrix, fiber orientation, fiber volume fraction in the composite, heat flow direction and temperature [21]. Thermal conductivity in fiber-glass reinforced polymer composites is relatively low as 0.14-1.2W/m.K [6, 10, 22].

Since composite materials are orthotropic, two main thermal conductivities in longitudinal and transverse direction of fibers are measured. Longitudinal and transverse thermal conductivities give the upper and lower bounds of thermal conductivity of the composite material.

Analytical approach for predicting composites thermal conductivity presents generalized equations for a two-dimensional steady-state heat flow. Analytical models for predicting

thermal conductivity are mostly developed for unidirectional fiber reinforced composites, considering glass fiber and resin as isotropic materials. The rule of mixtures is a simple and general model to predict the longitudinal thermal conductivity of unidirectional composites [23]:

$$k_{c,11} = V_f.k_f + \left(1 - V_f\right).k_p \quad (1)$$

where, $k_{c,11}$ is thermal conductivity of composite in longitudinal direction of fibers, k_p is thermal conductivity of polymeric matrix, k_f is thermal conductivity of fiber, and V_f is fiber volume fraction in the composite.

There are also several analytical models as described in [23, 24] for predicting transverse thermal conductivity of polymeric composites such as Rayleigh, Halpin-Tsai, Springer and Tsai, Hatta and Taya , Brennan *et al.* , Hashin, Cheng and Vachon, etc.. It is shown that Rayleigh, Springer and Tsai and Halpin-Tsai models predict transverse thermal conductivity with a good accuracy of ±2% [23]. We have used these theoretical models as given by [18, 23]:

Reyleigh model:

$$k_{c,22} = k_p \left[1 - \frac{2\varphi}{\gamma + \varphi - \frac{C_1}{\gamma}\varphi^4 - \frac{C_2}{\gamma}\varphi^8}\right] \quad (2)$$

where, $C_1 = 0.305$, $C_2 = 0.0134$,

$$\gamma = \frac{\left(\frac{k_p}{k_f}\right) + 1}{\left(\frac{k_p}{k_f}\right) - 1}$$

Springer and Tsai model:

$$k_{c,22} = k_p \left[1 - 2\sqrt{\frac{\varphi}{\pi}} + \frac{1}{B}\left(\pi - \frac{4}{\sqrt{1 - (\frac{B^2\varphi}{\pi})}} tan^{-1}\left(\frac{\sqrt{1 - (\frac{B^2\varphi}{\pi})}}{1 + B\sqrt{\frac{\varphi}{\pi}}}\right)\right)\right] \quad (3)$$

where,

$$B = 2\left(\frac{k_p}{k_f} - 1\right)$$

Halpin-Tsai model:

$$k_{c,22} = k_p \left[\frac{1 + \xi\varphi\eta}{1 - \eta\varphi}\right] \quad (4)$$

where, for circular or square reinforcement fibers $\xi = 1$, and

$$\eta = \frac{\frac{k_f}{k_p} - 1}{\frac{k_f}{k_p} + \xi}$$

1.5 Thermal Modeling of Embedded Heating Elements in a Polymer Composite Laminate

As mentioned earlier, fiber reinforced polymer composites are laminated structures consist of several plies of impregnated fibers with polymeric matrix with dissimilar thermal properties in different directions. The thermal behavior of composite materials is complicated because of their heterogeneity. Numerous analytical, experimental and

numerical methods have been developed for modeling the heat distribution inside a composite laminate. Analytical approaches for predicting temperature distribution in composite materials are limited to special geometries, thermal loadings and boundary conditions [25].

Numerical models using finite element and finite difference methods have also been developed for heat transfer studies in fiber reinforced composites [25-28]. Heat transfer models for polymer composites are mostly developed based on the laminate theories for structural analysis and have been solved by finite element methods [25, 27]. Thermal Lamination Theory (TLT) is the most common approach for modeling temperature distribution through the composite thickness. In this model the individual thermal properties of each layer in the composite is replaced with a set of homogenous anisotropic thermal properties. The TLT theory is applicable when the thermal conductivities of adjacent layers are almost the same, and the span to thickness ratio of the composite is large [25, 27].

There are also other models when the above conditions are not satisfied, such as zig-zag thermal lamination model by assuming a piecewise linear variation of the temperature. Pantano and Averill [27] have studied heat transfer in composite structures and developed a finite element model using zig-zag sublaminate structural laminate theory. In this model the composite laminate is considered as several sublamites, which each sublaminate consists of one or several plies. All of these models, which provide temperature distribution profile in the layered composite thickness, are sophisticated and time

consuming. In this thesis we were not interested in complicated thermal modeling for investigating temperature distribution inside the composite thickness.

Thermal modeling of the embedded thermal elements in the polymer composite laminate was necessary to estimate the surface temperature of the thermal elements to prevent thermal degradation of the composite material due to overheating. To satisfy this requirement, an analytical and a numerical thermal analysis were carried out in this study.

An analytical model was developed for a composite flat plate with the embedded heating elements for simplicity and understanding the thermal behavior of the system. Composite material was considered homogenous. This simplified steady-state one-dimensional thermal model was based on thermal resistance concept and conduction shape factor [29] used for predicting the embedded heating elements' temperature.

A simplified numerical thermal analysis using ABAQUS 6.9 student version from SIMULIA® was also performed for the composite airfoil equipped with the heating system. The composite material was considered as a single layer, and it was also assumed that the transverse heat flux is continuous at ply interfaces. Surface temperature of the embedded thermal elements and temperature distribution inside the composite airfoil as well as its surface temperature distribution were numerically simulated by a steady-state two-dimensional thermal model. Thermal modeling was also used to verify the experimental results, and explain some of the experimental observations. The results of the simplified model were satisfactory.

1.6 Objectives

In this study, the concept of embedded thermal elements as an anti-icing system for polymer composite airfoils used in wind turbine blades and aircraft wing structures was proposed, and developed experimentally and numerically. The concept was developed based on thermal mapping of the system tested in cold (dry) and icing (wet) conditions. The specific objectives of this thesis were as follows:

- Investigate the feasibility of the concept through making flat composite coupons with embedded heating elements, and characterize thermal behavior of the system.
- Develop a manufacturing technique to implement the electro-thermal anti-icing system in the form of discrete thermal elements with a specific pattern inside airfoils made of composite laminates.
- Implement an IR camera as the temperature measurement tool in the experimental setup for thermal mapping of the system in cold (dry) and icing (wet) condition tests.
- Investigate the effect of surface temperature distribution and uniformity on the icing behavior of composite airfoils.
- Preliminary investigation of the effect of thermal elements' spacing/pattern and input power scheme to the heating system on the airfoils' surface temperature distribution, and the effectiveness of the thermal elements' pattern for icing mitigation.

- Determine the power threshold in the anti-icing system to prevent thermal degradation of the polymer composite by a numerical simulation of heat transfer in the systems tested.
- Develop an image analysis methodology based on IR imaging for simultaneous monitoring of ice accretion and thermography of airfoils.

1.7 Scope

This study focuses on developing the concept of embedding thermal elements as an anti-icing system for polymer composite airfoils. The focus of this study is thermal behavior of the concept. As such, the study is focused on conceptual design aspects of the proposed anti-icing system, fabrication techniques, the energized airfoils' surface temperature profiles, and energy consumption. Issues related to possible effects of embedding thermal elements on mechanical performance of composite test samples are not considered. Also, issues such as thermal stresses induced by heating of composite, low thermal conductivity of polymer composite materials, delamination possibility of composite laminates, protecting the composite material from permanent damage due to overheating (e.g. by sensor development), and system reliability are not considered in this thesis.

In this thesis thermal behavior of composite airfoils equipped with the anti-icing system was also numerically simulated. In numerical thermal analysis of the airfoil, the entire airfoil was modeled as a flat plate for simplicity and realizing that the interest was on the

conceptual level principally. The flat plate simplified model was validated through comparing experimental and modeling results.

This thesis also presents a method for simultaneous monitoring of ice accretion and thermography of airfoils using IR imaging. The developed methodology uses an image processing routine coded in MATLAB, to not only detect and quantify the ice covered areas, but also simultaneously measure the surface temperature evolution of the airfoil during an icing test.

1.8 References

[1] Aircraft icing handbook, Civil Aviation Authority, 2000, http://www.caa.govt/, Accessed March 19, 2010, Chap. 1.

[2] S. K. Thomas, R. P. Cassoni, 1996, "Aircraft ant- icing and de-icing techniques and modeling", J. Aircraft, 33, pp. 841-854.

[3] N. Dalili, A. Edrisy, R. Carriveau, 2009, "A Review of surface engineering issues critical to wind turbine performance", Renewable Sustain. Energy Rev., 13, pp. 428-438.

[4] O. Parent, A. Ilinca, 2011, "Anti-icing and de-icing techniques for wind turbines: critical review", Cold Reg. Sci. Technol., 65, pp. 88-96.

[5] A. G. Kraj, "Icing characteristics and mitigation strategies for wind turbines in cold climates", University of Manitoba, M.Sc. thesis, March 2007.

[6] Charles A. Harper, "Handbook of plastics, elastomers and composites", McGraw-Hill, 4th ed., 2002, Chap. 4.

[7] A. H. Tabrizi, W. S. Johnson, 1998, “Surface-blowing anti-icing technique for aircraft surfaces”, J. Aircraft, 26, pp. 354-359.

[8] G. Fortin, J. Perron, 2009, “Wind turbine icing and de-Icing”, 47th AIAA Aerospace Sciences Meeting, Orlando, Florida, Paper No. AIAA-2009-274.

[9] C. Antonini, M. Innocenti, T. Horn, M. Marengo, A. Amirfazli, 2011, “Understanding the effect of superhydrophobic coatings on energy reduction in anti-icing system”, Cold Reg. Sci. Technol., 67, pp. 58-67.

[10] G. Lubin, S. T. Peters, “Handbook of composites”, Chapman & Hall, 2th ed., 1998, Chap. 3.

[11] Ching-Cheh Hung, M. E. Dillehay, M. Stahl, 1987, “A heater made from graphite composite material for potential deicing application”, J. Aircraft, 24, pp. 725-730.

[12] H. Siefert, 2004, “Technical requirements for rotor blades operation in cold climate”, BOREAS IV, 9-11 April, Pyhae, Finland.

[13] X. Wang, “Convective heat transfer and experimental icing aerodynamics of wind turbine blades”, University of Manitoba, PhD thesis, August, 2008.

[14] S. W. Ciardullo, S. C. Mitchell, R. D. Zerkle, 1987, “Evaluation of capillary reinforced composites for anti-icing”, 25th AIAA Aerospace Sciences Meeting, Reno, Nevada, Paper No. AIAA-87-0023.

[15] R. Elangovan, R. F. Olsen, 2008, “Analysis of layered composite skin electro-thermal anti-icing system”, 46th AIAA Aerospace Sciences Meeting, Reno, Nevada, Paper No. AIAA-2008-0446.

[16] Expert group study on "Wind Energy Projects in Cold Climates", edition 2005, http://virtual.vtt.fi/virtual/arcticwind/reports/recommendations.pdf, Accessed March 19, 2010.

[17] G. Fortin, C. Mayer, J. Perron, 2008, "Icing wind tunnel study of a wind turbine blade deicing system", Sea Technol., 49, pp. 41-44.

[18] J. Schuster, D. Heider, K. Sharp, M. Glowania, 2008, "Thermal conductivities of three-dimensionally woven fabric composites, Composites Sci. Technol., 68, pp. 2085-2091.

[19] F. C. Campbell, "Structural composite materials", ASM International, 2010, Chap. 1.

[20] A. Vanaja, R. M. V. G. K. RAO, 2002, "Fiber fraction effects on thermal degradation behavior of GFRP, CFRP and hybrid composites", J. Reinforced Plastics Composites, 21, pp.1389-1398.

[21] K. E. Perepelkin, 2006, "Fiber composite materials, fiber polymer composites, basic types, principles of fabrication, and properties. Part 4", Fiber chemistry, 38, pp. 224-239.

[22] R. M. Vauhini, V. Srinivasan, V. S. Panchagavi, 2006, "Heat transfer studies on glass epoxy composite laminates-effects of heating rate and fiber fraction", J. Reinforced Plastics Composites, 25, pp.1353-1365.

[23] I. H. Tavman, H. Akinci, 2000, "Transverse thermal conductivity of fiber reinforced polymer composites", Int. Comm. Heat and mass transfer, 27, pp.253-261.

[24] Y. Gowayed, Jhy-Cherng Hwang, 1995, "Thermal conductivity of composite materials made from plain weaves and 3-D weaves", Composites Eng., 5, pp.1177-1186.

[25] R. Rolfes, 1990, “Effective thermal analysis of anisotropic composite plates using new finite elements”, Fourth European Conference on Composite Materials, Stuttgart, F.R.G., pp. 743-748.

[26] B. W. James, G. H. Wostenholm, G. S. Keen, S. D. Mclvor, 1987, “Prediction and measurement of the thermal conductivity of composite materials”, J. Phys., D: Appl. Phys., 20, pp. 261-268.

[27] A. Pantano, R. C. Averill, 2002, “An improved thermal lamination model for analysis of heat transfer in composite structures”, J. Composite Materials, 36, pp. 701-719.

[28] M. Amazouz, R. Gauvin, 1997, “Solving heat dissipation problems in unidirectional composite structure”, J. Reinforced Plastics Composites, 16, pp. 686-697.

[29] Y. A. Çengel, “Heat and mass transfer: a practical approach”, McGraw-Hill, 3rd ed., 2007, Chap.3 and 7.

2. Electro-thermal Icing Mitigation System for Polymeric Composite Airfoil[*†]

2.1 Introduction

Icing adversely affects the performance of aerodynamic structures such as aircraft wings and wind turbine blades. It is responsible for increasing the weight and decreasing the aerodynamic efficiency of the wing by decreasing the lift and increasing drag [1-3]. Over the years, a number of icing mitigation techniques have been developed and are categorized as anti-icing and de-icing systems [1, 4, 5]. De-icing is a process to remove ice from the surface after formation to provide a clean surface. There are various methods for de-icing e.g., pneumatic boots, thermal and chemical techniques using heat system and chemical fluids for ice removal [1, 4, 5].

Anti-icing systems prevent the formation of ice or frost for a limited period of time, and they are activated before entering icing conditions to prevent the adhesion of ice to the surface [1]. There are mainly three types of anti-icing systems, i.e., chemical systems, hot-air systems and electrical resistance heating (electro-thermal) systems [2]. There are also other systems such as super-hydrophobic coatings.

---

[*] A version of this chapter has been published in Proceedings of the ASME 2010 International Mechanical Engineering Congress & Exposition, Vancouver. Mohseni, Mertiny, Amirfazli, Nov. 2010.

[†] In this chapter different power amount definition is used than the rest of this thesis.

In chemical systems a chemical liquid with a low freezing temperature such as ethylene glycol is distributed on the ice prone surface [2, 4]. This system has been used successfully in some of aircrafts, but due to the weight load of the anti-icing liquid that the aircraft must carry, this system is generally not considered to be an effective anti-icing system.

In hot-air systems, which are the most prevalent thermal anti-icing systems, hot bleed air is ducted from the compressor of the engine to the wings through piccolo tubes or narrow gas passages to transfer thermal energy to the surface and thus heat the wing surface [2]. This is a highly reliable and well developed technology for conventional aircraft wings. But, due to the required volumetric flow rate of hot air, a relatively large amount of fuel is spent on heating and thrust is reduced which are important issues considering aircraft efficiency [2]. A system for polymer composite airfoils can be challenging since maximum operating temperature and thermal resistance of polymer composites pose a temperature limit for hot air [6, 7]. Ciardullo et al. [10] have developed a method for using hot-air as an anti-icing system for advanced composite structures. The concept involves conducting hot air through embedded glass capillary tubes on the surface of the composite structure rather than conducting heat through thick composite walls. Surface heating of composites employing this method was investigated, but its energy consumption and its effect on surface roughness, which can lead to increase the aerodynamic drag, has not been assessed. It was also not tested in icing conditions.

Electrical resistance heating systems are mostly used in the form of electro-thermal pads, applied to the surface of a structure, to prevent ice formation. In one version of such thermo-electric system, pads consist of a heating element, two layers of insulation and a layer of sheet metal as a shield. This system is very simple, but the power consumption can be very high [2]. Different types of electro-thermal pad systems with various electrical heating elements such as metal foils, carbon fibers, and graphite fiber/epoxy composites have been developed for different structures [3, 5, 7-9].

Hung et al. [3] reported on the use of a surface electro-thermal heater made from graphite composite material in the form of flat coupons. The heating element in this system is a graphite fiber/epoxy composite which is claimed to have high thermal and electrical conductivity. The protecting layers are made of glass fiber/epoxy composites. This system, which can be formed on irregular surfaces, was found to have acceptable heating performance in room temperature tests, but it has not been tested in wind tunnel icing experiments.

In this paper a new electro-thermal system is explored to be used as an anti-icing system for polymer composite structures. In this system, constantan wires which are used as electrical thermal elements are embedded in an aircraft grade fiber glass/epoxy composite in the form of flat coupons. The coupons were made and tested in room temperature and cold room conditions to investigate the feasibility of the concept. This system does not need any protection and sheet metal layers, and it can simply be incorporated during the manufacturing of a polymer composite structure such as airfoils. It is also applicable to

irregular surfaces with different profiles. It provides a smooth surface and allows for the thermal elements to be placed close to the surface with direct heating, resulting in a nearly uniform heating of the surface. In principle this system can be customized so that the temperature of different locations on the surface can be controlled to reach a specific anti-icing temperature while minimizing energy consumption.

2.2 Experiments

2.2.1 Materials and Manufacturing Procedure

In this study, polymer composite laminates were manufactured from a commercially available aerospace-grade fiberglass/epoxy prepreg, i.e., Necote E-765 epoxy/fiberglass prepreg from Park Electrochemical Corporation Advanced Material Technologies. Prepregs are pre-impregnated reinforcing fibers with a partially cured polymer matrix resin. The reinforcing phase in this prepreg is woven fiberglass (E-glass) fabric. Prepregs are in the form of sheets which can readily be applied to make the structure; hence, experimental uncertainties due to composite sample fabrication will be minimized. Since here polymer composites are subjected to relatively high temperatures, thermal stability of the prepreg in the anti-icing system is important. In polymer composites, thermal stability depends on the matrix system and it increases with an increasing glass transition temperature (Tg) [11]. Consequently, the prepreg was selected based on its Tg and maximum operating temperature. The specification of the selected prepreg is provided in Table 2-1.

Constantan wire was used as the thermal elements in the anti-icing system, because its resistivity is almost constant over a wide temperature range (0-100°C). Constantan wires with two diameters, i.e., 0.13 mm and 0.25 mm, were used from Omega Engineering Inc. Corresponding physical properties are presented in Table 2-2. Since both wires with different diameters are analyzed in this study, the wires will be termed 'thin' and 'thick' wire respectively.

Table 2-1- Physical properties of the prepreg as provided by the manufacturer.

Prepreg	**Resin solids (%)**	**Volatile content (% max)**	**Tg (by DMA) (°C)**
7781 E-Glass	38	1.5	165
Gel time @275F (min)	**Void content (%)**	**Maximum wet service temperature (°C)**	**Maximum dry service temperature (°C)**
5	< 2%	82	137

Table 2-2- Physical properties of the thermal elements as provided by the supplier.

Type	Constantan T
Composition	45% Nickel 55% Copper
Size (mm)	0.13 0.25
Resistivity at 0°C & 20°C (μΩcm)	48.9
Temperature coefficient of resistance, 0-100°C (Ω/Ω/°C)	-0.1×10^{-4}
Thermal conductivity at 100°C (W/m°C)	21.115

The polymer composite laminates were fabricated by hand lay-up of six prepreg layers. The constantan wires as thermal elements were laminated in the middle of the composite sheet. The thermal wires were aligned straight inside the composite laminate using a specially designed jig. At first, three layers of prepreg were deposited, then the thermal wires were affixed on the third layer, and another three prepreg layers were laminated on top of the elements.

The final dimension of the fabricated composite laminate was 15cm (L) × 16cm (W) × 1.4mm (H). The length of each constantan wire was 10cm and the distance between two adjacent wires was 1cm. Also, two wires were put near both edges of the sheet with a 2.5cm distance from the next wire to investigate edge effects. The laminate was then covered with vacuum bagging material and cured in the form of a flat plate for one hour at 82°C, followed by a two-hour cure at 135°C, in an oven applying a minimum vacuum pressure of 82kPa. Following curing, the thermal elements were connected to each other to form a serial circuit.

2.2.2 Measurements

Composite sheets with embedded heating elements were tested in an open circuit wind tunnel. This low speed wind tunnel is refrigerated and able to operate at subzero temperatures. The test section is a transparent, ice free cavity 26cm high, 30cm long and 38cm wide. Tests were conducted at room temperature and cold room conditions between -12°C and -10°C under a maximum air flow of 27m/s. Composite sheets were heated by connecting the thermal elements to a DC power supply. The power was adjusted in a range of 2W to 26W for room temperature tests and 24W to 40W in cold room

experiments. The composite surface temperature at different power levels was recorded by eight fast response T-type thermocouples as a function of heating time. A schematic of the thermocouple positions on the sheet surface is shown in Figure 2-1.

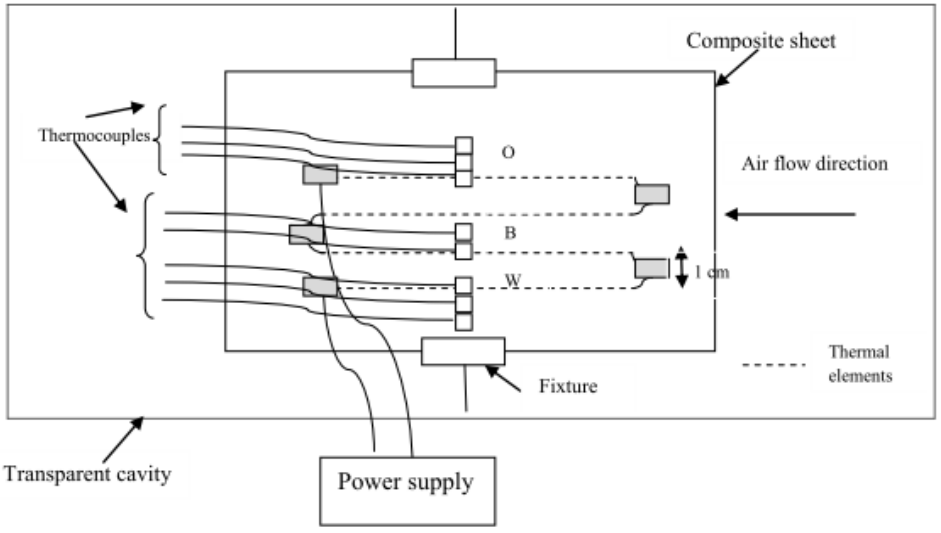

Figure 2-1- Top view schematic of thermocouple positions on the sheet surface in the transparent wind tunnel test section.

Thermocouples were placed on a straight line on the surface 0.5cm apart from each other. In Fig.1, “W”, “B” and “O” represent a location on a thermal element, the midpoint between two adjacent thermal elements, and a point outside the thermal element section respectively. Thermocouples were connected to a data acquisition system and surface temperatures were recorded using Labview software by National Instruments. The temperature as a function of heating time was recorded at different points on a straight line on the surface. In this study, test data were obtained from samples with seven thermal elements, of which five were put 1cm from each other and the remaining two, located near the sample edges, were 2.5cm far from the next thermal element.

2.3 Results and Discussion

When the thermal elements were heated starting from room temperature with a DC current with constant electrical power, the temperature rise at selected points on the surface was monitored with time as shown in Figure 2-2. As can be seen in Figure 2-2, the surface temperatures on the thermal elements (TW) were higher than those of points between the elements (TB) and outside the thermal element section (TO). It was observed that the temperature rise for different points on the surface reached 50% of the final steady-state value in 20 seconds, which indicates a rapidly responding heating system.

The steady-state temperature at 250 seconds (T_{250} - $T_{ambient}$) as a function of their position relative to the sample edge at different normalized power amounts is shown in Figure 2-3. Power amounts were normalized with respect to the total length of the thermal elements in the composite sheets. It was found that the temperature distribution on the surface is relatively uniform for the points on the thermal elements and between them, except at the points where their distance from the thermal elements were more than 0.5cm (TB2, TB3), those with more than 0.5cm distance from one thermal element (TB1, TB4) and points located outside the thermal elements section (TO1, TO2). The lowest temperature was observed on TO1, TB2 and TB3 and their temperatures did not increased by increasing power. This indicates that temperature does not increase with power for the surface points with 1cm distance from the thermal elements.

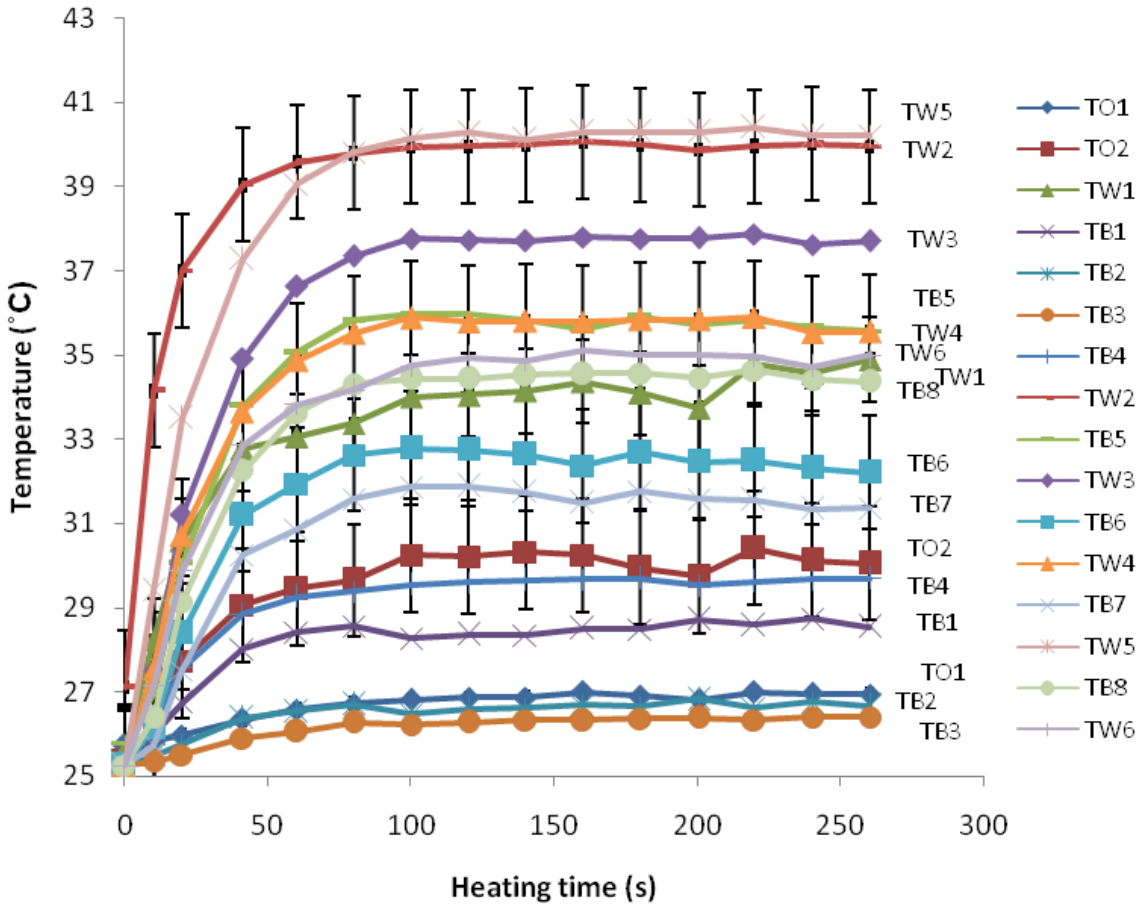

Figure 2-2- Temperature as a function of heating time for thick thermal element at 0.27W/cm (power per element length) at room temperature; (TW1: Temperature on the thermal element next to the sample edge; TW2: Temperature on the second thermal element 2.5cm away from W1; TW3, 4, 5, 6: Temperature on the thermal elements, each 1cm further from previous one; TO1: Temperature of the point 1cm from W1 and outside the thermal element section; TO2: Temperature of the point 0.5cm from W1 and outside the thermal element section; TB1: Temperature of the point 0.5cm from W1 and 2cm from W2; TB2: Temperature of the point 1cm from W1 and 1.5cm from W2; TB3: Temperature of the point 1.5cm from W1 and 1cm from W2; TB4: Temperature of the point 2cm from W1 and 0.5cm from W2; TB5: Temperature of the midpoint between W2 and W3; TB6: Temperature of the midpoint between W3 and W4; TB7: Temperature of the midpoint between W4 and W5; TB8: Temperature of the midpoint between W5 and W6.) (Note that lines connecting data points are shown to provide a guide for the eye of the reader).

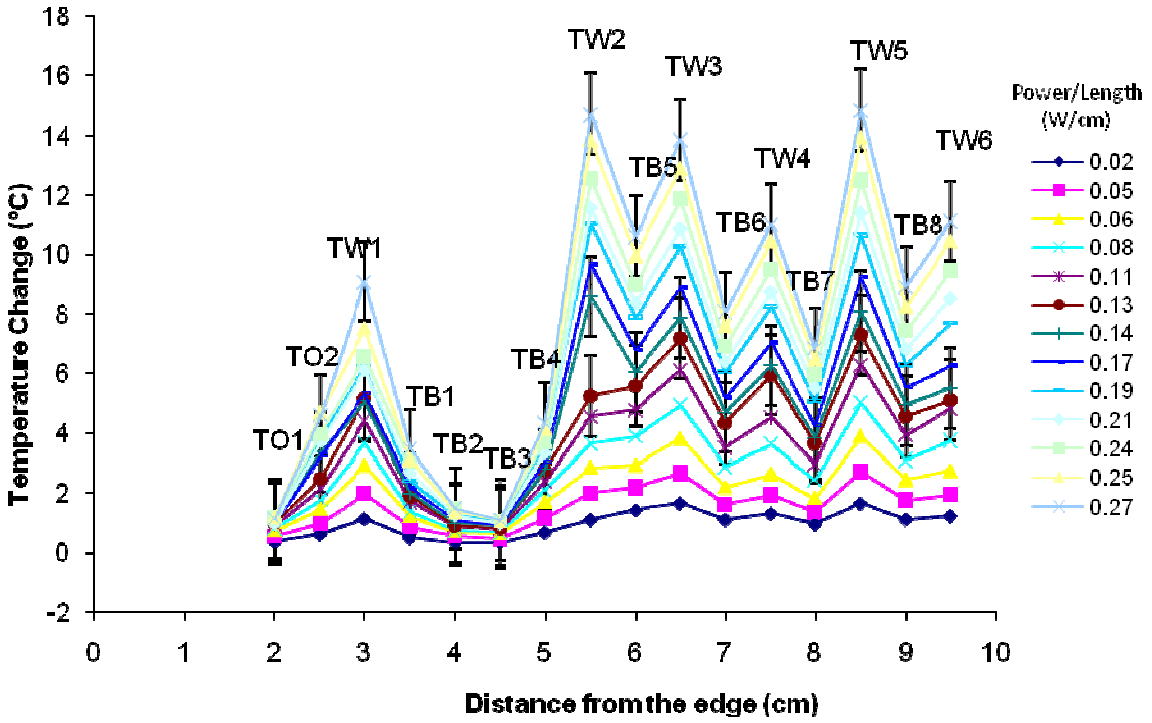

Figure 2-3- Steady-state temperature of different points as a function of their position relative to the sample edge at various W/cm at room temperature for the thick thermal element. (Note that lines connecting data points are shown to provide a guide for the eye of the reader).

As can be noticed from Figure 2-3, the temperature distribution on the surface is more uniform at lower power levels, and by increasing power, temperature differences between the various points on the surface increases. Considering the uncertainty of temperature measurements, the maximum temperature difference between the points on the wires (TW) and points between the wires (TB) was 5°C at 0.27W/cm. This can be explained by the low thermal conductivity of the composite material. It shows that the maximum distance between thermal elements should not be more than 1cm in order to ensure a relatively uniform temperature distribution on the surface. In icing condition, this pattern of thermal elements in the composite material, which can provide a nearly uniform temperature distribution, would be able to keep the entire surface warm enough for

preventing ice formation. Furthermore, the required anti-icing surface temperature can be controlled by the spacing between thermal elements and electrical power input.

Figure 2-3 and Figure 2-4 show that the temperature of different points increases with increasing power; but its increase rate is higher for the surface points located on the thermal elements. The rate is lowest for the points located outside the thermal elements section and those which are not located between two thermal elements with 1cm distance. The maximum temperature change from room temperature at a power input of 0.27W/cm is about 13°C for the surface point on the thermal element, and the minimum is less than 1°C for TO1, TB3 and TB2 whose distance from the thermal elements is 1cm and more.

In the present application, polymer composite materials may potentially be subjected to high temperatures, and when being exposed to temperatures above or close to their upper service temperature, they will irreversibly be damaged. Hence, the surface temperature of the thermal elements must carefully be considered, i.e. it must be less than the maximum working temperature of the composite. In a separate study based on the developed thermal model provided in Section 2.4, the present researchers determined that the surface temperature of the thermal elements was about 73°C, which is lower than the maximum service temperature of the composite. As a result, 0.27W/cm is a safe power level which can be applied without composite thermal degradation.

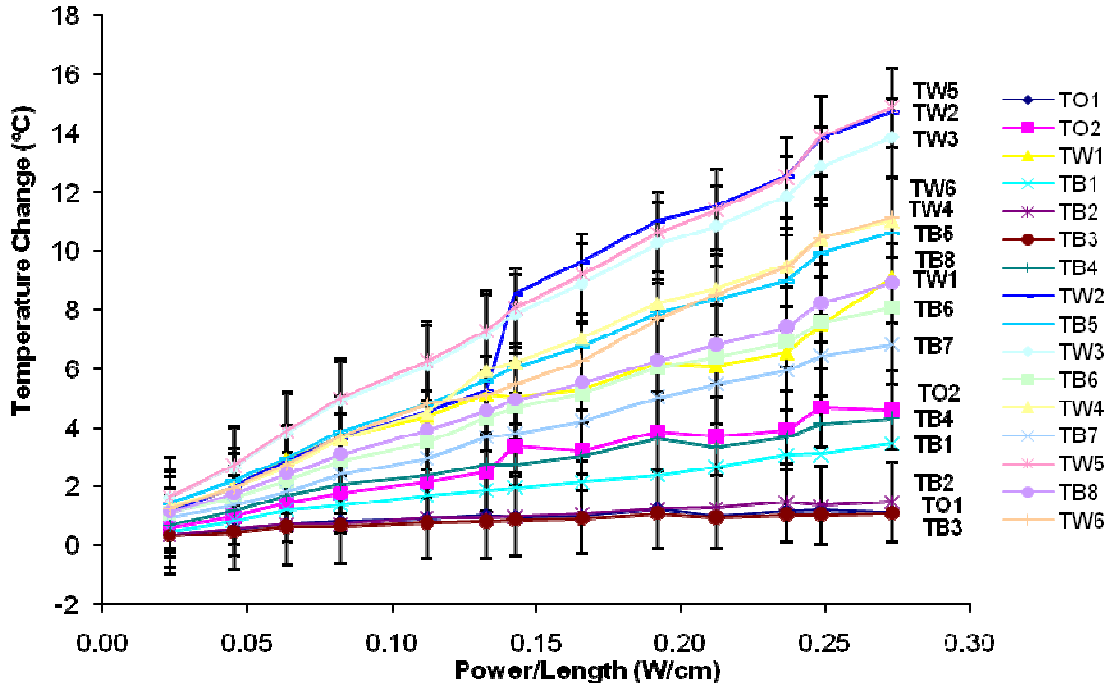

Figure 2-4- Steady-state temperature changes of different points of the surface as a function of power input at room temperature for the thick thermal element; (Note that lines connecting data points are shown to provide a guide for the eye of the reader).

Constantan wires with two different diameters were used as thermal elements to investigate the difference between two types of thermal elements. As it can be seen from Figure 2-5, the temperature distribution for the thin wire is less uniform compared to thick wire (see Figure 2-3). Figure 2-5 shows that the temperatures on the wires are not necessarily the highest ones, and do not show a specific trend. This can be explained by the fiber orientation, the relative position of thermal elements with respect to the reinforcing fibers and resin matrix in the composite material and voids trapped during the manufacturing process. This behavior was verified through experimental results from other composite coupons with thin wire.

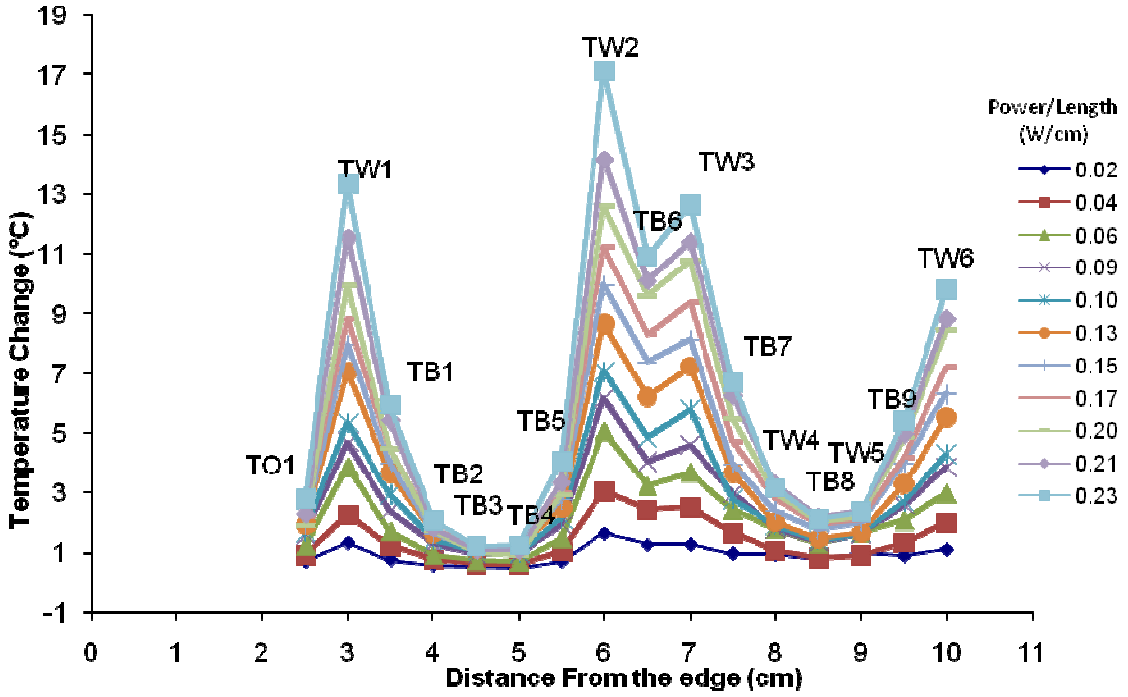

Figure 2-5- Steady-state temperature of different points as a function of their position relative to the sample edge at various W/cm at room temperature for the thin thermal element; (Note that lines connecting data points are shown to provide a guide for the eye of the reader).

Steady-state temperatures of three specific points on the composite sheets with two types of thermal elements are provided as a function of power in Figure 2-6. This figure shows that for the selected points which are on the wire (TW), between two wires with 0.5cm from each wire (TB-0.5) and between two wires with 1cm from one wire and 1.5cm from other wire (TB-1), the temperature changes for thin and thick wires were the same at a specific power input. Since the diameter of the constantan wire did not affect its performance as a thermal element, and working with thick wire is generally easier than with a thin one, the thick wire was selected for further experiments at this stage.

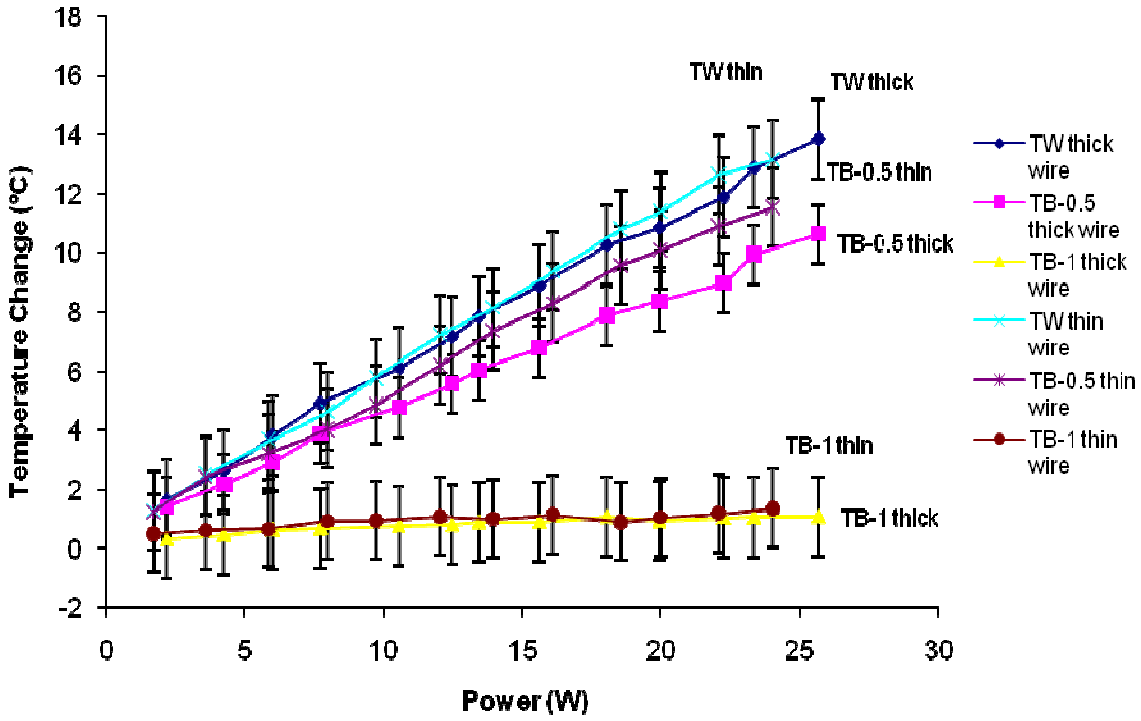

Figure 2-6- Comparison of surface temperature changes at three similar surface points for thermal elements with two different diameters as a function of power input; (Note that lines connecting data points are shown to provide a guide for the eye of the reader).

Surface temperature measurements for the composite sample with the thick thermal elements in cold room conditions are shown in Figure 2-7. In this Figure the steady-state temperature of the selected points at 250 seconds is presented as a function of their distance from the sample edge at different power inputs. It can be seen from Figure 2-7 that even at the highest power input of 0.42 W/cm, point TB3 (which is located 1.5cm from the edge thermal element and 1cm from the second one) and TB4 (located 2cm from the edge thermal element and 0.5cm from the second one) could not reach to above-zero temperatures. This means that under icing conditions, the points which are located farther than 0.5cm from one thermal element will be cold spots which could lead to the formation of ridges in cold regions. Similar to room temperature experiments, the surface points on the thermal elements showed the highest temperatures, and points between the

wires had lower temperatures. All surface points, except TB3 and TB4, reached a temperature above 0°C at a power level of 0.32W/cm, and above 5°C at 0.42W/cm, which is high enough to prevent ice formation in icing conditions.

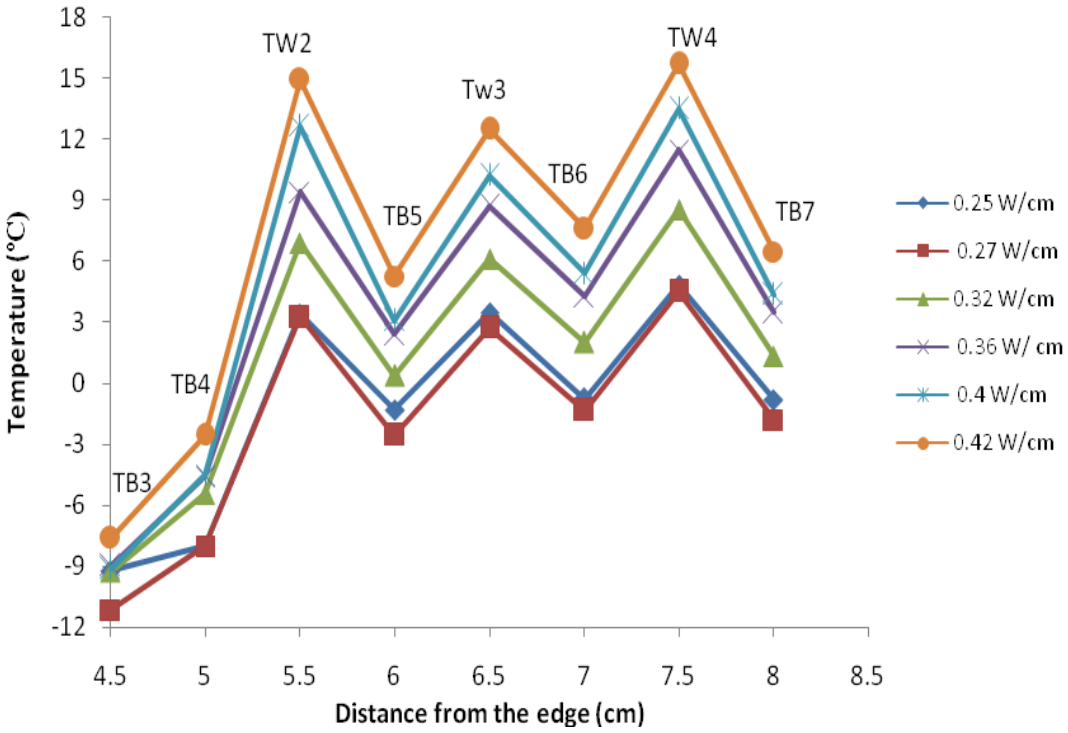

Figure 2-7- Steady-state temperature of different points as a function of their position relative to the sample edge at different W/cm for cold room tests with the thick thermal elements; (Note that lines connecting data points are shown to provide a guide for the eye of the reader).

Figure 2-8 shows the steady-state temperature of different points on the surface as a function of power-per-length for cold room conditions. The rate of temperature increase with power for different points, except for TB3 and TB4, is almost the same. As shown in Figure 2-7 and Figure 2-8, the surface temperature increases with increasing power input, and the surface temperature can be controlled with the amount of applied power.

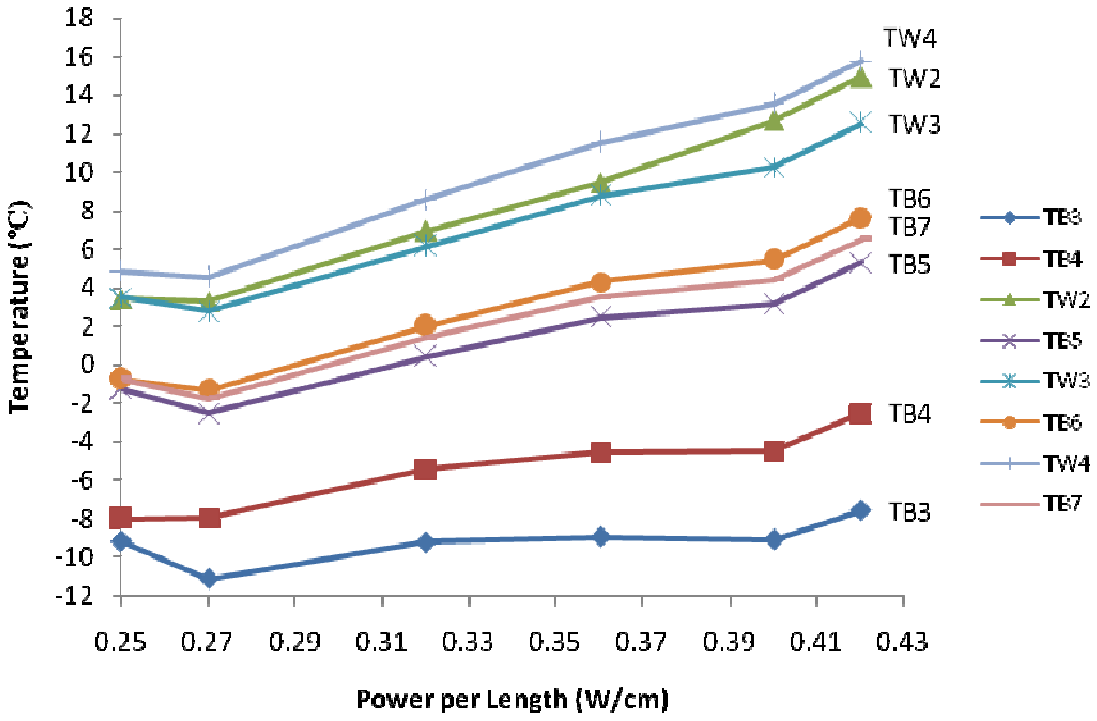

Figure 2-8- Steady-state temperature of different points as a function of power input for cold room test with the thick thermal elements; (Note that lines connecting data points are shown to provide a guide for the eye of the reader).

Thermal analysis showed that the surface temperature of thermal elements at 0.42W/cm is about 61°C, which is less than the maximum service temperature of the polymer composite. Hence, this heating power can be applied to composite samples without causing thermal degradation. Also, this power level seems sufficient to prevent ice formation on the composite surface.

2.4 Thermal Analysis

A simplified steady-state one-dimensional thermal model based on thermal resistance concept and conduction shape factor was used for predicting the embedded heating elements' temperature. The heating element in this model was considered a distinct

thermal element in the shape of wire embedded in the mid plane of a composite flat plate. It was assumed that all of the heat flows directly to the nearest outside surfaces; the composite laminate was considered homogenous; and thermal conductivity is constant with respect to temperature. Only one thermal element is modeled due to the symmetry of embedded elements in the composite plate. The boundary conditions for the top and bottom surfaces of the sheet were considered convection. Adiabatic boundary conditions for the other two sides of the plate were considered due to the symmetry. Figure 2-9 shows the cross section of composite flat sheet with embedded thermal element.

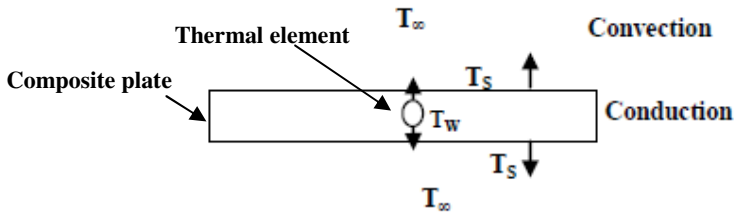

Figure 2-9- Schematic cross section of the composite plate with embedded thermal element

Thermal resistance network consists of heat conduction through the composite sheet and convection on its both surfaces. Thermal energy ($\dot{Q}$), was related to each thermal resistance in the circuit as well as to the total thermal resistance, i.e. sum of individual thermal resistances:

$$\dot{Q} = \frac{T_W - T_\infty}{R_{cond.} + R_{Conv.}} \tag{1}$$

$$\dot{Q} = \frac{T_W - T_S}{R_{cond.}} = \frac{T_S - T_\infty}{R_{conv.}} \tag{2}$$

where, $\dot{Q}$ is thermal energy, T_∞ is ambient temperature, T_S is surface temperature of the composite plate, which assumed equal for the top and the bottom surfaces due to the symmetry of the system, T_W is surface temperature of the thermal element, $R_{cond.}$ is conduction thermal resistance through the composite sheet, and $R_{conv.}$ is thermal resistance of convection on the top and bottom surfaces of the plate.

Conduction resistance of the composite plate is calculated using a conduction shape factor:

$$R_{cond.} = \frac{1}{S.\,k_{c,22}} \tag{3}$$

where, S is the conduction shape factor and $k_{c,22}$ is thermal conductivity of the composite plate in transverse direction.

Considering the configuration of composite plate with embedded element, the most appropriate shape factor for this experiment is considered for circular isothermal cylinder of length L in the mid plane of an infinite wall. The configuration of the conduction shape factor can be found in [12]. The shape factor for this configuration is [12]:

$$S = \frac{2\pi L}{ln\left(\frac{8Z}{\pi D}\right)} \tag{4}$$

where, L is thermal element's length (m), Z is the distance between thermal element's center and the sample surface (m), D is the diameter of thermal element (m) (for infinite wall $Z > 0.5\ D$).

Convection thermal resistance for both surfaces of the composite plate can be calculated by:

$$R_{conv.} = \frac{1}{h.(2A)} \quad (5)$$

where, h is the convection heat transfer coefficient and A is considered as the surface area of the composite plate above the thermal element. "A" is calculated based on the thermal element length and the thermal elements' spacing.

Forced convection heat transfer coefficient (h), for a laminar flow over a flat plate surface, can be calculated by [12]:

$$Nu = hL/k = 0.664\ Re_L^{0.5}\ Pr^{1/3} \quad (6)$$

$$Re_L = UL/\nu \quad (7)$$

where, Nu is Nusselt number, Re_L is Reynolds number at the end of plate with length L, U is the free stream velocity, L is the length of composite plate, h is convection heat transfer coefficient, k is thermal conductivity of the air, Pr is Prandtl number.

2.5 Conclusions

The concept of embedded thermal elements as an electro-thermal anti-icing system in polymer composite structures was developed. The feasibility of this system was investigated through making flat composite plates with constantan wires as thermal

elements located in the middle of the composite laminate. Electrical power was applied to the heating system in wind tunnel tests at room temperature and cold room conditions. Temperature measurements of the surface showed that the maximum allowable distance between thermal elements resulting in a relatively uniform temperature on the surface was 1cm. The system also provided fast heating of the surface when power applied to the heating elements, and the surface temperature reached 50% of its steady-state temperature in 20 seconds. The surface temperature increased with increasing power input, and the maximum temperature rise at 0.27W/cm was 13°C at the thermal element locations. A similar trend of temperature rise with heating time and power input at similar points on the surface was observed for room temperature and cold room tests. Therefore, the required anti-icing temperature on the composite surface can be adjusted and controlled by the spacing of the thermal elements and the amount of applied electrical power. In cold room test at -10°C, the temperature of the surface at the thermal elements and between them were above 5°C at 0.42W/cm, which is sufficient high to prevent ice formation in icing conditions. This power level is also safe for the polymer composite material and can be applied without causing thermal degradation of the composite.

2.6 References

[1] Aircraft icing handbook, Civil Aviation Authority, 2000, http://www.caa.govt/, Accessed March 19, 2010, Chap. 1.

[2] S. K. Thomas, R. P. Cassoni, 1996, “Aircraft ant- icing and de- icing techniques and modeling”, J. Aircraft, 33, pp. 841-854.

[3] Ching-Cheh Hung, M. E. Dillehay, M. Stahl, 1987, "A heater made from graphite composite Material for potential deicing application", J. Aircraft, 24, pp. 725-730.

[4] A. H. Tabrizi, W. S. Johnson, 1998, "Surface-blowing anti-icing technique for aircraft surfaces", J. Aircraft, 26, pp. 354-359.

[5] N. Dalili, A. Edrisy, R. Carriveau, 2009, "A Review of surface engineering issues critical to wind turbine performance", Renewable Sustain. Energy Rev., 13, pp. 428-438.

[6] O. Parent, A. Ilinca, 2011, "Anti-icing and de-icing techniques for wind turbines: Critical review", Cold Reg. Sci. Technol., 65, pp. 88-96.

[7] Expert group study on "Wind Energy Projects in Cold Climates", Edition 2005, http://virtual.vtt.fi/virtual/arcticwind/reports/recommendations.pdf, Accessed March 19, 2010.

[8] G. Fortin, C. Mayer, J. Perron, 2008, "Icing wind tunnel study of a wind turbine blade deicing system", Sea Technol., 49, pp. 41-44.

[9] H. Seifert, 2003, "Technical requirements for rotor blades operating in cold climate", BOREAS 4 FMI, Pyhatunturi, Finland, pp.13.

[10] S. W. Ciardullo, S. C. Mitchell, R. D. Zerkle, 1987, "Evaluation of capillary reinforced composites for anti-icing", AIAA 25th Aerospace Sciences Meeting.

[11] G. Lubin, S. T. Peters, "Handbook of composites", Chapman & Hall, 2th ed., 1998, Chap. 3.

[12] Y. A. Çengel, "Heat and mass transfer: a practical approach", McGraw-Hill, 3rd ed., 2007, Chap.3 and 7.

3. A Novel Electro-thermal Anti-icing System for Fiber-reinforced Polymer Composite Airfoils*

3.1 Introduction

Composite materials are versatile and customizable, hence used widely in wind turbine blades and aircraft structures. The most important properties of polymer composite materials are their high specific stiffness and strength in comparison to metals. Icing of the polymer composite aerodynamic structures, such as airplanes' wing and wind turbine blades, can be a serious problem. Icing changes the dynamic behavior of the whole structure, changes the airfoils' shape, increase surface roughness, and can increase the weight, increase drag, and decrease lift [1, 2]. In wind turbines, icing affects the turbine's power production efficiency; and even a light icing event can roughen the turbine blades' surface to decrease the aerodynamic efficiency [3, 4].

Anti-icing systems are mainly categorized into two types: passive and active. Passive anti-icing systems such as black paint and so-called "ice-phobic" coatings have their own drawbacks on composite materials. Since the polymer composite materials are sensitive to high temperatures, black paint on the wind turbine blade may increase the surface temperature which leads to thermal degradation of the composite material in summer time [4, 5]. Most of the time the passive anti-icing systems are not sufficient to prevent icing, and they should be combined with an active anti-icing systems [5, 6].

---

* This chapter has been submitted to Cold Reg. Sci. Technol. J., Mohseni, Amirfazli, 2012.

Active anti-icing systems mainly require an energy supply, which can be thermal, chemical or pneumatic. Traditional thermal anti-icing systems such as hot-air systems for polymer composite airfoils can be challenging due to maximum operating temperature, and high thermal resistance of the polymer composites which pose a temperature limit for the hot air [4, 5, 7, 8].

A few hot-air and electro-thermal anti-icing systems [7, 9, 10] were developed for polymer composite materials, e.g. by using surface heating. But these studies did not consider energy consumption of these systems, and the effect of surface roughness as a result of installing surface mounted heating systems on aerodynamic efficiency. Also wind tunnel icing experiments were not conducted. Besides, electro-thermal anti-icing systems which are used in the form of thermal pads, electrically heated foils, and metal or carbon fiber electrical heating elements on the composite blades' surface, have serious drawbacks [4, 11, 12]. For example, thermal pads and electrically heated foils which are mostly mounted on the surface of the blade, change the aerodynamic performance of the airfoil, and disturb the air flow around the blade. Also, metal and carbon heating elements can attract lighting strikes to the surface of the blade. Carbon fibers as the thermal elements, which are positioned at the leading edge can also cause additional problems for the polymer composite blade, since they bear a large portion of the load which leads to cracks in the heating elements [4, 5, 11].

Currently, there are relatively few experimental studies in the icing conditions examining the performance of the anti-icing systems developed for composite airfoils; and most of

the studies are numerical analysis to model the heat transfer in the icing conditions or simulate the icing behavior of the airfoils [3, 13, 14].

Given the trend towards expanded use of composites for wind turbine blades and aircrafts, it is important to develop icing mitigation systems that are compatible with composite materials. In this study embedded thermal elements as an anti-icing system for polymer composite airfoils was investigated. The concept involves embedding thermal elements in the form of constantan wires inside a glass-fiber-reinforced/epoxy composite airfoil and heating the composite structure through these elements. The main goal of this study was to develop a new concept for anti-icing system for polymer composite airfoils which potentially may be used for, e.g. wind turbine blade. However, the intention is not as much on a specific application, but to investigate the feasibility of the new concept in a condition where ice can be formed. The idea is not to focus on icing conditions which lead to formation of the ice, or physics of ice formation. The intension is to study the functionality of the concept for using embedded thermal elements in a composite aerodynamic structure to prevent ice formation without thermal degradation of the composite material. The focus of this study is thermal behavior of the concept; and issues related to possible effects of embedding thermal elements on mechanical performance of composite test samples are not considered. As such, the study is focused on conceptual design aspects of the proposed anti-icing system, the energized airfoils' surface temperature profiles, and energy consumption; experimental as well as numerical methods are used.

The developed system can simply be incorporated during the manufacturing of a polymer composite structure such as airfoils. The embedded thermal elements will leave the exterior surface of the airfoil smooth unlike prior systems. In principle, this system can be customized; so that the temperature of different locations on the surface can be controlled to reach a specific anti-icing temperature to reduce energy consumption.

3.2 Experimental Methods

3.2.1 Manufacturing Process of the Composite Airfoils with the Anti-icing System

Polymer composite airfoils with embedded thermal elements as the anti-icing system were manufactured from a commercially available aerospace-grade fiberglass/epoxy prepreg, i.e., Necote E-765 epoxy/fiberglass prepreg from Park Electrochemical Corporation Advanced Material Technologies. Constantan wire, i.e. SPCC-010-50 with 0.25mm diameter, was used as the thermal elements in the anti-icing system, from Omega Engineering Inc.

The polymer composite laminates were fabricated by dry hand lay-up of six prepreg layers with total thickness of 1.4mm. The Anti-icing system is comprised of separate thermal elements (wires) embedded inside the composite airfoil. The thermal elements with equal lengths were sandwiched in between the composite laminate with desired spacing. Three layers of the prepreg were laid first, and then the thermal elements were aligned straight on them (perpendicular to the airfoil chord line), using a specially designed jig. Another three layers of the prepreg were laminated on top of the elements.

Figure 3-1(a) shows the designed jig with wires laid on the third layer (middle) of the composite laminate. As shown in Figure 3-1(a), the screws are placed at a specific distance from each other on the jig plate; and the wires can be kept straight with a specific spacing, using the screws.

After fabricating the composite laminates with embedded thermal elements, the laminates were formed into the airfoil profile, using a mold. Using the vacuum bag molding, the airfoil was cured in an oven for one hour at 82°C, followed by a two-hour cure at 135°C, applying a minimum vacuum pressure of 82kPa. The vacuum bag molding is used for improving the consolidation of the fibers, and removing excess resin, air and volatile compounds from the composite laminate. Figure 3-1(b) and Figure 3-1(c) show the two-part aluminum NACA 0021 airfoil's mold and the polymer composite inset. The final dimension of the composite airfoil inset is: 148mm (L) × 84mm (W) × 1.4mm (H).

In this study, two composite airfoil samples with two different thermal element patterns were made to study the effect of wire spacing on the airfoils' surface temperature distribution, and the effectiveness of the thermal elements' pattern for icing mitigation. First, composite airfoil labeled as: (I) had 11 equally spaced thermal elements with an equal length of 120mm; five thermal elements were placed on the top side, five on the bottom side, and one thermal element at the leading edge of the airfoil, as shown in Figure 3-2(a). The spacing of the thermal elements in this pattern was 10mm.

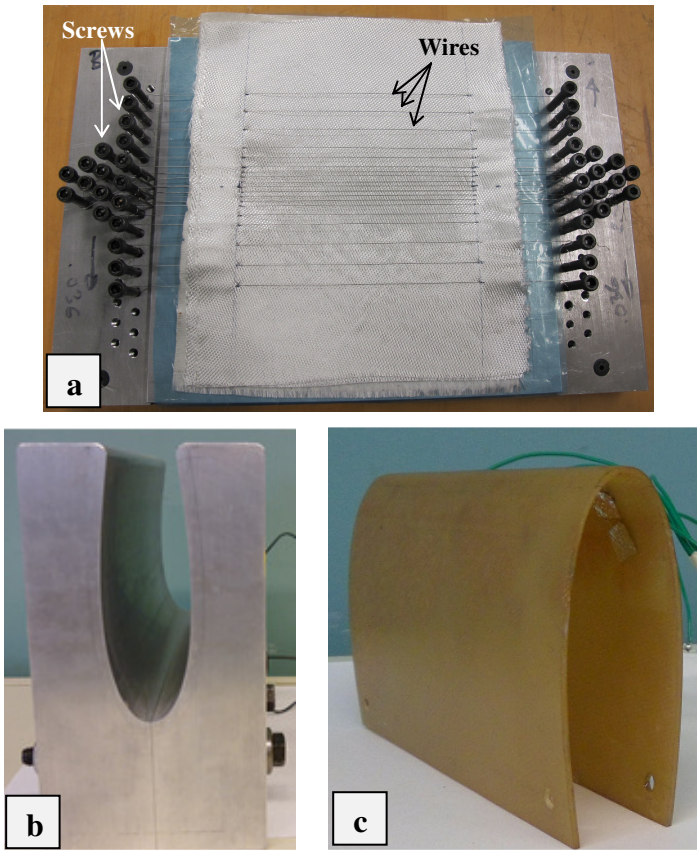

Figure 3-1- (a) The designed jig to lay the wires inside the composite laminate, (b) aluminum airfoil's mold, (c) the cured polymer composite airfoil inset.

The anti-icing system in the second fabricated airfoil, named airfoil (II), had 19 thermal elements with different wire spacing, but each wire had an equal length of 130mm. In airfoil (II), length of wires was 10mm longer than that of airfoil (I) for facilitating the wire connections to external conducting wires. The different wire lengths in airfoils do not affect the experimental results, since the middle section of composite airfoils was only considered in the tests and the edges of composite airfoil were not considered. Figure 3-2(b) shows the position of thermal elements inside the composite flat plate before shaping to an airfoil. As can be seen from Figure 3-2(b), one thermal element was embedded on the leading edge (wire 1), and the next four thermal elements till wires 2

and 2’ on the top and bottom sides of the airfoil (II), respectively, were placed with a 2.5mm spacing. This area, which considered as the leading edge region, is 3.42% chord length of the airfoil. The wires at the leading edge region were embedded closer than that of the area beyond leading edge region to increase the heat flux for the expected maximum convective heat transfer coefficient at this region.

Beyond the leading edge region, the convective heat transfer coefficient in the laminar regime decreases by thickening of the thermal boundary layer over the airfoil from the leading edge to the trailing edge. Also, a thermal element, i.e. wire 2-5, was placed in the mid-space between wires 2 and 3. The spacing between the rests of the thermal elements, beyond thermal element 3, is 10mm. Pattern of the thermal elements on the bottom side of airfoil (II) is similar to the top side, as shown in Figure 3-2(b).

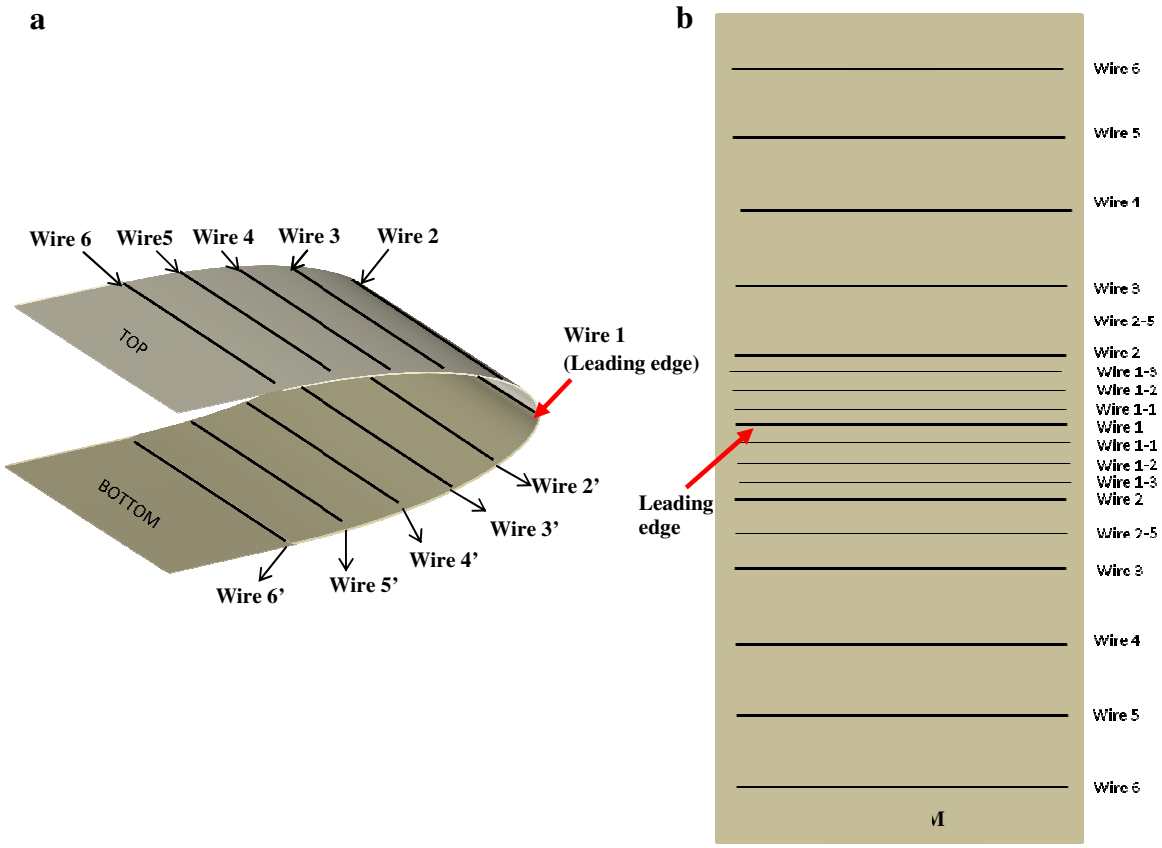

Figure 3-2- (a) Schematic of composite airfoil (I) with a total of 11 embedded thermal elements, (b) Thermal elements' spacing of airfoil (II) with a total of 19 embedded thermal elements before it has been shaped as an airfoil.

3.2.2 Experimental Setup

For tests, the composite airfoils were inserted in an aluminum airfoil (NACA 0021) frame which has the chord length of 146mm (see Figure 3-3(a)). The tests were done in an open loop low speed wind tunnel in cold (dry) and icing (wet) conditions to evaluate the actual performance of the anti-icing system. The airfoil was mounted inside the test section in the wind tunnel, which is a rectangular transparent section, 26cm (H), 30cm (L) and 38cm (W), as shown in Figure 3-3(a).

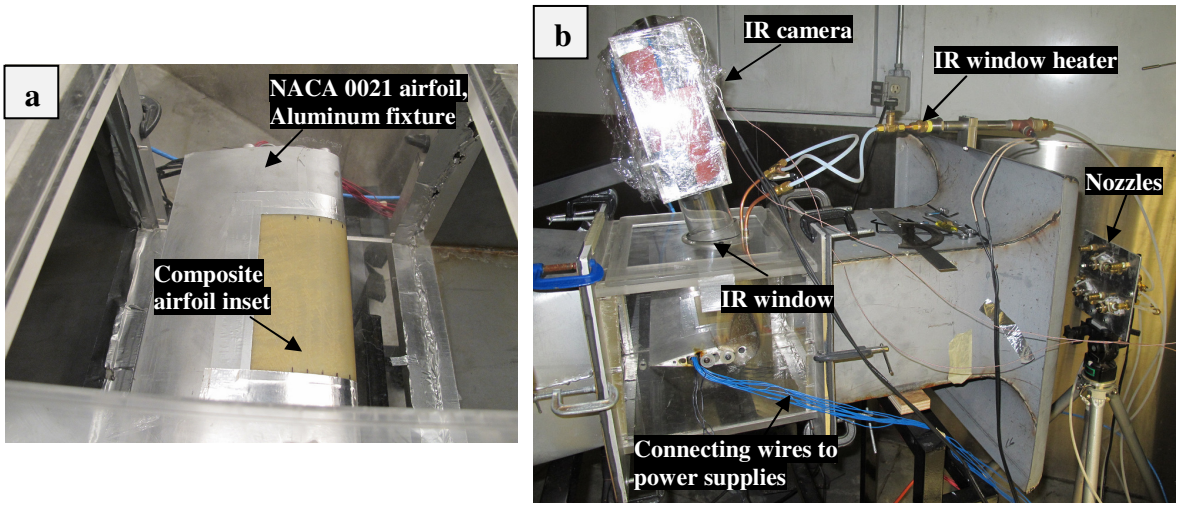

Figure 3-3- (a) The transparent test section in the wind tunnel and the NACA 0021 airfoil with the composite airfoil inset shown, (b) Experimental setup: wind tunnel, IR camera, and nozzles inside the cold room.

Conditions where icing can take place are wide and varied; it also depends on type of application, e.g. aviation or wind turbine industry. The main focus of this study has been on investigating the feasibility of the new concept in a single icing condition where ice can be formed, regardless of what conditions has led to formation of the ice. The selected icing condition used in the experiments can be representative of a very severe icing event for a wind turbine blade [3, 6, 12, 14, 15].

Icing (wet) tests were conducted at -17±1˚C under a maximum air velocity of 27.7m/s. The icing tests were run at two different water spray flow rates to investigate the effect of liquid water content (LWC) on the icing behavior of the composite airfoils. Water drop diameter (Volumetric Median Diameter, VMD) was chosen based on the water drops size in icing events such as fog, cloud and hydrometeor which is between 10 and 50μm [3]. From the manufacturer's specification of the air atomized nozzle (type 1/4J+SU16 Spraying Systems Co), the drop size at the air to water pressure of 551.6kpa to 413.7kpa

is ~50 microns and ~35 microns for water flow rates of 0.2kg/min and 0.16kg/min, respectively. Water drop temperature when hitting the airfoil is calculated to be between -1˚C to -2˚C, considering drop's initial temperature and time of flight. Icing test conditions is presented in Table 3-1. All icing tests were conducted three times for each composite airfoil inset.

Table 3-1- Icing (wet) test conditions.

Icing test condition	**Icing condition 1**	**Icing condition 2**
Air/water pressure (kPa)	551.6/413.7	551.6/413.7
Water drop diameter (VMD) (μm)	~50	~35
Water flow rate (kg/min)	0.2	0.16
Liquid Water Content (LWC) (g/m^3)	~1.05	~0.84
Icing test duration (minutes)	2	2
Angle of attack (AOA)	+2˚	+2˚

An A320 FLIR IR camera plus FLIR quick plot and Thermo Vision ExaminIR software were used for thermal imaging and study of the airfoils' surface temperature distribution. IR thermography was used to investigate the performance of the anti-icing system, and monitor the ice accretion and growth during icing tests [16]. For IR thermography of the airfoils in the cold (dry) and icing (wet) conditions, the IR camera was calibrated for the composite surface emissivity, airfoils profile considering its curvature, IR camera viewing angle, and IR window transmittance. The IR camera calibration for the effect of the airfoil's curvature on temperature measurements, showed that the IR camera can only measure the temperature of the leading edge area up to wire 1-3 (see Figure 3-2), and temperature of the top surface region from wire 2 up to wire 6 of the airfoils (I) and (II).

The experimental setup is shown in Figure 3-3(b). In Figure 3-3(b), the IR camera measures the top surface temperature of the airfoil through an IR window, mounted on the top surface of the transparent section of the wind tunnel. To measure the leading edge temperature of the airfoil, the IR camera was looking head-on onto the tunnel (this was only possible for dry test conditions).

The wires of the heating system were energized by power supplies. In the first set of icing experiments, equal powers were applied to all wires of airfoil (I) by connecting the 11 wires in a series circuit (power scheme 1 in Table 3-2). Then in the next set of icing tests, each wire of airfoil (I) was connected individually to the power supplies through a voltage regulator, as the power distribution system, to control the power distribution across the airfoil (power scheme 2 in Table 3-2). For airfoil (II), wires 3,4,5,6 were connected in series (for the top and bottom sides); so were wires 1-3, 2, and 2-5. The rest of the wires were connected individually to the power distribution system. The applied powers to the wires were decreased from the leading edge to the trailing edge to match the decreasing heat transfer over the airfoil from the leading edge to the trailing edge.

The input powers to the thermal elements of airfoil (I) are presented in Table 3-2. Power density is defined as the amount of power applied to a unit area of the thermal element's surface; it considers the length and diameter of the thermal element. The average power intensity is defined as the total applied power over the total heated surface area of the composite airfoil inset, i.e. area delimited by wires 1 and 6 on top and bottom of the airfoils.

Table 3-2- Input power to the thermal elements of airfoil (I) in cold dry and wet conditions.

Thermal element	Power scheme 1 (W)	Power density (kW/m^2)	Power scheme 2 (W)	Power density (kW/m^2)
1 (Leading edge)	6.0	56.6	13.9	131.3
2, 2’			14.0	132.4
3, 3’			7.7	72.8
4, 4’			4.3	40.9
5, 5’			2.8	26.8
6, 6’ (Trailing edge)			3.0	28.3
Total power (W)	66.0		77.8	
Average power intensity (kW/m^2)	5.0		5.9	

The applied power to each thermal element of airfoil (II) is provided in Table 3-3. In all of the icing tests to ensure the steady-state condition, the thermal elements were energized 5 minutes before starting the water spray in the icing tests.

Table 3-3- Applied power to the heating system of airfoil (II) in cold dry and wet conditions, to attain the stated powers, current and voltage were in the range of 2.1-3.7A and 1.4-4.5V, respectively.

Thermal element	Power scheme 2 (W)	Power density (kW/m^2)
1 (Leading edge)	10.1	89.0
1-1, 1-1’	9.1	79.9
1-2, 1-2’	8.7	76.6
1-3, 1-3’	5.6	49.0
2, 2’		
2-5, 2-5’		
3, 3’	4.9	43.4
4, 4’		
5, 5’		
6, 6’ (Trailing edge)		
Total power	118.7	
Average power intensity (kW/m^2)	8.3	

3.3 Results and Discussion

3.3.1 Effect of Airfoils' Surface Temperature on Icing

Thermal mapping of the energized composite airfoils' surface in the cold (dry) and icing (wet) conditions was used to understand the relation between the airfoils' surface temperature distribution, and the anti-icing performance of the heating system. The steady-state surface temperature distribution of airfoil (I) energized by power schemes 1 and 2 (Table 3-2), and airfoil (II) with energized heating elements by power scheme 2 (Table 3-3), were measured by the IR camera in the cold (dry) condition, before spraying water (see Figure 3-4). The surface temperature was measured at the mid section of the airfoils (see Figure 3-4). The reported temperatures are the average surface temperature from three tests on the airfoils.

Surface temperature of energized airfoil (I) with power scheme 1 (in Table 3-2), tested in cold (dry) condition, is shown in Figure 3-5(a). In Figure 3-5(a), the peaks show the temperature of the top surface of airfoil (I) on the thermal elements and the valleys are surface temperatures at the midpoints between thermal elements. Surface temperatures on top of the wires are higher than in-between the wires because of low thermal conductivity of the composite material. Surface temperature on the leading edge is the lowest compared to the surface temperature on other thermal elements. Surface temperature increases from the leading edge to the trailing edge due to the thickening of the laminar thermal boundary layer, and hence the decrease of convective heat transfer coefficient.

The flow over the airfoil is laminar as the maximum Reynolds number is ~1.5×10^5, and if one assumes insignificant turbulence in the wind tunnel.

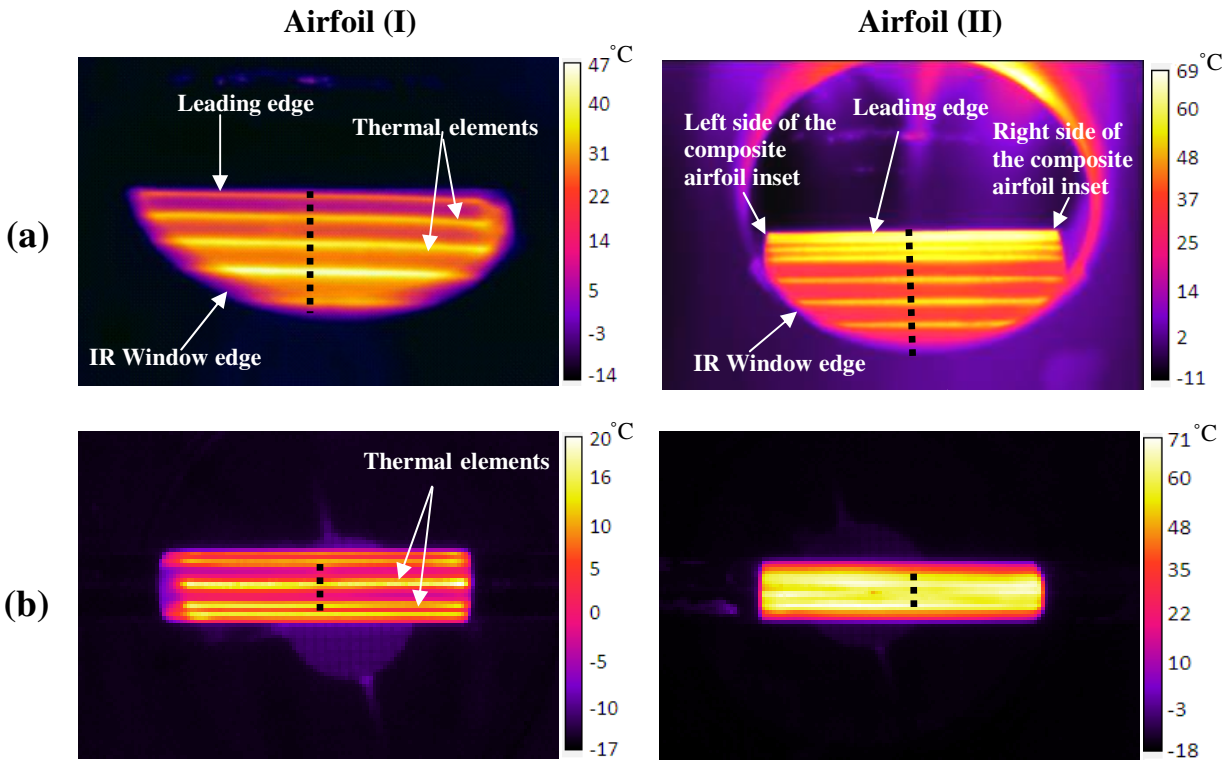

Figure 3-4- IR images of airfoil (I) energized by power scheme 1 (see Table 3-2), and airfoil (II) energized by power scheme 2 (see Table 3-3), before spraying water, (a) IR images of the top surface; (b) IR images of the leading edge as viewed head-on. The position of local temperature measurements are shown with the vertical black dashed lines. The crescent outline of the top surface IR image is due to round shape of the IR window; however, the front view of the leading edge is square since the camera directly viewed the leading edge (color figure on line). Magnifications of the images are different; however the scales have been adjusted in plotting data, e.g. in Figure 3-5.

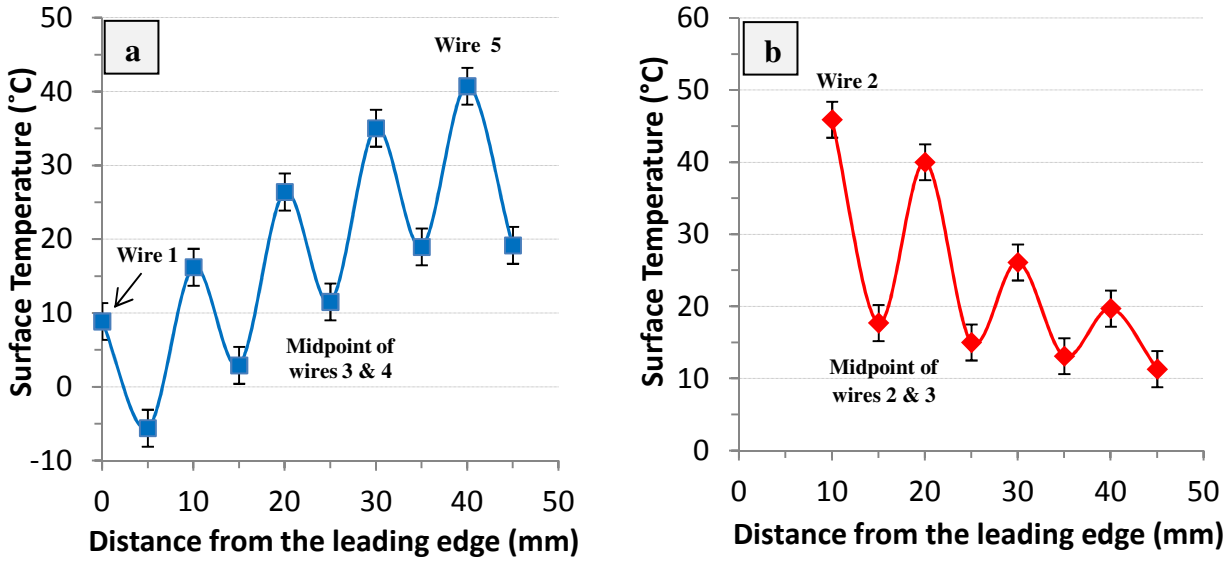

Figure 3-5- Surface temperature distribution for airfoil (I) captured by the IR camera in cold (dry) condition, (a) with equal input power to the thermal elements (power scheme 1 in Table 3-2), (b) with applied power scheme 2 (see Table 3-2); in (b), surface temperature of airfoil (I) leading edge region, i.e. wire 1 and midpoint of wires 1 and 2, was not measured. Lines are to guide the eye.

The minimum surface temperature of airfoil (I) is about -5.5˚C on the midpoint between wires 1 and 2 in the leading edge region (see Figure 3-5(a)). Surface temperature distribution in Figure 3-5(a) shows that equal input power to all of the thermal elements will not work to prevent ice accretion on the airfoil in the icing condition. This finding was also confirmed in icing tests as shown in Figure 3-6(a). As can be seen in Figure 3-6 (a), there was ice accretion on the leading edge area till wire 2, as expected. Also, there was ice between wires 2 and 3, between wires 3 and 4, and between wires 5 and 6, which shows that the surface temperature between the wires was not high enough to prevent icing. Figure 3-6(a) also shows that there is no ice on wires 3 to 6, which means that the surface temperature on wire 3 and beyond was sufficiently high to prevent icing. So, the airfoil's surface temperature on wire 3 before water spray in cold dry condition, i.e.

~26˚C, was considered as the minimum surface temperature to prevent ice accretion, beyond the wire 3 region.

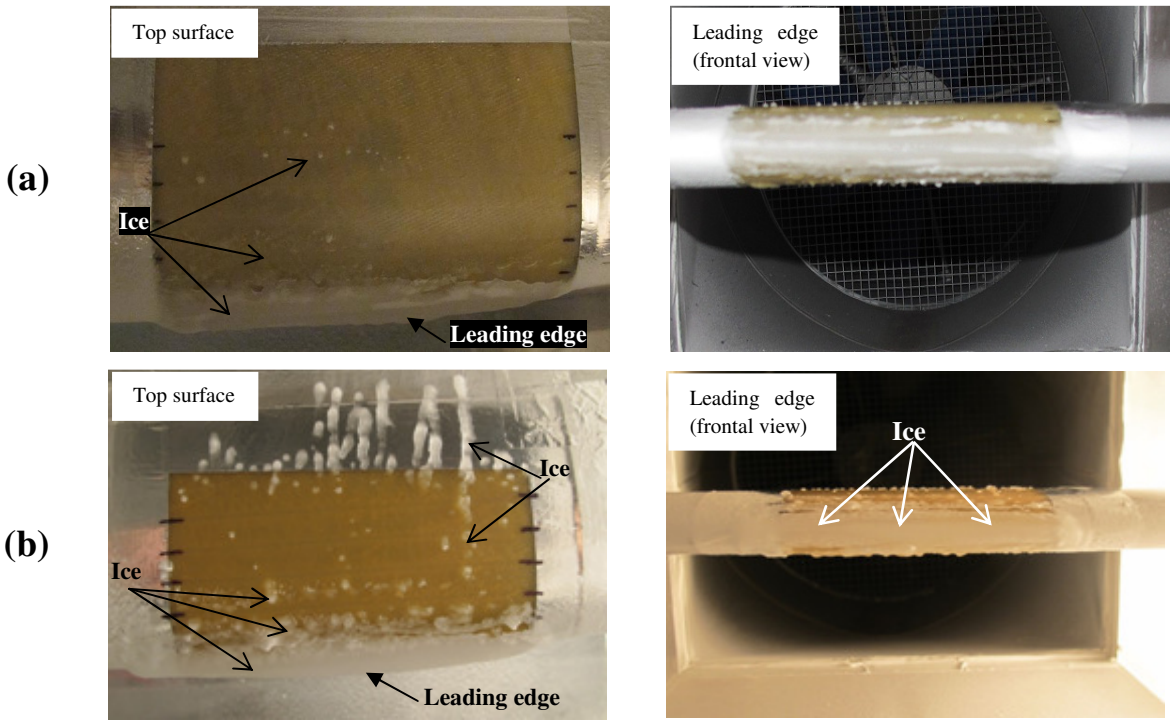

Figure 3-6- Icing behavior of airfoil (I) in icing condition 1 (see Table 3-1), (a) with applied power scheme 1 (see Table 3-2), (b) with applied power scheme 2 (see Table 3-2).

The icing experiments on airfoil (I) with an equal applied power to the wires also showed that the required power for the leading edge region is higher than that of the region beyond the leading edge area to have an ice free airfoil. So, to reduce the power consumption and to have an ice free composite airfoil, especially for the leading edge, the input power to each thermal element was controlled individually.

To prevent ice formation, one can change the power scheme, i.e. more power to the leading edge area, or change the wire pattern. Such flexibility is an advantage of the

proposed system of embedded thermal elements, that temperature distribution can be controlled by power manipulation (see Figure 3-5) or wire patterns (see Figure 3-4), or both.

Power scheme was changed first to investigate the effect of increased power level on surface temperature and distribution, and icing behavior of the leading edge region. In power scheme 2 for airfoil (I) (Table 3-2), the amount of applied power to wires 1-3 and 1-3' was increased; while the power level to wires 4-6 and 4'-6' was decreased due to the limited maximum capacity of our electrical system. Top surface temperature distribution of airfoil (I) in cold (dry) condition with power scheme 2 is shown in Figure 3-5(b). As can be noticed from Figure 3-5(b), this system does not seem to work as there are areas with temperature less than ~26˚C (note we had a limitation in power capacity of electrical supply system).

The icing behavior of airfoil (I) with the increased power level on the leading edge area is shown in Figure 3-6(b). As can be seen in Figure 3-6(b), although the temperatures of wires 1 and 2 were increased, ice still built up on the leading edge area. There is also ice between the wires, which verifies that the surface temperatures between the wires, shown in Figure 3-5(b), were not high enough to prevent ice accretion, as predicted. In Figure 3-6(b), the runback icing, i.e. ice that is formed from the water drops that run along the airfoil and then freeze once they reach unprotected cold region, was also observed beyond wire 6, which was expected in the unheated area beyond wire 6.

In further icing tests of airfoil (I) with individually controlled applied power to the thermal elements, the input power density to wires 1 and 3 were increased to 200kW/m^2 and 85kW/m^2, respectively. The input power to wire 2 was kept the same as provided in power scheme 2 (see Table 3-2); and the rest of wires were disconnected from the power supply due to the limited maximum capacity of our electrical supply system. These power levels are the power threshold, i.e. the maximum power which can be applied without thermal degradation of the polymer composite. In spite of applying maximum power levels to the leading edge area of airfoil (I), there was still ice accretion on the leading edge region (results not shown for brevity). This implies that the surface temperature on the leading edge between the thermal elements cannot be increased sufficiently by increasing the power levels of the wires due to the low thermal conductivity of the composite material; so spacing of wires need to be adjusted.

Also, comparison of Figure 3-5(a) and Figure 3-5(b) shows that surface temperature of airfoil (I) is more uniform for the region of wires 2 and 3 with the lower level of applied power. Surface temperature difference between the points above wire 2 and at the midpoint of wires 2 and 3 is about 12˚C for lower applied powers in Figure 3-5(a); while it reaches to ~28˚C when the input power to wires 2 and 3 increases in Figure 3-5(b). Surface temperature uniformity of airfoil (I) decreases by increasing the power levels of wires 2 and 3. Also, the surface temperature is more uniform in the region of wires 4 and 5 in Figure 3-5(b) because of less applied powers to wires 4 and 5. Although, increasing input power to the thermal elements increases surface temperature of the composite

airfoil, but surface temperature uniformity decreases by increasing the applied power levels to the heating system.

Given the maximum power one could safely transfer to the polymer composite and the maximum capacity of the electrical system, it is not expect that this system would work in icing condition. As a result, 10mm spacing of the wires near the leading edge area of the airfoil and its upper part cannot provide sufficiently high surface temperature and proper distribution, in the leading edge region, to prevent ice accretion. This led to changing the wire pattern, i.e. fabrication and study of airfoil (II). The minimum surface temperature of airfoil (II) beyond wire 3 region was kept at about 26˚C for the new design.

Comparison of the surface temperature of airfoils (I) and (II) in Figure 3-4 shows that the surface temperature of airfoil (II) near the leading edge is more uniform than that of airfoil (I). So, one can see how by changing the wire spacing, the surface temperature distribution and uniformity can be changed as needed.

The required power for individual thermal elements in different regions of airfoil (II) was adjusted to have an ice free composite airfoil, and reduce the amount of power consumption. Two important parameters were considered in adjusting the applied power; power threshold of the thermal elements to prevent thermal degradation of the polymer composite material, and the minimum applied power to the thermal elements to prevent ice accretion on the composite airfoil surface.

To reduce the power consumption of airfoil (II) heating system, the applied power at the leading edge area, which needed more power, was the maximum. The power was decreased by moving towards the trailing edge region. The total power applied to composite airfoil (II) was ~118.7W, and the power intensity was ~8.3kW/m^2. The total applied power to airfoil (II) is lower than the 131.8W input power to heat an aluminum airfoil with the same dimension at the same icing condition to prevent ice accretion [17]. Also, it was found that the required energy to have the leading edge of airfoil (II) devoid of ice was ~48% of the total applied power to the composite airfoil inset. The power intensity of the leading edge area, i.e. 25kW/m^2, was 4.9 times more than that of the rest of the airfoil, i.e. 5.1kW/m^2. According to the performed thermal analysis by ABAQUS simulation, provided in Section 3.4, the applied powers to the airfoils were safe to avoid thermal degradation of the polymer composite.

Surface temperature of airfoil (II) in the cold (dry) condition is presented in Figure 3-7. As can be seen from Figure 3-7, the trend of surface temperature changes over the composite airfoil from the leading towards the trailing edge conforms with the trend of heat transfer from the airfoil's surface.

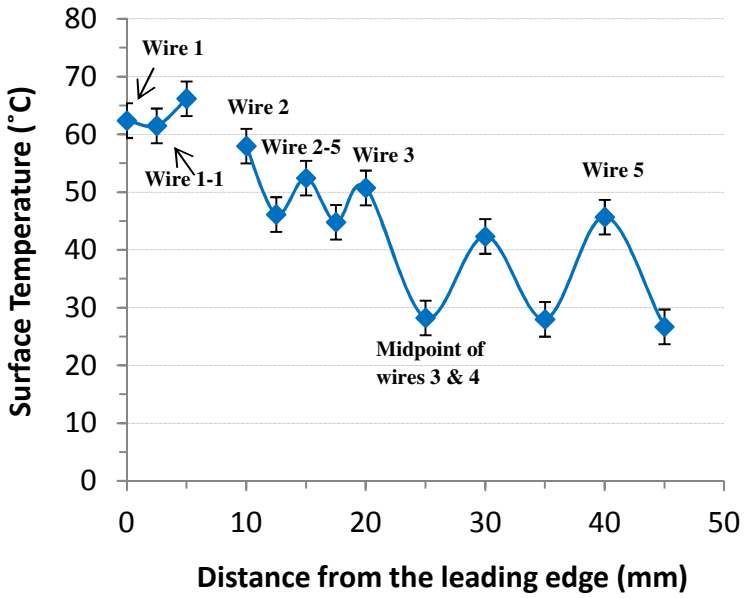

Figure 3-7- Surface temperature distribution of airfoil (II) with applied power scheme 2 (see Table 3-3), captured by the IR camera in cold (dry) condition. Line is to guide the eye.

The icing behavior of airfoil (II) in icing condition 1 is presented in Figure 3-8. As shown in Figure 3-8, the leading edge area and the top surface of airfoil (II) are free of ice, which verifies that the surface temperature was sufficiently high to prevent ice accretion on the airfoil. So, according to Figure 3-7, temperature of the leading edge region up to wire 2 should be ~60±3˚C to prevent ice build-up. Also, surface temperature between wires 2 and 3 should be ~45˚C-55˚C, and beyond wire 3 should be above 26˚C to have an ice free surface.

Figure 3-8 shows ice accumulation on the left side of airfoil (II). Further studies on the icing behavior of airfoil (II), which will be discussed in Sections 3.3.3 and 3.4, showed that ice accretion on the left side is due to the unheated aluminum edges of the fixture and the wires alignment defects during the composite airfoil fabrication process.

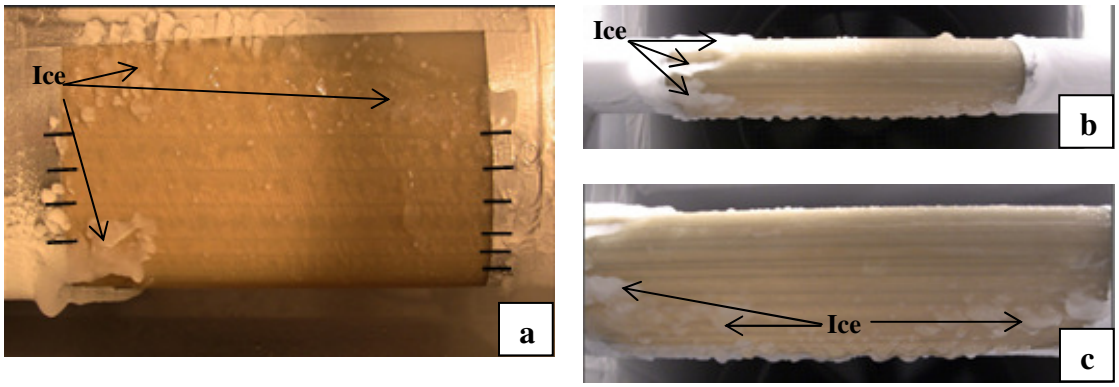

Figure 3-8- Icing behavior of airfoil (II) in icing condition 1 (see Table 3-1), (a) Top surface, (b) Leading edge, (c) Bottom surface of the airfoil.

Figure 3-8 shows that towards the trailing edge region of airfoil (II), runback icing occurs beyond the last thermal element, as there is no thermal element. Also, the bottom side of the airfoil has more ice than the top side due to a ~+2˚ AOA. The impingement surface area for the bottom side of the airfoil increases when the angle of attack increases. But, the collection efficiency, i.e. the fraction of the water in free stream which impacts a specific surface area of the airfoil, maybe about the same for different angle of attacks [3].

3.3.2 Effect of Water Spray on the Airfoil's Surface Temperature

The airfoils' surface temperatures were also monitored by the IR camera during icing (wet) condition; this was to investigate the effect of water spray on the anti-icing system performance and airfoil surface temperature. In the icing tests before spraying water, at the steady-state condition of the energized airfoils, the rate of the energy added to the airfoil by anti-icing system is equal to the rate of energy removal mainly by convection. During water spray (in the absence of ice formation), the heat is removed from the

surface by convection, and also energy used to bring the temperature of the liquid water from the initial to the final temperature [3]. So, after spraying water, surface temperature of the airfoil drops considerably.

Figure 3-9 shows the temperature of the selected points on the mid span of airfoil (II) top surface above the wires and at the midpoints between wires as a function of spraying time in icing (wet) condition 1 (Table 3-1). Water drops have a different temperature and emissivity than the airfoil (ice/drop has ~1% - ~4% lower emissivity than that of the airfoil [18]), and can interfere with surface temperature measurements (hence the fluctuations seen in Figure 3-9).

Figure 3-9 is only used to show the large surface temperature drop within the first 10 seconds of spraying water (15 seconds of icing test time), delimited with the black dashed line. Since the first significant temperature drop takes place within the first 10 seconds of spraying water, this is the time that ice will start to form, if the airfoil's surface temperature during water spray is not above water freezing point.

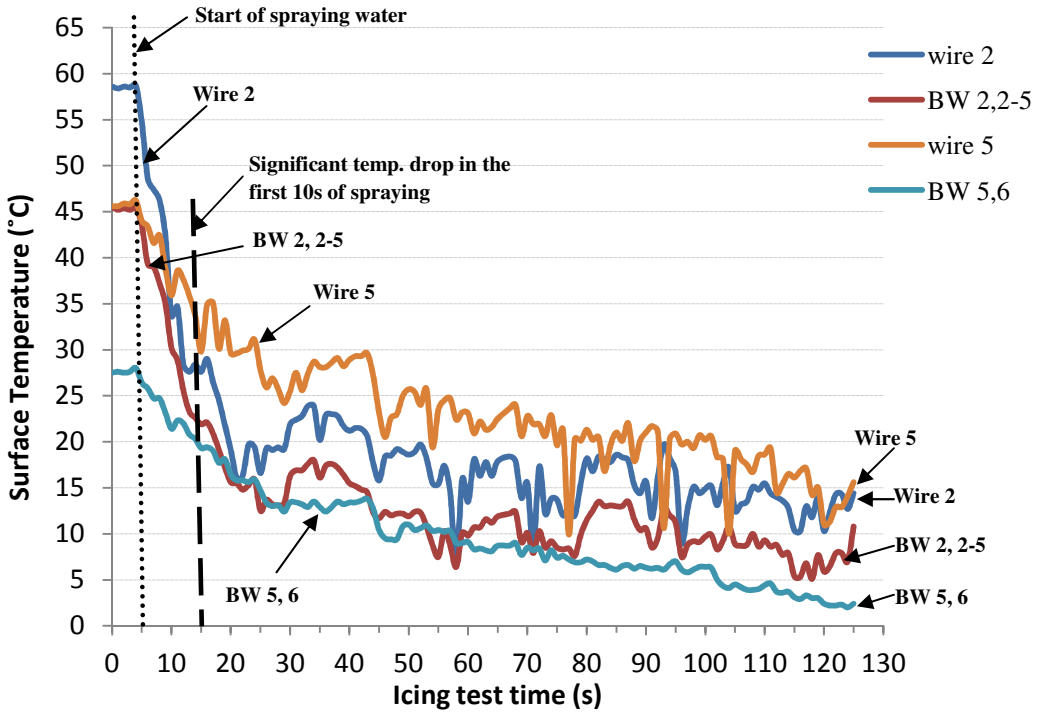

Figure 3-9- Graph of surface temperature as a function of icing test time for multiple points on the mid-span of airfoil (II) in icing condition 1 (see Table 3-1). "BW" in the legend represents the midpoint of wires which are numbered, (color plot online).

At the end of the 2-minute icing test period, as can be seen in Figure 3-8, there is no ice on the mid span area of the composite airfoil's surface, and also the residual water layer is insignificant due to the hydrophobic surface properties of the airfoil. So the measured surface temperature at the end of icing test shown in Figure 3-9 (at minute 2), can be considered as the surface temperature of the airfoil after stopping water spray. Figure 3-9 shows that the minimum surface temperature is about 2˚C, which is higher than the freezing point of the water. Figure 3-8 and Figure 3-9 verify that the surface temperature of the composite airfoil in icing (wet) conditions during water spray should be at least above 2˚C to prevent ice accretion on the airfoil surface, in these experiments.

Figure 3-10 represents the temperature drop of the selected points on the airfoil's top surface after 10 seconds of water spray, as a function of their distance from the leading edge. Temperature changes of the surface points in Figure 3-10 are derived from the data in Figure 3-9 by subtracting the temperature of the selected points before water spray and at 10 seconds after spraying begins.

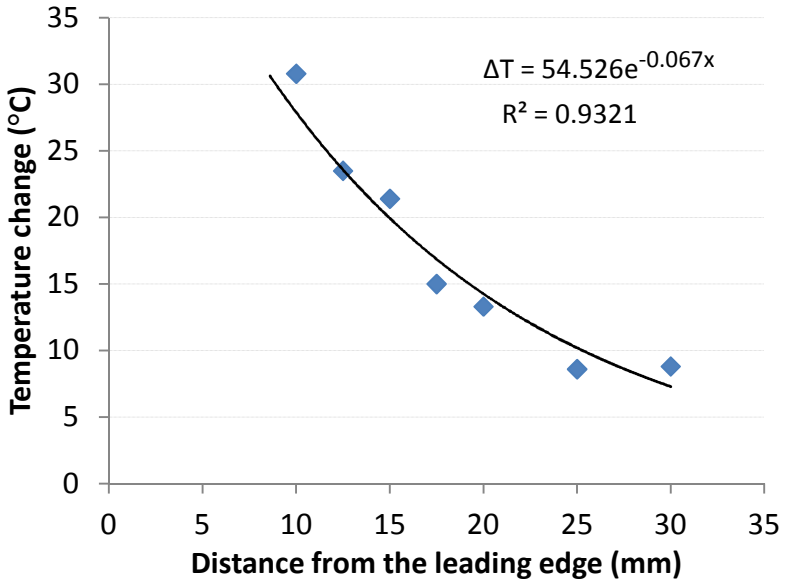

Figure 3-10- Plot of temperature changes for selected points, after spraying water, as a function of their distance from the leading edge for airfoil (II) in icing condition 1 (see Table 3-1). The solid curve is fitted to the data.

The fitted curve in Figure 3-10 allows for estimation of the temperature drop on the leading edge after water spraying, e.g. one can estimate a ~54˚C temperature drop at the leading edge after spraying water using the equation given in Figure 3-10. Comparing the leading edge temperature of airfoil (II) in cold (dry) condition, i.e. ~62˚C, with the estimated temperature drop of the leading edge, i.e. ~54˚C, after water spray, shows that the temperature of the leading edge would be above freezing point of the water. Since the

leading edge of airfoil (II) was free of ice during icing test, Figure 3-10 is a good representation of the temperature drop in relation to the distance from the leading edge.

3.3.3 Functionality of the Anti-icing System in Two Icing Conditions with Different LWCs

For better understanding of the anti-icing system functionality, and also determining the reason of icing on the left side of energized airfoil (II), further tests under icing condition 2 were done on airfoil (II). In Figure 3-11, the icing behavior of airfoil (II) in two different icing conditions is compared. As can be seen in Figure 11, the middle section (top and bottom) and right side of airfoil in both icing conditions were free of ice; while, there was ice accumulation on the left side, and run back icing towards the trailing edge of the top and bottom surfaces of the airfoil. As a result, the only observed change in icing between icing conditions 1 and 2 in Figure 11 was in the amount of collected ice, and not the ice location. So, the effect of drop size change in these experiments is not noticeable on the icing locations. Also, the drop size change from 50μm in icing condition 1 to 35μm in icing condition 2 does not noticeably affect the maximum local collection efficiency as shown in Ref. [3, 19]. Paraschivoiu and Saeed showed a ~5% increase in maximum local collection efficiency by changing drop size from 30 to 50 microns. So, the effect of drop size change in our experiments from 50 to 35 microns on the amount of accumulated ice is negligible compared to the effect of LWC.

Figure 3-11 shows that by decreasing LWC in icing condition 2 (see Table 3-1), the amount of ice on parts of the airfoil which had ice in icing condition 1, decreases. In spite

of forming less ice on the airfoil, there is still runback ice on the top and bottom surfaces of the airfoil and ice on the left side of the leading edge. This issue may be solved by using a superhydrophobic coating on the airfoil's surface [6].

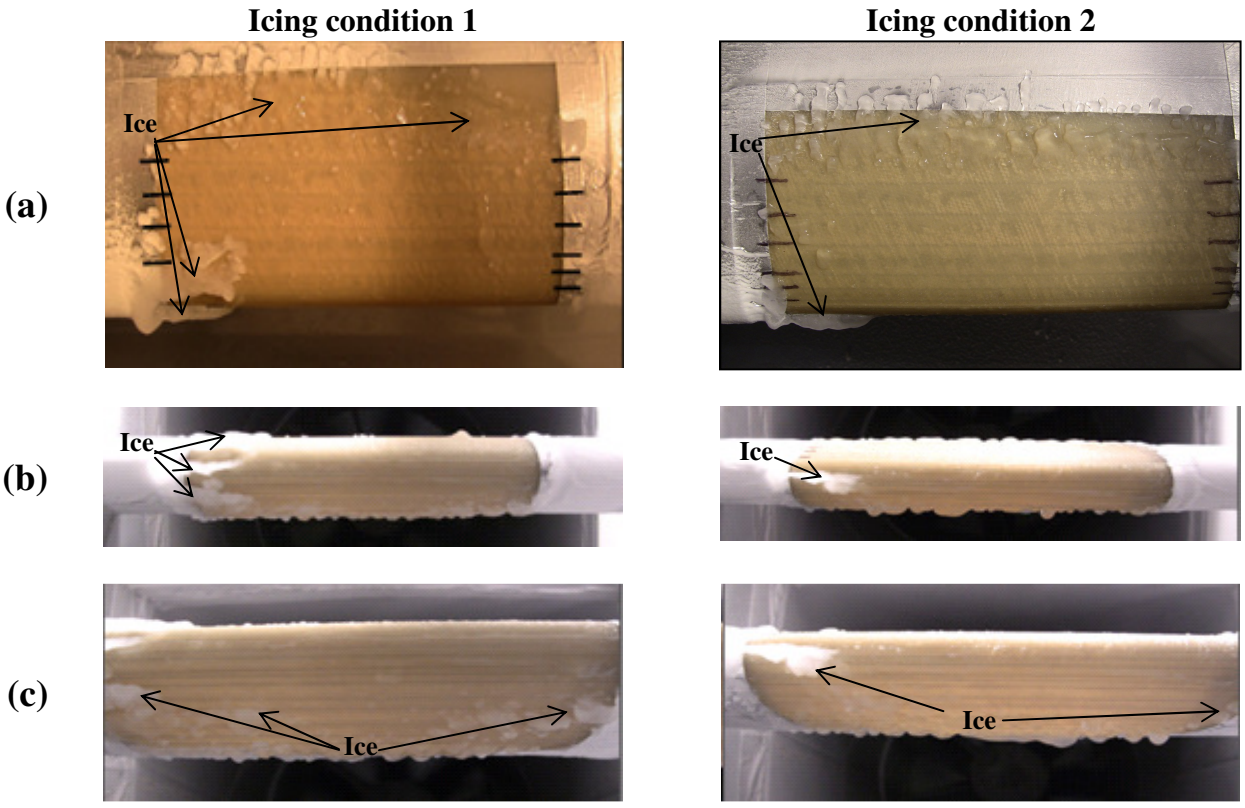

Figure 3-11- Comparison of icing behavior of airfoil (II) at different icing conditions 1 and 2 (see Table 3-1). (a) Top surface, (b) Leading edge, (c) Bottom surface of the airfoil.

The IR videos taken during icing test were used to investigate the reason of icing on the left side of airfoil (II) at different LWC in the icing conditions. Figure 3-12 shows a set of snapshots taken during the 2-minute icing test. It was found from Figure 3-12 that ice first accreted on the un-heated aluminum airfoil fixture edges, and then it grew from the edges towards the heated composite airfoil inset. As such, it created an impression that ice was formed on composite part of the airfoil. This ice was largely unattached to the

heated composite part of the airfoil. Ice accretion on the left aluminum edge was more than that of the right edge due to the airflow swirl induced by the fan.

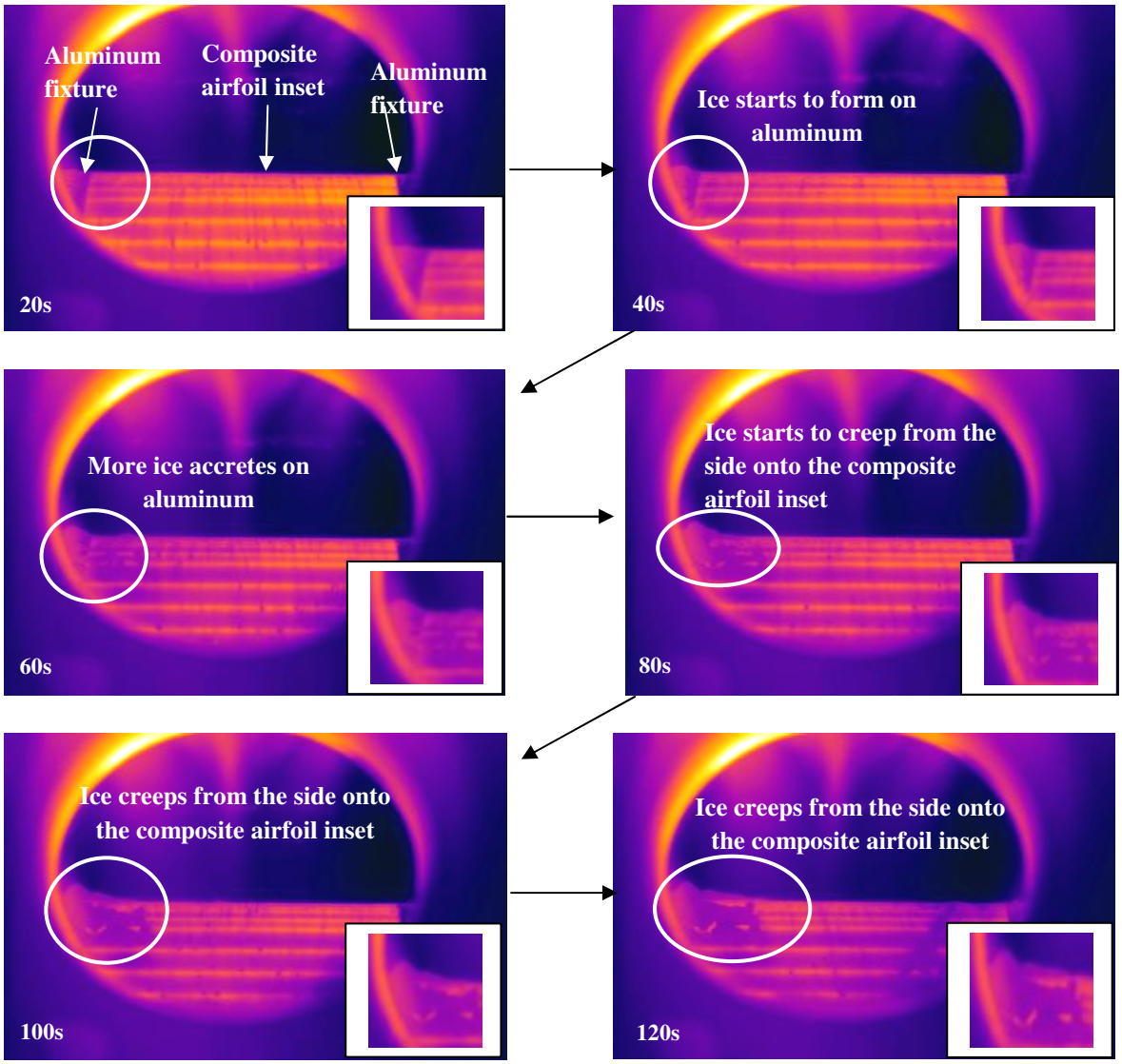

Figure 3-12- IR snapshots of the icing process of airfoil (II) in icing condition 1 (see Table 3-1), taken at 20 second intervals over the 2 minute icing test, icing on the left side of the airfoil is magnified on the bottom right corner, (color figure on line).

It was also further found that in airfoil (II), the elements were not equally spaced on the left side of the leading edge due to the uncertainties of composite airfoil manual

fabrication when forming the airfoil into the mold. Referring to Figure 3-2(b), spacing between wires 1-1' and 1-2', and between wires 1 and 1-1 is more than 3mm, instead of intended 2.5mm. Also, due to the displacement of wire 1-1', the spacing between wire 1-1' and wire 1 was less than 2.5mm on the bottom side. The displacement of thermal elements generally leads to a less uniform surface temperature distribution on the affected areas. These areas especially on the leading edge region would be susceptible to ice accretion. Thermal modeling in Section 3.4 for the leading edge region with different wires' spacing verifies this idea.

As can be seen in Figure 3-11, even with less LWC in icing condition 2, the ice formed on the left side of airfoil (II) leading edge area where wires are misaligned. The accreted ice on the aluminum edge grew towards the leading edge region with less uniform surface temperature distribution caused by the defects in the wires spacing.

Figure 3-11 also shows that in two icing conditions with different LWCs, there is no ice on the right and middle part of the airfoil's leading edge where 2.5mm spacing of wires is uniform. These results imply that for the applied power level to the leading edge region, critical spacing between wires on this area is 2.5mm to have a uniform surface temperature distribution for preventing ice accretion. It also emphasizes the precision and care that is required to fabricate such an anti-icing system.

3.4 Thermal Analysis

A simplified thermal model is developed in cold (dry) condition to:

1) Determine the power threshold in the anti-icing system to prevent thermal degradation of the polymer composite by simulating surface temperature of the embedded thermal elements (the upper limit for surface temperature for a given power).

2) Guide experiments by simulating the surface temperature distribution of airfoil in cold (dry) condition.

3) Verify the experimental results, where positions of the thermal elements inside the composite airfoil were changed.

This simplified thermal model in cold (dry) condition may be used in designing the thermal elements' spacing and location in the composite airfoil and also determining input power scheme. Our main focus in this study was developing an anti-icing system which can work in an icing condition without over heating the polymer composite airfoil which leads to degradation and burning of the composite material. The emphasis of this study was not on the icing phenomena or modeling the heat transfer during an icing event.

As a first step, surface temperature of the embedded thermal elements and the airfoils' surface temperature distribution were simulated by a steady-state two-dimensional thermal model, with a rectangular coordinate system:

$$\frac{\partial}{\partial x}\left(k_x \frac{\partial T}{\partial x}\right) + \frac{\partial}{\partial y}\left(k_y \frac{\partial T}{\partial y}\right) = 0 \quad (1)$$

where, x and y are position coordinates (m), T is temperature of the composite flat plate (˚C), k_x and k_y are thermal conductivities of the composite flat plate in x (fiber direction), and y (transverse to fiber direction) directions (W/m.K), respectively.

The composite material is considered as a single layer, due to its woven cloth fibers which have the same direction in different layers. It is also assumed that the transverse heat flux is continuous at ply interfaces.

Numerical thermal analysis for airfoil (II) has been done using ABAQUS software with the applied power values in Table 3-3. The simulation conditions were considered the same as cold (dry) condition in the wind tunnel experiments.

In the simplified heat transfer model of the airfoil, only half of airfoil (II) was modeled due to symmetry in the airfoil's shape and heat transfer condition; and airfoil was considered as a flat plate for simplicity and obtaining a first pass insight.

Figure 3-13 shows a schematic of the coordinate system of the composite flat plate with embedded thermal elements. The origin of xy coordinate system is at the left corner and at mid plane of the plate in Figure 3-13. The heat transfer from the top surface of the airfoil is mainly by forced convection (ignoring radiation heat transfer), and the bottom surface is assumed to be insulated, since there is no air movement inside the airfoil. The boundary conditions for the other two sides of the rectangle were considered adiabatic due to the symmetry of the system.

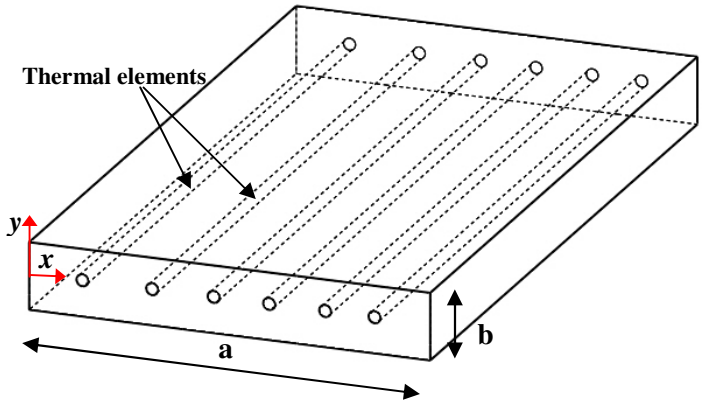

Figure 3-13- Schematic of composite flat plate with embedded thermal elements

Convective heat transfer coefficient over the airfoil surface was calculated using the "flat plate" approximation method [20, 21]. In this method the airfoil surface is considered as a combination of a cylinder on the leading edge and a flat plate beyond the leading edge. The known equations for the heat transfer from a cylinder and a flat plate was then applied to the airfoil surfaces. Local Nu numbers and the local convective heat transfer coefficients at central angle of, φ, from the stagnation point on a cylinder were calculated as follows [20]:

$$Nu_{\varphi} = hD/k = 1.14\ Pr^{0.4} Re_D^{0.5}\ [1-(\varphi/90)^3] \quad (2)$$

$$Re_D = UD/v \quad (3)$$

$$\varphi = (360/\pi)\ (s/D) \quad (4)$$

where, Nu_{φ} is the local Nusselt number over the cylinder at φ, Pr is Prandtl number, Re_D is Reynolds number of the cylinder (leading edge region) with diameter of D, h is the local convective heat transfer coefficient over the cylinder ($W/m^2.^{\circ}C$), k is thermal conductivity of the air (W/m. K), U is the free stream velocity, v is dynamic viscosity of

the air (kg/m.s), s is the curvilinear length measured along the airfoil surface from stagnation point over the leading edge region.

Following the calculation of local convective heat transfer coefficients on a cylinder, an average convective heat transfer coefficient "$h_{\text{ average}}$" was calculated for the leading edge region of the airfoil by [13]:

$$h_{\text{ average}} = \frac{1}{S}\int_s hdx = \sum_{i=1}^{3} h_i \ \Delta s_i \tag{5}$$

where, S is total length of the circumference of leading edge region, h_i is the local convection heat transfer coefficient of the selected points (i) on the leading edge surface, Δs_i is the difference between curvilinear lengths of two consecutive points measured along the airfoil surface from stagnation point over the leading edge region.

Heat transfer from the remainder of the airfoil, after the leading edge region, in the laminar flow, is calculated by considering the equations of a flat plate as follows [22]:

$$\text{Nu}_{\text{ave.}} = hL/k = 0.664\ \text{Re}_L^{0.5}\ \text{Pr}^{1/3} \tag{6}$$

$$\text{Re}_L = UL/\nu \tag{7}$$

where, Nu_{ave} is average Nusselt number over the entire plate, L is length of the flat plate region.

The modeling results showed that the maximum surface temperature of the thermal elements is 127.6˚C on wire 1-1 in the leading edge region of the airfoil. This

temperature is less than the maximum working temperature of the composite material, i.e. 137˚C [23]. It means that the applied powers (see Table 3-3) to different thermal elements in airfoil (II) are such that to prevent permanent damage to the composite material due to overheating.

The measured surface temperature of airfoil (II) by the IR camera from Figure 3-7, and the simulation results are compared in Figure 3-14. As can be seen in Figure 3-14, the simplified model predicts a slightly higher temperature over the wires than that of the measured ones. Whereas, the simulation results for temperature of the midpoints between the thermal elements is lower than that of the measured ones. Maximum temperature difference between the measured and simulation results on the airfoil's surface is about 13%. This is an acceptable outcome given the usual uncertainties in determining *h*, i.e. between 10-20% [22], and simplifications in the model. Also, the simulation results follow the same trend as the measured surface temperature in the experiments. Therefore, it seems that a simplified simulation presented can be used in designing the heating system and determining power thresholds to study thermal design of the proposed anti-icing system.

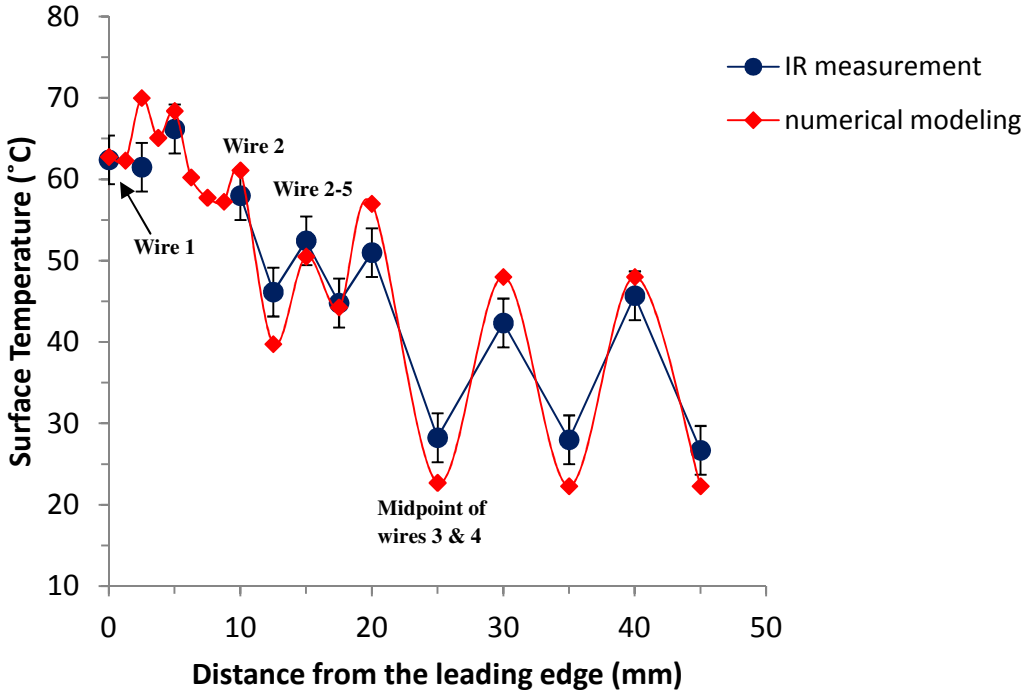

Figure 3-14- Comparison of simulated surface temperatures with the experimental data captured by the IR camera of airfoil (II) in cold (dry) condition, lines are to guide the eye.

The effect of thermal elements' position on airfoil (II) surface temperature distribution was also investigated. A simulation was performed for airfoil (II) with embedded wires positioned close to the airfoil surface. In these simulations, all the modeling parameters are the same as before, and only the positions of the thermal elements were changed from the middle plane of the airfoil thickness to the top most location near the airfoil's surface, i.e. 105μm under surface. The modeling results showed that surface temperature distribution of the composite airfoil with the embedded thermal elements close to the airfoil surface is less uniform than the airfoil with the thermal elements in the mid-plane of the airfoil thickness. So, an airfoil with the anti-icing system embedded in the mid-plane of the airfoil thickness, has a better performance in icing conditions. Details of these modeling can be found in [23].

Thermal modeling was also done for the leading edge region of airfoil (II) to investigate the effect of wires' displacement on the icing behavior of the leading edge. As described in Section 3.3.3, there was a misalignment between wires 1-1' and 1-2' and between wires 1 and 1-1 in airfoil (II) which led to have a smaller spacing between wires 1-1' and 1, and between wires 1-1 and 1-2, i.e. less than 2.5mm.

Figure 3-15 shows the surface temperature distribution of airfoil (II) on the leading edge region for wires alignment with equal 2.5mm spacing and displaced wires with 1.5mm spacing between wires 1-1' and 1, and between wires 1-1 and 1-2. As can be seen in Figure 3-15, surface temperature distribution on the leading edge region becomes less uniform when the spacing of wires is not equal to 2.5mm. Figure 3-15 shows that when wires 1-1 and 1-2 are close, a hot spot with temperature of ~80˚C and a cold spot with temperature of ~45˚C on the leading edge region appear. Also, in the case of smaller spacing between wires 1-1' and 1, a hot and cold spot at wire 1 with temperature of ~80˚C and ~52˚C, respectively, were seen. As discussed earlier, surface temperature of the leading edge region should be uniform and ~60˚C to prevent ice build-up.

Figure 3-15 shows that a less uniform surface temperature distribution results from displacement of wires from optimum position, affecting the performance of the heating system to hinder the ice formation. Thermal modeling results in Figure 3-15 verify the experimental results which showed ice accretion on areas of leading edge having non uniform wires' spacing.

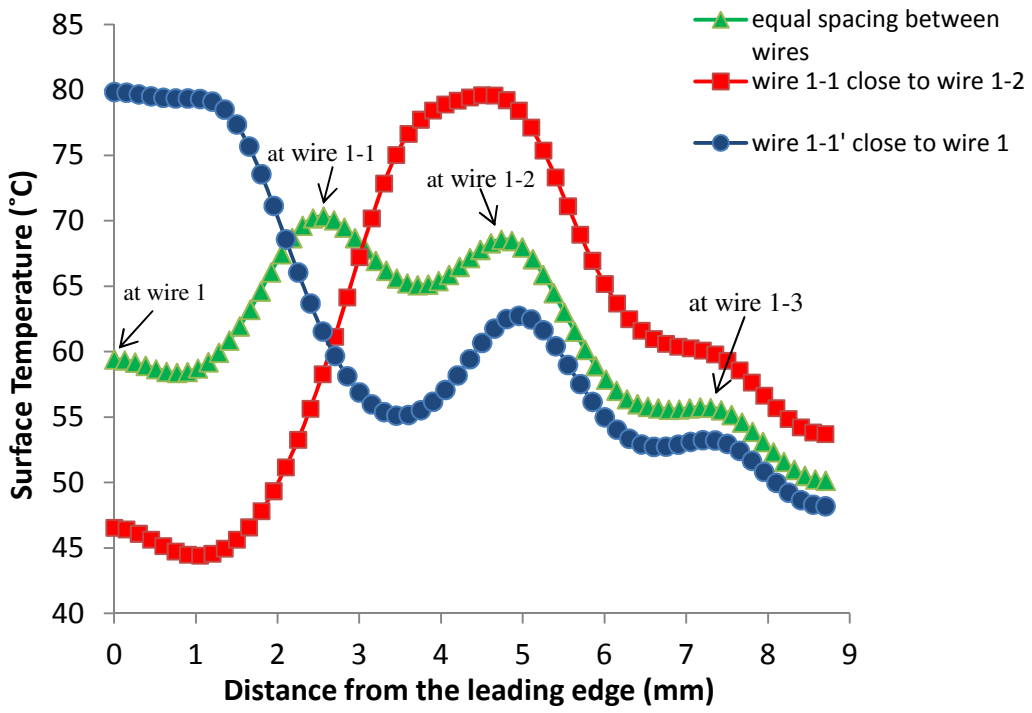

Figure 3-15- Comparison of temperature distribution on the leading edge region of airfoil (II) with equal 2.5mm spacing between wires and displaced wires with 1.5mm spacing between wires 1-1' and 1, and between wires 1-1 and 1-2, in cold (dry) condition with applied power scheme 2 (see Table 3-3). Note that these results are from simulations.

3.5 Summary and Conclusions

The concept of tailorable embedded thermal elements as an anti-icing system for the polymer composite airfoils was developed experimentally and numerically. Electrical wires as thermal elements were embedded in the composite airfoil using a specially designed jig. Airfoil (I) with 10mm spacing of wires could not provide sufficiently high surface temperature and a uniform temperature distribution to prevent icing. Since the leading edge region is the most susceptible area to ice accretion due to the maximum convective heat transfer over this area and liquid loading, the spacing between wires in this region should be less than 10mm. Airfoils' surface temperature distribution and

uniformity can be influenced by thermal elements' pattern and/or input power scheme; and power savings can be realized using both parameters. In cold dry conditions, the temperature on the leading edge region should be ~60±3˚C and the minimum surface temperature of the airfoil should be kept at ~26˚C to prevent ice accretion for the tested conditions. Icing tests with different water content showed that the amount of ice accretion is proportional to LWC; and drop size change from 50μm in icing condition 1 to 35μm in icing condition 2 has negligible effect on the amount of collected ice.

The total power consumption of 118.7W of this system was lower than that of 131.8W input power to a similar aluminum airfoil at the same icing condition. This verifies that the novel electro-thermal system is a promising anti-icing method for polymer composite structures with lower power consumption. The numerical thermal analysis in cold (dry) conditions was in a good agreement with the experimental results. It can be used in designing the anti-icing system, including the thermal elements' spacing and location, and required input power to the discrete wires of the heating system.

3.6 References

[1] Aircraft icing handbook, Civil Aviation Authority, 2000, http://www.caa.govt/, Accessed March 19, 2010, Chap. 1.

[2] S. K. Thomas, R. P. Cassoni, 1996, "Aircraft anti-icing and de-icing techniques and modeling", J. Aircraft, 33, pp. 841-854.

[3] G. Fortin, J. Perron, 2009, "Wind turbine icing and de-Icing", 47th AIAA Aerospace Sciences Meeting, Orlando, Florida, Paper No. AIAA-2009-274.

[4] H. Seifert, 2004, "Technical requirements for rotor blades operation in cold climate", BOREAS IV, 9-11 April, Pyhae, Finland.

[5] O. Parent, A. Ilinca, 2011, "Anti-icing and de-icing techniques for wind turbines: critical review", Cold Reg. Sci. Technol., 65, pp. 88-96.

[6] C. Antonini, M. Innocenti, T. Horn, M. Marengo, A. Amirfazli, 2011, "Understanding the effect of superhydrophobic coatings on energy reduction in anti-icing system", Cold Reg. Sci. Technol., 67, pp. 58-67.

[7] C. Hung, M. E. Dillehay, M. Stahl, 1987, "A heater made from graphite composite Material for potential deicing application", J. Aircraft, 24, pp. 725-730.

[8] G. Lubin, S. T. Peters, "Handbook of composites", Chapman & Hall, 2th ed., 1998, Chap. 3.

[9] S. W. Ciardullo, S. C. Mitchell, R. D. Zerkle, 1987, "Evaluation of capillary reinforced composites for anti-icing", AIAA 25th Aerospace Sciences Meeting, Reno, Nevada, Paper No. AIAA-87-0023.

[10] Expert group study on "Wind Energy Projects in Cold Climates", Edition 2005, http://virtual.vtt.fi/virtual/arcticwind/reports/recommendations.pdf, Accessed March 19, 2010.

[11] N. Dalili, A. Edrisy, R. Carriveau, 2009, "A review of surface engineering issues critical to wind turbine performance", Renewable Sustain. Energy Rev., 13, pp. 428-438.

[12] G. Fortin, C. Mayer, J. Perron, Sep. 2008, "Icing wind tunnel study of a wind turbine blade deicing system", Sea Technol., 49, pp. 41-44.

[13] R. Elangovan, R. F. Olsen, 2008, "Analysis of layered composite skin electro-thermal anti-icing system", 46th AIAA Aerospace Science Meeting and Exhibition, Reno, Nevada, Paper No. AIAA-2008-0446.

[14] X. Wang, "Convective heat transfer and experimental icing aerodynamics of wind turbine blades", University of Manitoba, PhD thesis, August 2008.

[15] A. G. Kraj, E. L. Bibeau, 2010, "Phases of icing on wind turbine blades characterized by ice accumulation", Renewable Energy, 35, pp. 966-972.

[16] M. Mohseni, M. Frioult, A. Amirfazli, "Simultaneous monitoring of ice accretion and thermography of an airfoil: An IR imaging methodology", submitted to Measurement Sci. Technol., 2012.

[17] M. Innocenti, "Superhydrophobic coating for mitigating icing of airfoils", University of Bergama, M.Sc. thesis, March 2009.

[18] FLIR Systems, Inc., "User's manual for FLIR A320 & A325", 2008.

[19] I. Paraschivoiu, F. Saeed, "Aircraft icing", John Wiley & Sons, Inc.

[20] H. Sogin, "A design manual for thermal anti-icing systems, WADC Technical Report 54-313, December 1954.

[21] L. M. Boelter, L. M. Grossman, R. C. Martinelli, E. H. Morrin, "Investigation of Aircraft Heaters: Comparison of Several Methods of Calculating Heat Losses from Airfoils", NACA TN 1453, 1948.

[22] Y. A. Çengel, "Heat and mass transfer: a practical approach", McGraw-Hill, 3rd ed., 2007, Chap.7.

[23] M. Mohseni, "Development of a novel electro-thermal anti-icing system for fiber-reinforced polymer composite airfoils", University of Alberta, M.Sc. thesis, May 2012,

Appendix C, “Thermal analysis of the polymer composite airfoil with the anti-icing system”.

4. Simultaneous Monitoring of Ice Accretion and Thermography of an Airfoil: An IR Imaging Methodology*

4.1 Introduction

Icing of aerodynamic structures such as wind turbine blades and aircraft wings adversely impacts the aerodynamic properties of the airfoil. Ice accretion on the airfoils' surfaces leads to loss of lift, increased drag, and weight of an airfoil. As such icing can affect flight safety or safe and efficient operation of wind turbines.

Ice accretion on an airfoil's surface occurs when supercooled water drops which are in a metastable condition interact with the solid surface at a temperature range of -40°C to 0°C. There are different types of icing phenomena depending upon the atmospheric conditions such as the atmospheric temperature, the volumetric mean diameter of the water drops, and the liquid water content [1, 2]. The size, shape and properties of the accreted ice also depend upon the geometry of the airfoil, the air speed and the collection efficiency [2, 3].

To mitigate icing problem efficiently, and apply optimized anti-icing/de-icing strategies, it is important to predict the type, shape, and extent of ice accretion. Monitoring of ice accretion and growth can be used in determining the type of ice and its accumulation rate

* This chapter has been submitted to Measurement Sci. Technol. J., Mohseni, Frioult, Amirfazli, 2012.

at various icing conditions on the surface of airfoils. These results can be used as an indication of the ice severity and the required mitigation strategy to control the ice accretion on the airfoil's surface. Also, the rate and shape of ice accretion can be used in optimizing the geometric parameters of an airfoil to minimize the ice accretion on the airfoil's surface [3].

Since methods to combat icing usually involve heating, thermography information is needed to design the heating system properly. Rarely, if at all simultaneous information about temperature field and ice accretion is obtained with current techniques, but such information is imperative for energy efficient design of an anti-icing system. Knowing the correlation between the icing pattern and surface temperature evolution during icing test period can allow better understanding of anti-icing system performance and in general physics of ice growth.

Icing behavior of airfoils including wind turbine blades and wings has been investigated experimentally in different icing conditions [1, 4, 5]. In all of the experimental studies, a digital camera was used to investigate the ice growth pattern and rate of ice accumulation during icing experiment. In most of the experimental studies, the final ice pattern at the end of icing experiment was recorded, and no pattern of ice growth during icing test was presented e.g. [1, 4]. There are also multiple studies to predict icing phenomena on an airfoil's surface using numerical simulations e.g. [2, 6, 7].

The main methods to measure the surface temperature of an airfoil are attaching thermocouples directly on to the outer surface of an airfoil[8, 9], which is an intrusive process, or its inner surface [10, 11], which may not be proper to measure surface temperature of composite airfoils due to their high thermal resistance. The use of thermocouples to measure the surface temperature both in a wind tunnel and in actual flight has been investigated [8, 9]. However, even though the thermocouples are very thin, they could still have an effect on the surface profile which in turn would change the airflow over the airfoil. Use of thermocouples also at best provides a discrete and sparse picture of temperature field.

In this study, infrared images were taken of an airfoil's surface during the icing tests in cold (dry) and icing (wet) conditions, and were used to monitor the surface temperature of an airfoil, as well as ice accretion rate and pattern. We used an airfoil made of composite material which was equipped with a newly developed electro-thermal anti-icing system as described in [12]; basically thermal elements were embedded in the airfoil.

The main contribution and importance of this work is to simultaneously obtain ice location and temperature field information, as well as monitoring the evolution of ice or potentially drops running on the airfoil. The focus of this paper is to introduce and demonstrate the utility of the methodology presented; it is not an icing study. To the best of our knowledge this is the first study for monitoring simultaneously the airfoil's surface temperature and ice accretion and growth pattern using an IR technique.

4.2 Methodology

Conditions where icing can take place are wide and varied; it also depends on type of application, e.g. aviation or wind turbine industry. The main focus of this study has been on methodological developments to allow simultaneous study of icing and thermal profile of an airfoil during an experiment where ice forms, regardless of what conditions has led to formation of the ice. Nevertheless, the selected icing condition used in our experiments can be representative of a very severe icing event for a wind turbine blade [5, 7, 10, 13, 14]. Icing (wet) tests were conducted at -17±1˚C with an air velocity of 27.7m/s with high liquid water content, LWC (1.05g/m^3) (see Table 4-1). Water drop diameter (Volumetric Median Diameter, VMD) was chosen based on the water drop size in icing events such as fog, cloud and hydrometeor which is between 10 and 50μm [7]. The air atomizer nozzle (type 1/4J+SU16 Spraying Systems Co) used to generate drop cloud in our tests, produced drops of ~50 μm VMD, when operated at the air to water pressure of 551.6kPa to 413.7kPa, and water flow rate of 0.2kg/min.

Table 4-1- Icing (wet) test condition.

Parameter	**Value**
Air/water pressure of air atomized nozzles (kPa)	551.6/413.7
Water drop diameter (VMD) (μm)	~50
Water flow rate (kg/min)	0.2
Liquid Water Content (LWC) (g/m^3)	~1.05
Icing test duration (minutes)	2
Angle of attack (AOA)	+2˚

Temperature distribution and ice accretion on a polymer composite airfoil surface, equipped with an electro-thermal icing mitigation system, was monitored in an open loop low speed wind tunnel in icing (wet) condition. The composite airfoils were inserted in an aluminum airfoil (NACA 0021) frame which has the chord length of 146mm (see Figure 4-1). The NACA 0021 airfoil was mounted inside the test section in the wind tunnel, which is a rectangular transparent section, 26cm (H), 30cm (L) and 38cm (W), as shown in Figure 4-1 and Figure 4-2.

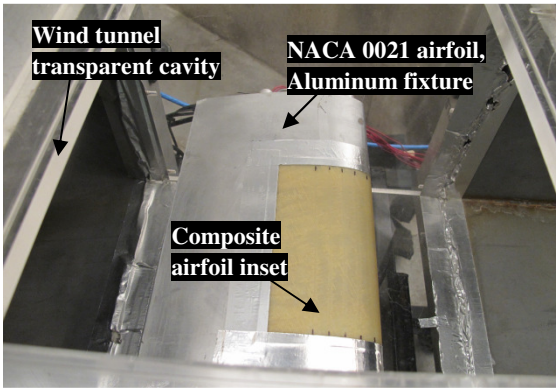

Figure 4-1- The transparent test section in the wind tunnel and the NACA 0021 airfoil with the composite airfoil inset shown.

4.2.1 Measurement Techniques

An A320 FLIR IR camera with a 10mm/45˚ lens plus FLIR quick plot and Thermo Vision ExaminIR software were used for simultaneous thermal imaging and monitoring of ice accretion on the airfoils' surface. Based on the IR camera distance from the target (composite airfoil), type of the lens, and its' sensor resolution, i.e. 320×240 pixels, the spatial resolution (pixel size) was 0.73×0.73mm/pixel in the experiments. Imaging was

done at 2 frames per second, and the captured images were stored in a computer for subsequent analysis.

The experimental setup is shown in Figure 4-2. As can be seen in Figure 4-2, the airfoil was mounted inside a transparent section in the wind tunnel. The IR camera was placed above the transparent section to measure top surface temperature of the airfoil through an IR window. The IR camera was calibrated for the composite surface emissivity, airfoils profile and curvature, IR camera viewing angle and IR window transmittance (details can be found in [12]). In icing (wet) conditions, the IR window should be ice free to have the thermal images of the airfoil. So, the IR window was protected from icing by a layer of warm air blowing over the inner surface of the IR window (see Figure 4-2).

To have the supercooled water for spraying in the icing condition, the water was cooled outside the testing room in a pressurized tank in the refrigerator. Water was then sprayed into the wind tunnel using the air atomized nozzle type 1/4J+SU16, (Spraying Systems Co.). Sprayed water drops become supercooled during the flight towards the airfoil. Water drops temperature at nozzles is ~0˚C, and when hitting the airfoil, its temperature was calculated to be between -1˚C to -2˚C.

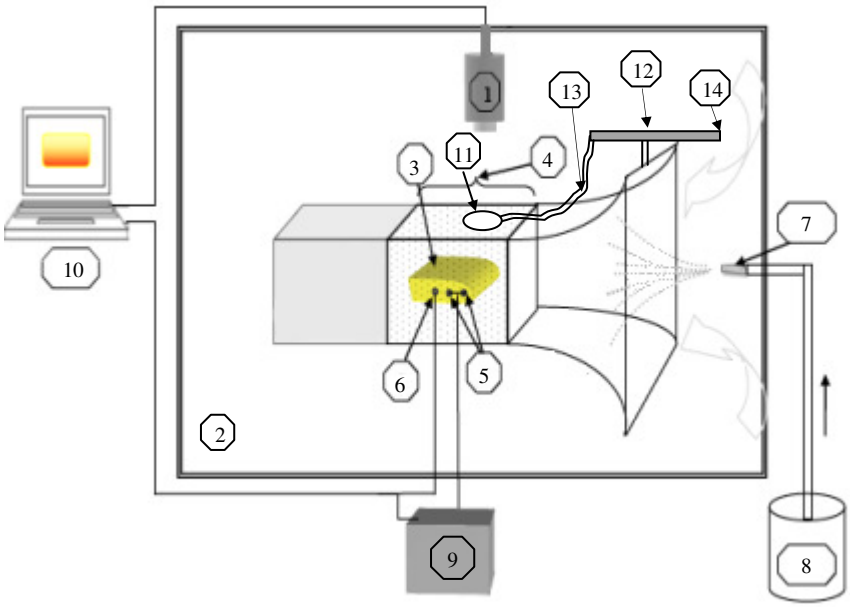

1- IR camera	5- Airfoil heating system	9- Power supply	13- Warm air tube
2- Cold room	6- Thermocouples	10- PC	14- Heater inlet, Connected to compressed air (not shown)
3- Polymer composite airfoil	7- Air atomizing nozzles	11- IR window	
4- Transparent cavity	8- Cold water tank	12-IR window air heater	

Figure 4-2- Schematic of the IR thermographic imaging for the polymer composite airfoil in the open icing wind tunnel setup.

The icing mitigation system of the airfoil was connected to the power supplies, located outside of the testing cold room. This system was comprised of discrete thermal elements embedded in the composite airfoil insert; details can be found in [12]. In all of the icing tests to reach the steady-state condition, the thermal elements were energized 5 minutes before starting the water spray in the icing tests. Icing experiments were conducted for 2 minutes; and IR videos from top surface of the energized airfoil were recorded during the icing test period using FLIR quick plot software.

In this study, icing (wet) tests were done using two composite airfoils with different thermal element patterns for the anti-icing system. Airfoil (I) had 11 equally spaced

thermal elements with 10mm spacing; whereas, airfoil (II) had 19 thermal elements with different wire spacing; the thermal elements at the leading edge region were embedded closer than that of the area beyond leading edge region. So, the ice accretion and growth pattern was different on the airfoils due to their different surface temperature distributions. To demonstrate the feasibility of the proposed methodology, IR videos taken from airfoils (I) and (II) in the icing tests were analyzed and presented.

4.2.2 Post Processing Methodology

Using FLIR quick plot software, IR videos in two types of color map showing temperature profile, i.e. “rain 10” and “gray” of FLIR quick plot software, were recorded (see Figure 4-3). The recorded IR videos were processed with MATLAB image processing tools. “Rain 10” color map (see Figure 4-3(a)) was used for surface temperature measurements (thermography), and “gray” color map (see Figure 4-3(b)) was used for monitoring ice accretion and growth. Color bars in Figure 4-3 represent surface temperature distribution of energized composite airfoil (I) inset in cold (dry) condition.

IR videos were first changed to IR images using an in-house MATLAB code. A 2 min IR video strip of icing test consisted of 240 IR images/frames, considering the IR camera speed, i.e. 2 frames per second. The IR frames were in an RGB (red, green, blue) color format. The IR images were processed for simultaneous monitoring of the ice accretion and thermography of the airfoils, as described below.

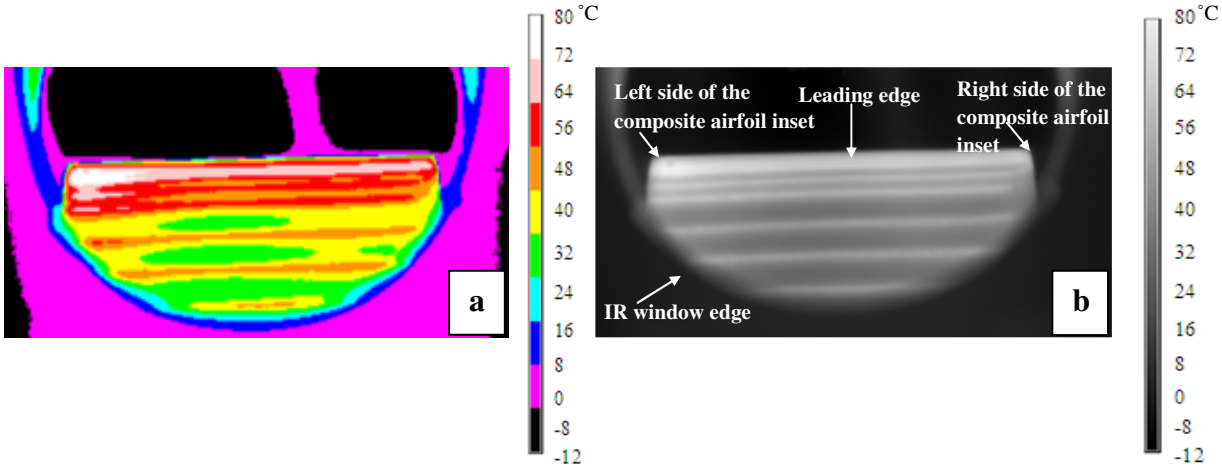

Figure 4-3- IR image of energized composite airfoil (I) insert in cold (dry) condition (top view), (a) "rain 10" color map IR image, (b) "gray" color map IR image; the main object in the IR image is the composite airfoil surface which can be seen through the IR window, the rest of image is irreverent in the image processing; The crescent outline of the IR image is due to round shape of the IR window edge; (color figure on line).

4.2.2.1 Thermography of the Airfoil's Surface

The airfoil's surface temperature during icing test was measured from each "rain 10" color map IR image using FLIR quick plot software. Temperature profile of the airfoil's surface was used to monitor surface temperature evolution during icing test period.

4.2.2.2 Monitoring of Ice Accretion and Growth

An algorithm in MATLAB was developed to process the "gray" color map IR images automatically to monitor ice accretion and growth pattern on the airfoil's surface during icing test period. The output of every step of the procedure is shown in Figure 4-4, and briefly described as follows:

(1) Each IR image frame was loaded as 8 bites RGB (red, green and blue) color format (Figure 4-3).

(2) Each frame was converted from RGB (3D) mode to grayscale mode (2D) (Figure 4-4 (a)) with MATLAB functions. 2D images were devoid of color dimension of the IR images.

(3) To remove the IR image noise, a median filter was applied to the images (Figure 4-4 (b)). Median Filtering (medfilt2), which is a non-linear operation, is often used for removing salt and pepper noises [15]. A median filter is more effective than convolution filtering when the goal is to reduce noise and preserve edges, simultaneously [15]. Our investigation [12] showed that, "medfilt2" function was more efficient in removing noises in the IR images than "imfilter" filtering function, which is a linear filtering of multidimensional images, and works in two filtering modes of convolution or correlation [15].

(4) The IR images contrast was enhanced using histogram equalization, i.e. "histeq" function. The resulting image is depicted in Figure 4-4(c). IR images can be blurred images with strong noise and a low target to background contrast [16]. To detect and track the target more precisely in 2D infrared images, it is important to enhance the contrast of the image. We found [12] that "histeq" function was more effective in enhancing IR images than "imadjust" function, which enhances an image through adjusting the intensity values or color map of the image [15].

(5) Ice was detected by a gradient operator. Edge detection is a traditional method in detecting a target in infrared images [16, 17]. Different edge detection operators including Roberts, Canny, and Sobel were used to detect edge of the ice as the target in actual infrared images. It was found [12] that Sobel operator detects the boundary of major icing better in noisy IR images than other edge detection operators [15]. Since

Roberts operator is sensitive to noise, and Canny operator detects both the strong and weak edges, so, they cannot produce a clean edge detected image from noisy IR images. Sobel operator creates images like the one shown in Figure 4-4(d).

(6) Detected edges due to the IR window outline, moving water drops on the heated airfoil's surface, and non-uniform surface temperature distribution of the airfoil were removed from the edge detected images. In this study we were interested in detecting major icing of the airfoils which deteriorates the airfoil performance. So, detected minor icing on the airfoil surface were also removed from the processed IR images by visual inspection. In the removing step, the area on edge detected images which needed to be devoid of noises and minor icing was selected by visual inspection and cleaned using the MATLAB code developed. The image was also inversed to change the background color to white. The resulted image is shown in Figure 4-4(e).

7) The processed grayscale images (2D) were again converted to RGB mode (3D). The processed infrared images showing ice growth pattern should be in 3D so it can be combined with the original "rain 10" color scale of the IR images which shows surface temperature distribution of the airfoil; this allows to have combined information in a single frame/image for the airfoil.

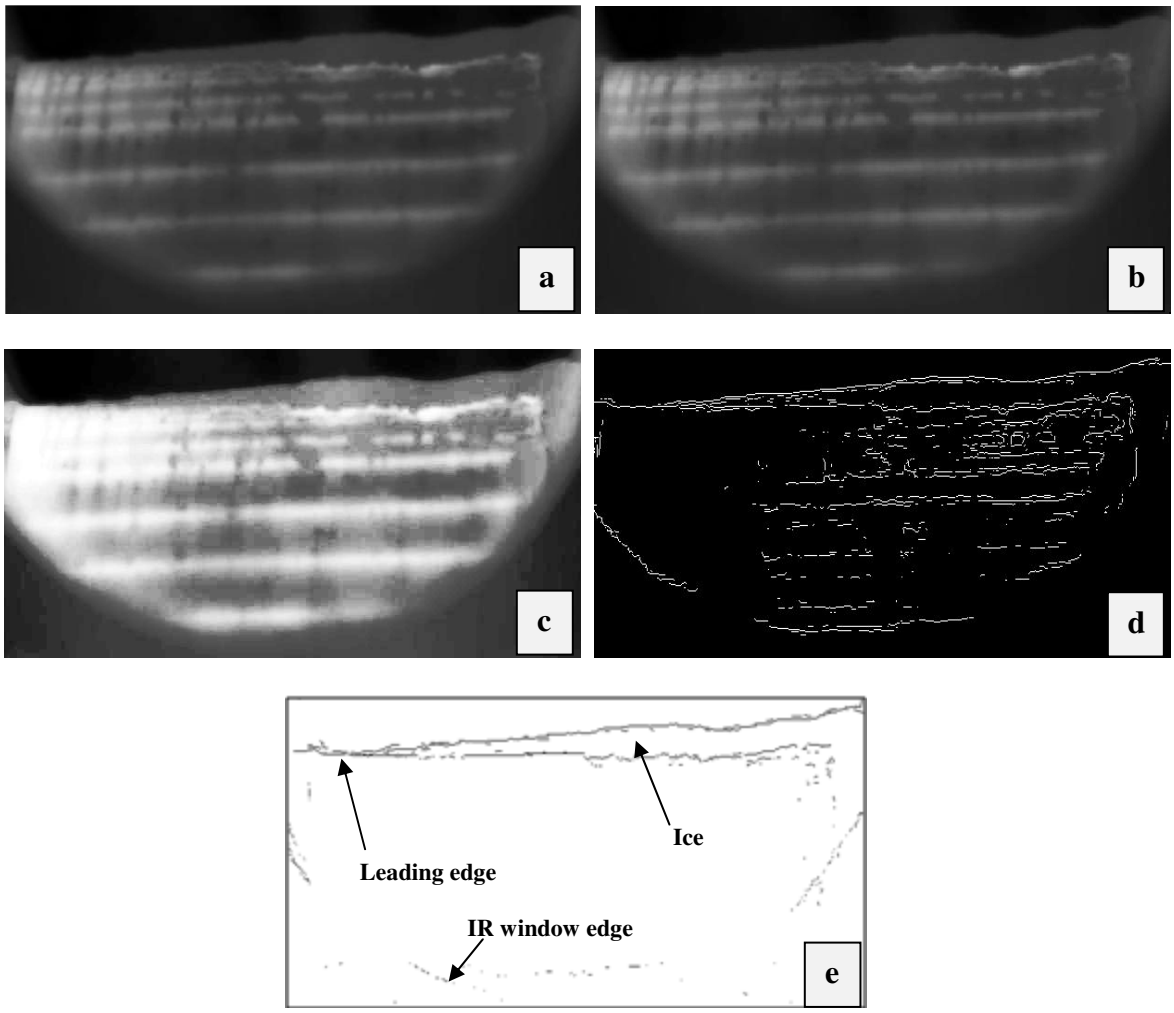

Figure 4-4- Sequential steps for image processing of IR images (top view of the airfoil) to detect ice accretion on airfoil (I): (a) grayscale image, (b) after median filter, (c) after contrast enhancement, (d) after edge detection, (e) after cleaning and inversing the image. The bright areas in images a-c show thermal elements embedded in the airfoil.

4.2.2.3 Simultaneous Monitoring of Ice Accretion and Temperature

To investigate the relation between the ice accretion and the airfoil surface temperature distribution during icing test, the "rain 10" color scale IR images, showing temperature profile, were masked with the processed IR images showing iced regions. This was done using a specially developed MATLAB code (see Figure 4-5). In this method, coordinates

of the black pixels showing iced regions were first detected in the processed IR images; then the intensity value of pixels with the corresponding coordinates in the color scale IR images were changed to 255 to show the iced region edges as "white". Figure 4-5 shows the masked "rain 10" color scale IR image with the processed IR image at 80s of the icing test. A series of masked images can be used to monitor simultaneously the ice accretion pattern and the airfoils' surface temperature evolution during icing test period.

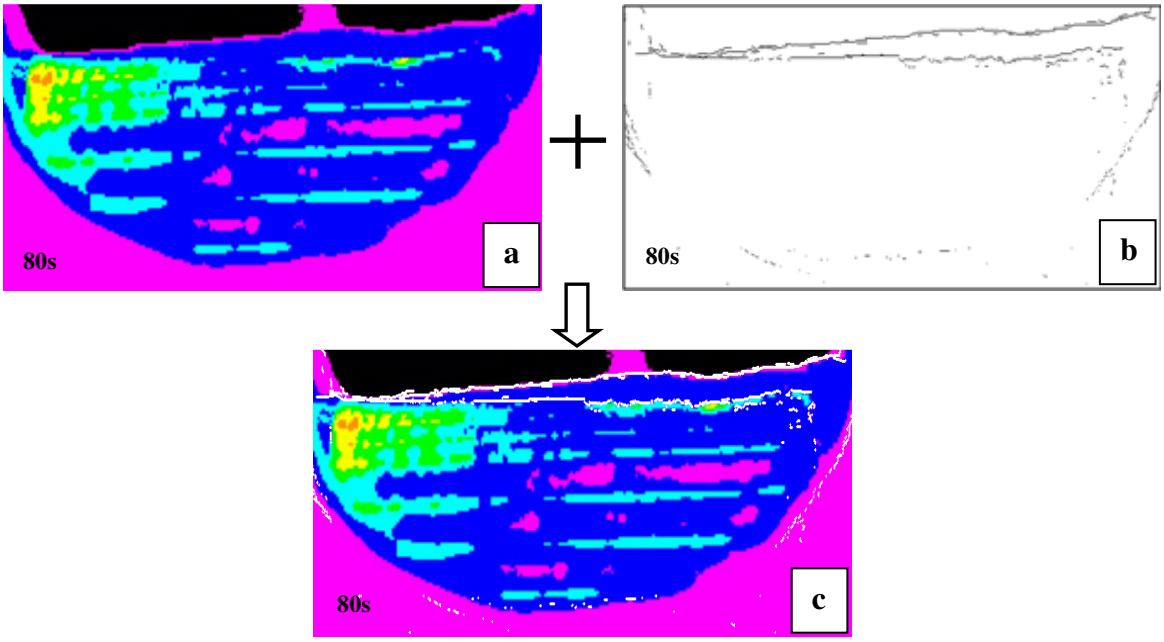

Figure 4-5- Overlaying of "rain 10" color map IR image with the processed IR image of airfoil (I) surface at 80th second of icing test period, (a) "rain 10" color map IR image, (b) processed IR image shown in (a), and top view of the airfoil, (c) overlaid image of (a) and (b), showing outline of iced areas and temperature of the airfoil surface, (color figure on line).

4.2.2.4 Ice Accumulation Rate

Grayscale IR images of airfoil (I) were also used to determine the ice accumulation rate. This was done by monitoring the rate of change of, e.g. the projected area of ice grown

outward from the airfoil's leading edge. First, the detected iced region was selected in all grayscale frames of the IR video. Then, the projected area of the accumulated ice was measured by counting the pixels representing iced region. Pixels in the region of interest were counted based on the intensity of each pixel, using a developed MATLAB code. Pixels of the ice region in the grayscale IR images had the intensity between 66 and 49. MATLAB code counted the pixels in this range of intensity. Then number of pixels representing projected ice area was multiplied by the known area of each pixel, i.e. 0.73mm × 0.73mm, in the IR images. Finally, calculated ice accumulations from grayscale IR frames were plotted as a function of icing test time for airfoil (I).

4.3 Results and Discussion

Ice was detected from IR video snapshots for airfoil (I) to monitor the ice accretion and growth pattern during icing test period (see Figure 4-6). Figure 4-6 shows the ice growth pattern on the leading edge of airfoil (I), at 20 second intervals over the 2 minute icing test period. As can be seen in Figure 4-6, ice has grown outward from the airfoil leading edge and its amount increased with the icing test time. Also, ice accretion on the leading edge area was not symmetrical, and the amount of accumulated ice on the right side of the airfoil leading edge was more than that of the left side. The asymmetric ice accumulation is explained by the non-uniform surface temperature distribution of the airfoil's surface (see below for details).

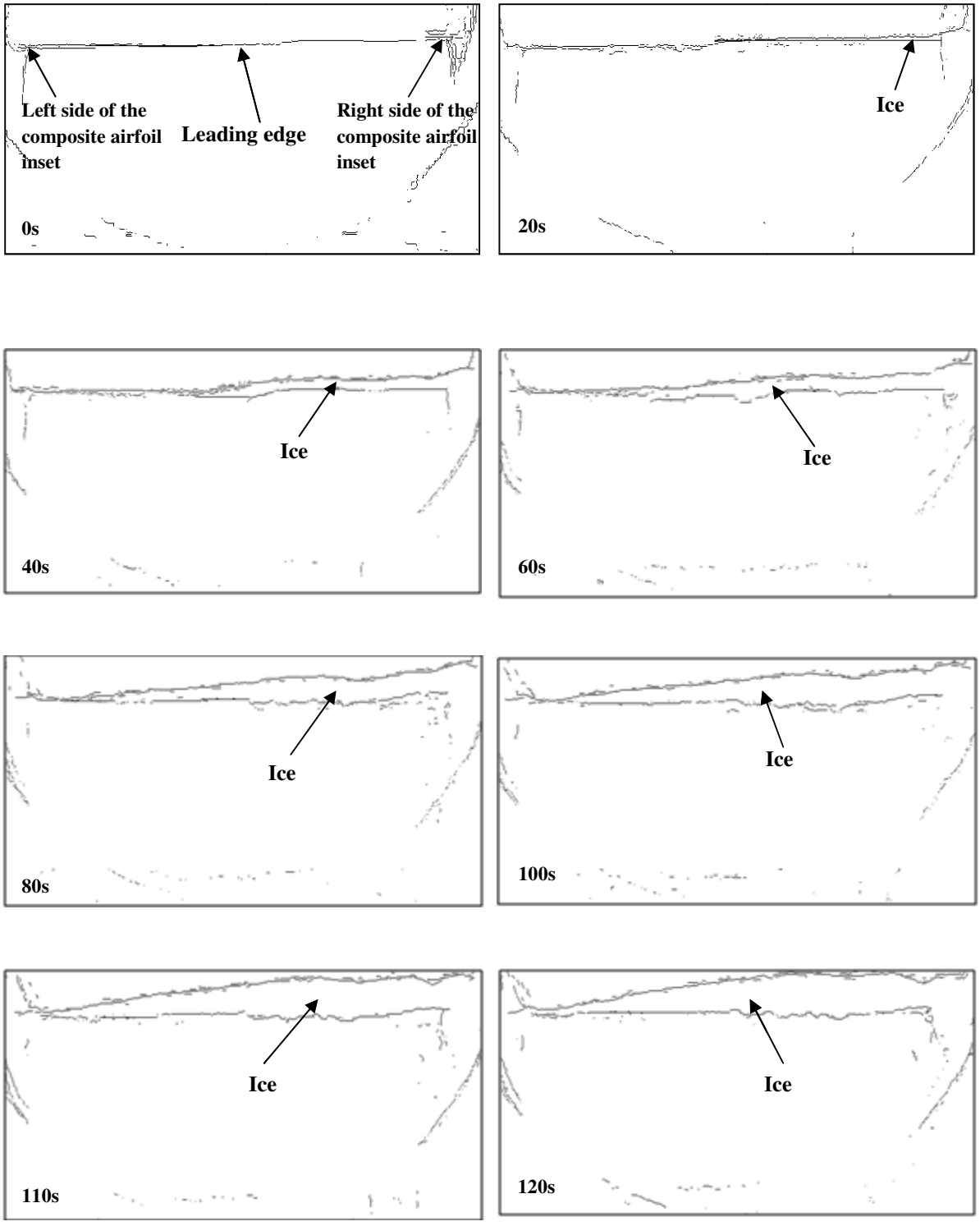

Figure 4-6- Ice accretion detected from IR video snapshots during icing process of airfoil (I), at 20 second intervals over the 2 minute icing test period.

Figure 4-7 shows the ice growth pattern at the end of icing test as compared from optical image and the processed IR image of airfoil (I). As can be seen in Figure 4-7(c), detected ice on airfoil (I) leading edge from the processed IR image is in a good agreement with the optical image of the airfoil, showing the grown ice outward from the airfoil leading edge. Some minor icing on airfoil (I) surface can be observed in the optical image (see Figure 4-7(a)), which is not identified in the processed IR image (see Figure 4-7(b)). This difference is because of intentional removal of minor icing from the processed IR images as explained earlier. Our goal at this stage was detecting major icing which affect the airfoil performance, and showing the principal of the developed methodology.

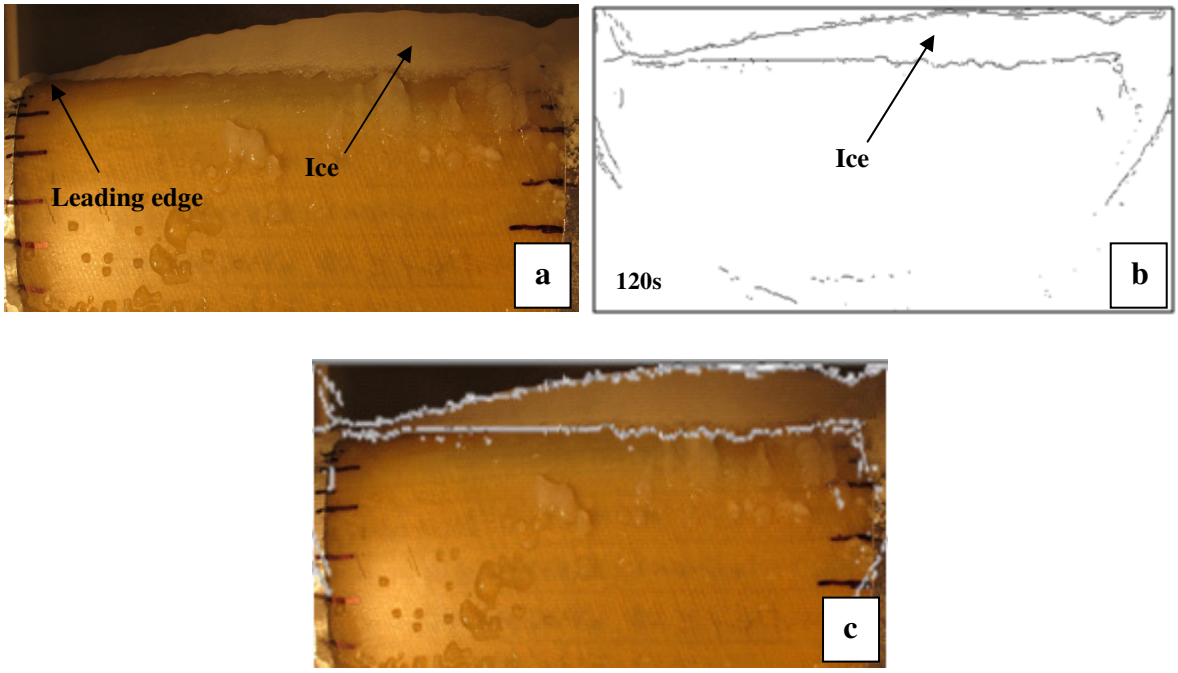

Figure 4-7- Comparison of ice detected IR image with the optical image of airfoil (I) surface at the end of icing test period, i.e. at 2min, (a) optical image of the airfoil, (b) processed IR image, (c) overlaid image of (a) and (b).

The pattern of ice formation and removal on airfoil (II) surface during icing test period is shown in Figure 4-8. As can be seen in Figure 4-8, ice growth pattern on airfoil (II) surface is different than that of airfoil (I) shown in Figure 4-6. Figure 4-8 shows that ice mostly forms on airfoil (II) leading edge area during icing test period, and then swept from the surface. Only small amount of ice remained on the middle part of leading edge area. Also, the amount of ice formed on the right side of the composite airfoil increased as icing test time progressed. Ice detected from IR images of airfoil (II) shows that ice first accreted on the aluminum fixture and then grew on to the composite airfoil insert. Type of ice accretion and growth pattern can be used in determining the required icing mitigation strategy to control the ice accumulation effectively.

The processed IR image of airfoil (II) is compared with the optical image of the airfoil at the end of icing test period, i.e. at 2 min, in Figure 4-9. Figure 4-9(a) shows ice on the middle and right side of the airfoil leading edge area which is the same as the detected ice from the processed IR image shown in Figure 4-9(b). The slight discrepancy is seen due to the thin ice on the middle part of the leading edge area. This is due to the inevitable delay in taking optical image which led to melting of the thin ice on the leading edge region test section (note that an initial visual inspection confirmed the thin ice presence). Photography needs to be performed after the icing test was stopped, and the lid including the IR window removed.

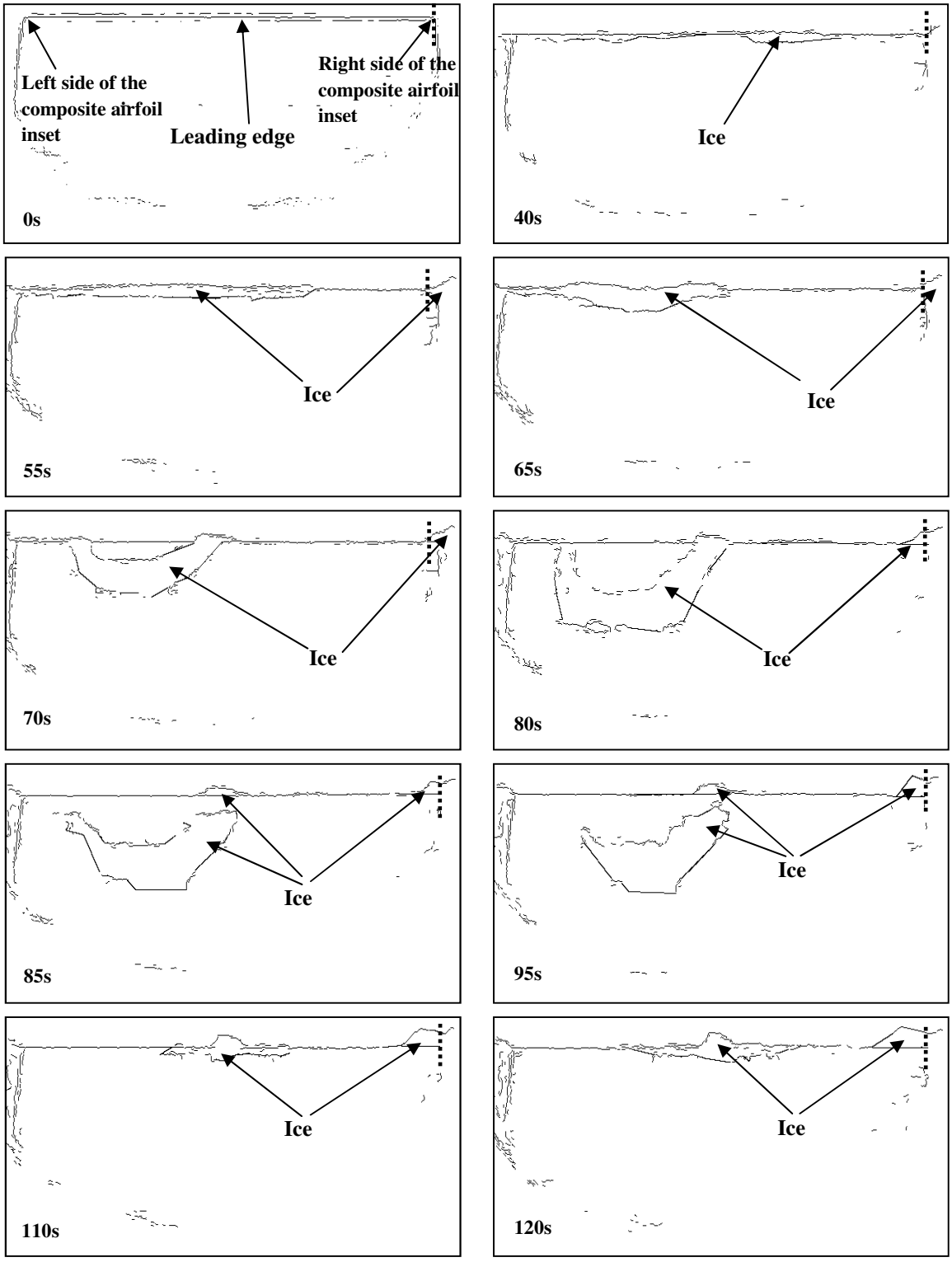

Figure 4-8- Ice detection from sequential IR video snapshots during icing process of airfoil (II), edge of the aluminum fixture is shown by dashed black line on the right side of the images.

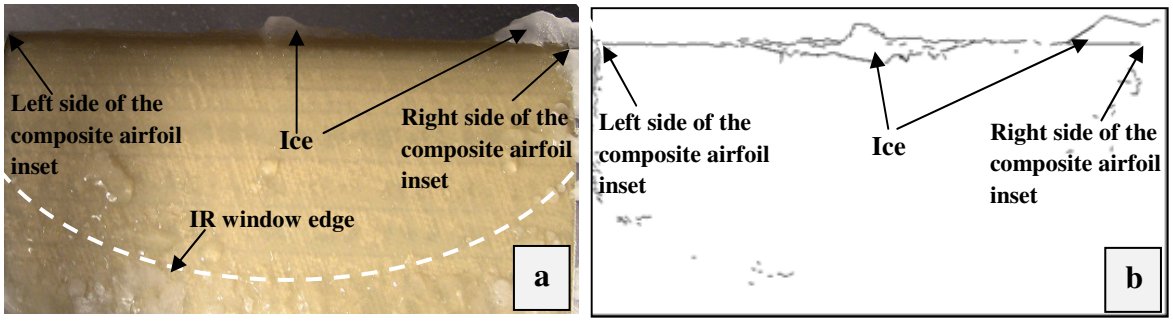

Figure 4-9- Comparison of ice detected IR image with the optical image of airfoil (II) surface at the end of icing test period, i.e. at 2min, (a) optical image of the airfoil's surface, (b) processed IR image. Note that (a) was taken at a delayed time with respect to the (b), see text.

To monitor the ice accretion and growth pattern simultaneously with the airfoil's surface temperature changes during icing test period, the "rain 10" color map IR images of airfoils (I) and (II) were masked with the ice detected IR images shown in Figure 4-6 and Figure 4-8. Figure 4-10 shows the ice growth pattern and the surface temperature evolution of the composite airfoil (I) during 2 minute icing test. As can be seen in Figure 4-10, the airfoil's surface temperature drops significantly after starting water spray as shown in the image with 20 second time stamp. Knowing the significant temperature drop is helpful in predicting the probability and onset time of ice accretion on different areas of an airfoil's surface during icing process. Ice will start to form if the airfoil's surface temperature during water spray is not above water freezing point. Also, it can be used to evaluate the performance of the icing mitigation system.

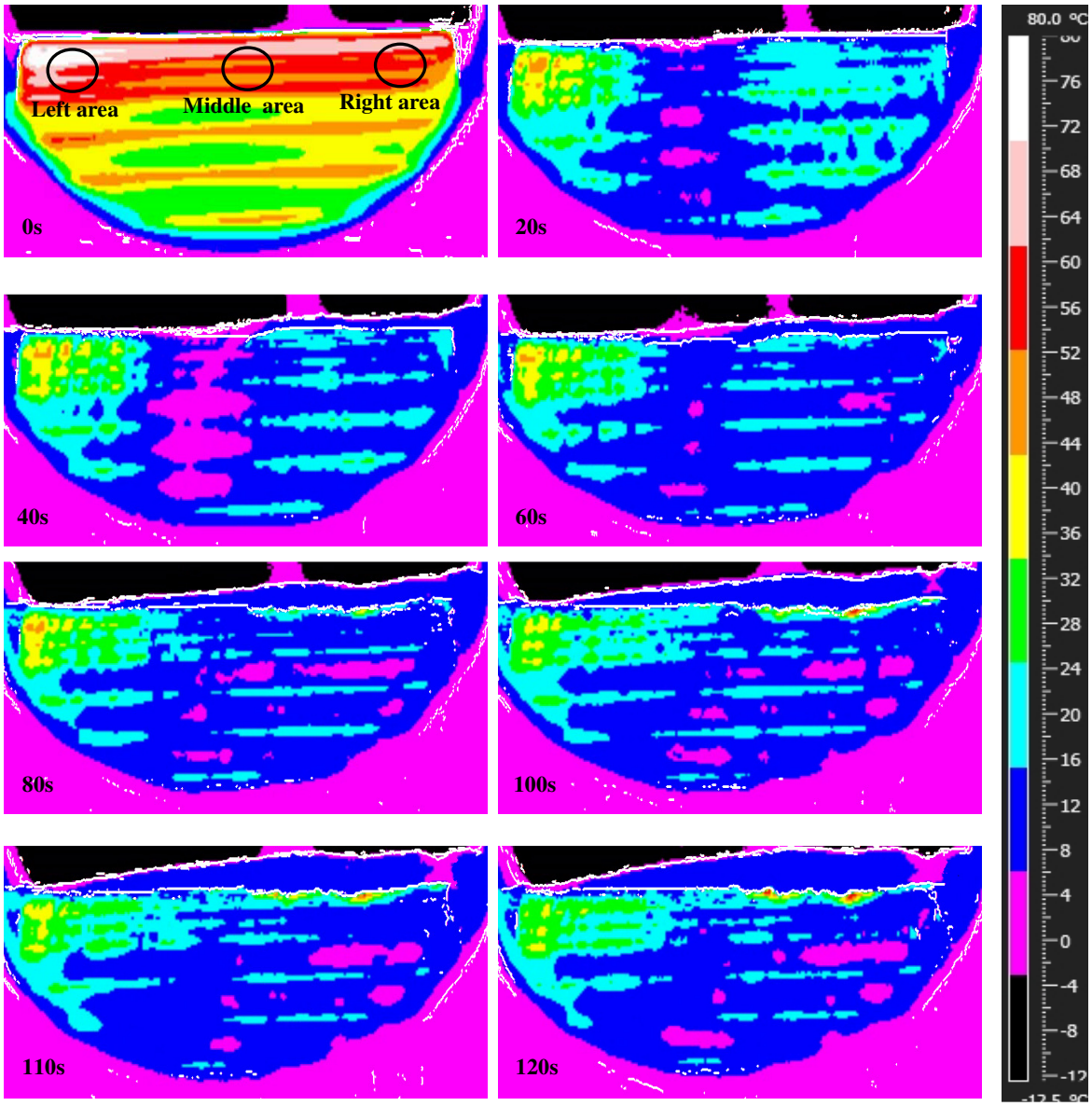

Figure 4-10- Airfoil (I) surface temperature evolution and ice growth pattern during icing process of the airfoil, at 20 second intervals over the 2 minute icing test, color bar on the right side of the images shows the temperature profile of the airfoil's surface (color figure on line). At time 0s, no water was sprayed; the spray was started at time 8s.

The IR image was calibrated for emissivity of the airfoil; as such, temperature of accreted ice cannot be read from processed IR images shown in Figure 4-10, because of different emissivity of ice than that of the airfoil's surface. But, if needed temperature of ice surface can be read from such IR images through pixel by pixel calibration of IR camera,

using the emissivity of ice for the regions covered with ice. This can be done by inputting the emissivity of ice into the IR camera software instead of the airfoil's surface emissivity and measure the temperature of iced regions in IR images. Pixel by pixel calibration was not done in this work, but in principle it is not a difficult task to accomplish.

Figure 4-11 shows the average temperature of the selected areas on the left, middle and right sections of airfoil (I) leading edge area, shown in Figure 4-10 (at time 0 second), as a function of spraying time in icing (wet) condition. In Figure 4-11, the fluctuations in temperature measurements are due to the moving ice/drop on the airfoil, having different temperature and emissivity than the airfoil (ice/drop has ~1% - ~4% lower emissivity than that of the airfoil [18]).

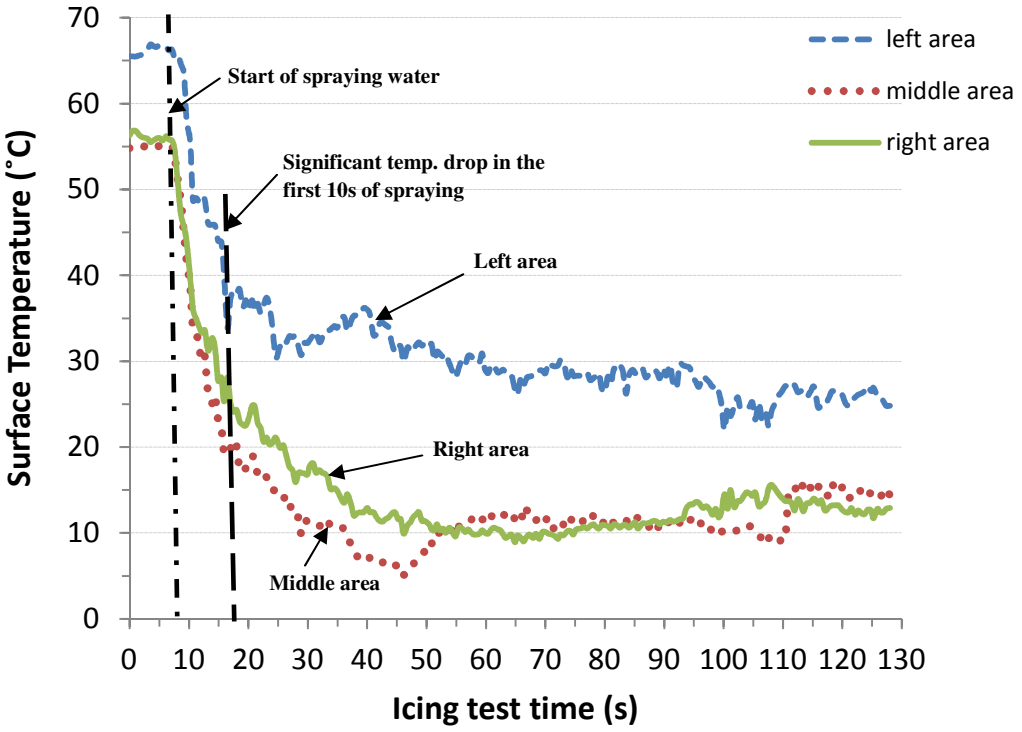

Figure 4-11- Graph of surface temperature as a function of icing test time for the selected areas (see Figure 4-10) on airfoil (I) surface in icing (wet) test, (color plot online).

Figure 4-11 can be used to show the large surface temperature drop within the first 10 seconds of spraying water (~18 seconds of icing test time), shown with the black dashed line. Figure 4-11 also shows that the initial airfoil's surface temperature on the left side is higher than that of the middle and right sections of the airfoil. It was found that the spacing between thermal elements on the left side is less than that of the middle and right sides due to the displacement of thermal elements during fabrication of airfoil [12]. This led to higher surface temperature on the left side of airfoil (I). Also, air flow swirl inside the wind tunnel can be another reason for this temperature difference. The asymmetric ice accumulation in Figure 4-10 can be explained by the non-uniform surface temperature distribution of the airfoil's surface. The left side of the airfoil with higher temperature shows less ice accretion; while the middle and right sections with lower surface temperature shows higher amount of ice accumulation. Also, the temperature drop after starting water spray is less for the left side of the airfoil than that of the middle and right sections. As can be seen a combined temperature and ice growth pattern in a visual manner can be a very useful tool to interpret anti-icing system performance or study icing phenomena.

Surface temperature changes of airfoil (II) along with the ice formation and removal pattern during icing test period is shown in Figure 4-12. As can be seen in the image with 0s time stamp in Figure 4-12, temperature profile of the region next to the leading edge area is more uniform compared to that of airfoil (I) in Figure 4-10. This can also be observed in Figure 4-13 which depicts average temperature of the selected areas on the left, middle and right sections of airfoil (II). Different temperature profiles of airfoils (I)

and (II) is the main reason of having a different ice accretion pattern on the airfoils' surfaces (see Figure 4-6 and Figure 4-8). Figure 4-13 also shows that temperature drop on the right side of airfoil (II) is larger than that of the left side, which can be due to swirl inside the wind tunnel. As can be noticed in Figure 4-13, there is a small temperature difference between the initial surface temperatures of airfoil (II) on the three selected areas. The temperature difference is small and it is in the range of temperature measurements uncertainty for these experiments, i.e. ±3˚C, [12]. It may also be due to the minor wires alignment defects during the composite airfoil fabrication process. Surface temperature profile changes of an airfoil during icing test period, such as provided in Figure 4-11 and Figure 4-13 can also be used in studying the effect of changes in the airfoil profile, due to the ice accretion and growth, on the airfoil's surface temperature distribution.

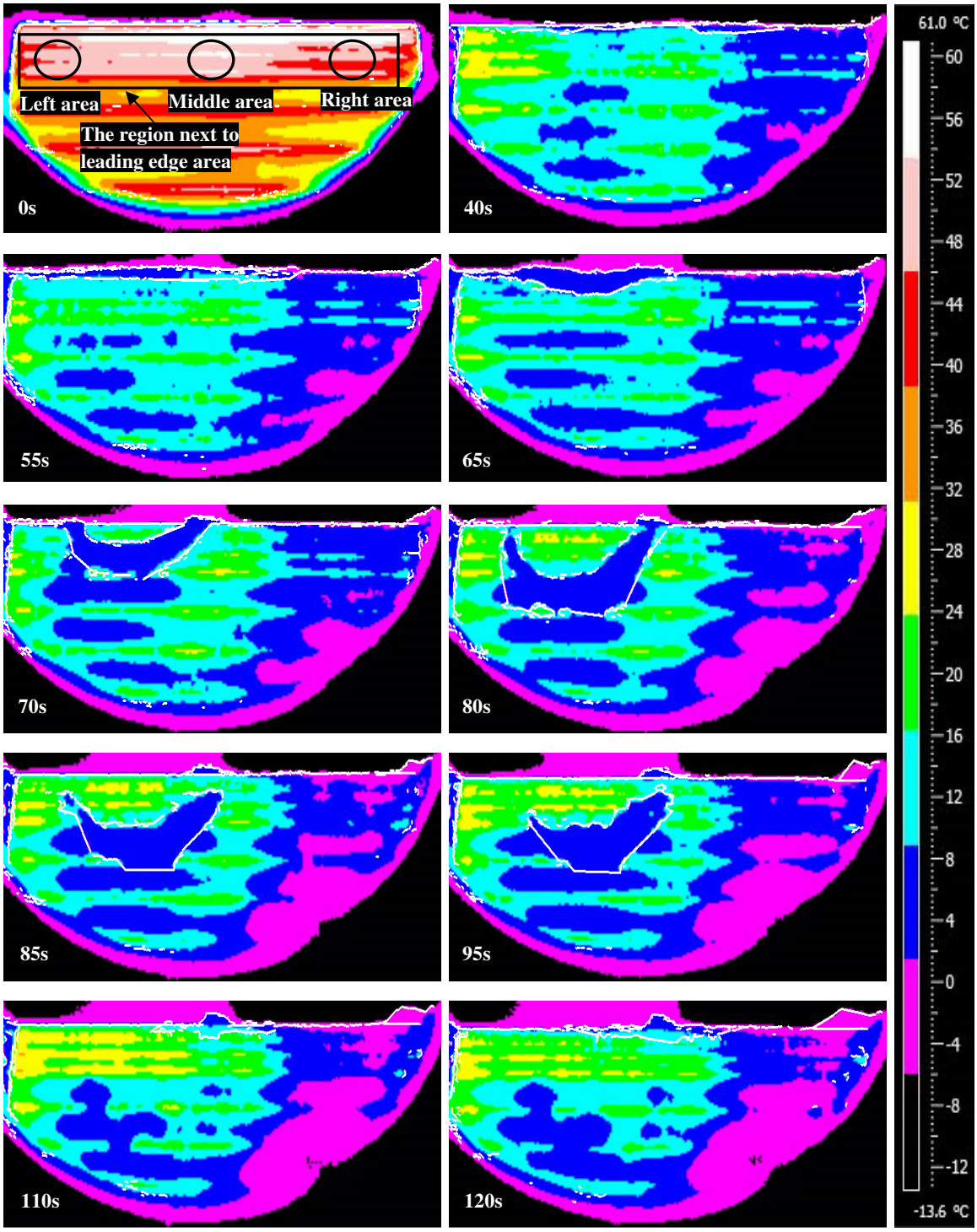

Figure 4-12- Airfoil (II) surface temperature evolution and ice growth pattern during icing process of the airfoil, taken over the 2 minute icing test, color bar on the right side of the images shows the temperature profile of the airfoil's surface (color figure on line). At time 0s, no water was sprayed; the spray was started at time 6s.

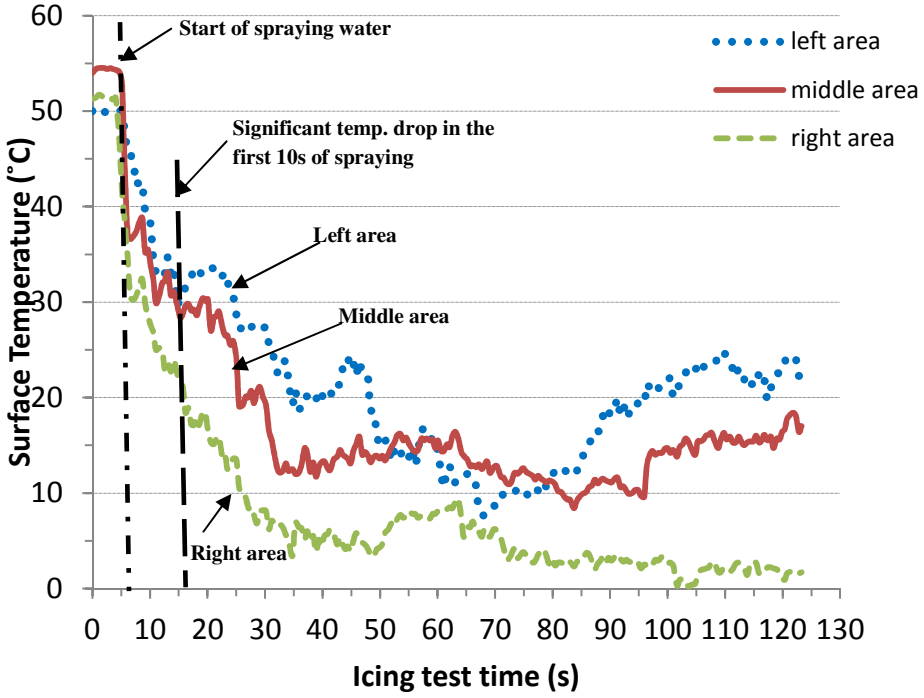

Figure 4-13- Graph of surface temperature as a function of icing test time for the selected areas (see Figure 4-12) on airfoil (II) surface in icing (wet) test, (color plot online).

The processed IR images in this study were also used in determining the projected area covered by ice on airfoil (I) leading edge and its changes with icing test time, as described in Section 4.2.2.4. This information provides an indication of the ice accumulation rate on the airfoil's surface in a given icing test condition, and for a particular icing mitigation strategy. The calculated ice area (projected) can also be used as an indication of the type of the ant-icing/de-icing system which is required to prevent ice formation or removing the accreted ice.

Figure 4-14 shows the projected area covered by ice grown outward from the airfoil's leading edge as a function of the icing test time; the ice area on the airfoil's leading edge

increases with the icing test time. The processed IR images of airfoil (I) presented in Figure 4-10 also show the same trend in ice accumulation over icing test time.

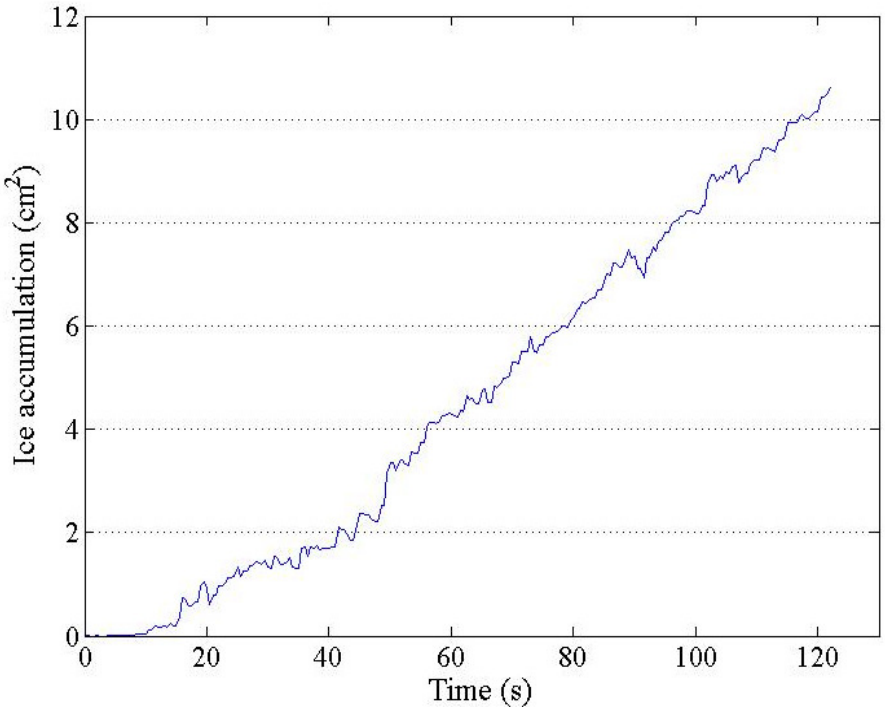

Figure 4-14- Ice accumulation rate on airfoil (I) leading edge region in the 2 minute icing test period.

4.4 Summary and Conclusions

In this study a methodology based on IR imaging was developed for simultaneous monitoring of ice accretion and thermography of a polymer composite airfoil equipped with an electro-thermal anti-icing system. Simultaneous information about temperature field and ice accretion is essential for energy efficient design of thermal anti-icing/de-icing systems. This methodology is based on processing of IR images of airfoils' surfaces during icing test period, using a specially developed MATLAB image processing

algorithm. The IR images were processed to detect and monitor ice accretion and growth pattern and investigate its relation with surface temperature changes of the airfoil during icing test.

IR images showing surface temperature profile of an airfoil can be used in studying the uniformity of surface temperature distribution and its effect on the icing behavior of airfoil. Also, temperature profile changes during icing test period provide information about the onset of icing event by showing the large surface temperature drop within the first few seconds of spraying water. Processed IR images show simultaneous information about ice accretion and temperature profile. Such a tool can be used in studying the effect of changes in the airfoil profile due to the ice accretion and growth, on the airfoil's surface temperature distribution.

Processed IR images were also used to determine the ice accumulation rate on the airfoil's surface in a given icing test condition. It was found that the ice accumulation rate on airfoil (I) shows the same trend of icing as the processed IR images of airfoil (I).

The image processing scheme has been demonstrated to work successfully, since the optical images taken at the end of the icing tests from the airfoils' surfaces agreed with the processed IR images detecting iced regions on the airfoils.

4.5 References

[1] M. Vargas, E. Reshotko, 2000, "LWC and temperature effects on ice accretion formation on swept wings at glaze ice conditions", Glenn Research Center, Case Western Reserve University, Cleveland, Ohio, NASA TM-2000-209777, Paper No. AIAA-2000-0483.

[2] F. Martini, D. Ramdenee, H. Ibrahim, A. Illinca, 2011, " A multiphase CFX based approach into ice accretion modeling on a cylinder", IEEE Electrical Power and Energy Conference, pp. 450-455.

[3] M. S. Virk, M. C. Homola, P. J. Nicklasson, 2010, "Relation between angle of attack and atmospheric ice accretion on large wind turbine blades", Wind Engineering, 34, pp. 607-614.

[4] Y. Li, K. Tagawa, F. Feng, S. Li, 2010, "Wind tunnel tests on ice accretions on the surface of a static straight blade for the vertical axis wind turbine", 2nd International Conference on Mechanical and Electrical Engineering (ICMEE 2010), pp. V1-302-V1-304.

[5] A. G. Kraj, E. L. Bibeau, 2010, "Phases of icing on wind turbine blades characterized by ice accumulation", Renewable Energy, 35, pp. 966-972.

[6] C. YiHua, Z. Gu, M. Chao, 2011, "Numerical simulation of ice accretion prediction on multiple element airfoil", Science China Technological Sciences, 54, Paper No. 9: 2296–2304.

[7] G. Fortin, J. Perron, 2009, "Wind turbine icing and de-Icing", 47th AIAA Aerospace Sciences Meeting, Orlando, Florida, Paper No. AIAA-2009-274.

[8] L. C. Martin, R. Holanda, July 24-29, 1994, “Applications of thin film thermocouples for surface temperature measurement”, Lewis Research Center, Cleveland, Ohio, NASA TM – 106714.

[9] A. J. Panas, J. Terpiłowski, P. Waślicki, 2005, “Transient temperature measurements during in-flight and wind tunnel investigations of icing phenomena”. In Flight Test-Sharing Knowledge and Experience, Meeting Proceedings RTO-MP-SCI-162, Paper 25, pp. 25-1 – 25-10.

[10] C. Antonini, M. Innocenti, T. Horn, M. Marengo, A. Amirfazli, 2011, “Understanding the effect of superhydrophobic coatings on energy reduction in anti-icing system”, Cold Reg. Sci. Technol., 67, pp. 58-67.

[11] X. Wang, E. Bibeau, G. F. Naterer, 2007, “Experimental correlation of forced convection heat transfer from a NACA airfoil”, Exp. Thermal Fluid Sci., 31, pp.1073-1082.

[12] M. Mohseni, “Development of a novel electro-thermal anti-icing system for fiber-reinforced polymer composite airfoils”, University of Alberta, M.Sc. thesis, May 2012.

[13] X. Wang, “Convective heat transfer and experimental icing aerodynamics of wind turbine blades”. University of Manitoba, PhD thesis, August 2008.

[14] G. Fortin, C. Mayer, J. Perron, Sep. 2008, “ Icing wind tunnel study of a wind turbine blade deicing system”, Sea Technol., 49, pp. 41-44.

[15] Matlab Code: Examples, http://bme.med.upatras.gr/improc/matalb_code_toc.htm, Accessed Dec. 19, 2011.

[16] D. Y. Zhi, Z. X. Dong, S. T. Sheng, L. S. Li, 2003, “Edge detection of IR ship images based on soft morphology”, Proc. of SPIE, 5203, Applications of Digital Image Processing XXVI, Bellingham, WA, pp. 581-589.

[17] Y. Yao, W. Wang, F. Chen, Y. Yu, 2011, “Nondestructive testing of transmission lines based on the image method’, IEEE Electrical Power and Energy Conference, pp. 2143-2146.

[18] FLIR Systems, Inc., “User’s manual for FLIR A320 & A325”, 2008.

5. Summary and Conclusions

The concept of a new anti-icing system in the form of embedded thermal elements for polymer composite airfoils was developed experimentally and numerically. The focus of this thesis was conceptual design aspects of the proposed anti-icing system, fabrication techniques, the energized airfoils' surface temperature profiles in cold (dry) and icing (wet) conditions, and energy consumption. Also, a methodology based on IR image analysis was developed for obtaining simultaneous information about airfoils' temperature field and ice accretion; such information is imperative for energy efficient design of an anti-icing system.

Feasibility of the concept was investigated in Chapter 2 through making polymer composite flat coupons with the embedded thermal elements and testing the coupons at specific power levels in a wind tunnel under room temperature and cold (dry) conditions. The performance of the heating system was studied by monitoring the surface temperature distribution of the composite coupons using thermocouples. The system provided fast heating of the surface when applying power; the surface temperature reached 50% of its final steady-state value in 20s. It was found that the required anti-icing temperature on the composite surface can be adjusted and controlled by the spacing of the thermal elements and the amount of applied electrical power.

Chapter 3 dealt with developing the anti-icing system for polymer composite airfoils. In this chapter, performance of the anti-icing system of the composite airfoil was characterized by developing an Infrared (IR) thermography. Thermal mapping of the

composite airfoils' surface was done in cold (dry) and icing (wet) conditions to understand the effect of surface temperature distribution and uniformity on the icing behavior of composite airfoils. It was found that 10mm spacing of wires on the leading edge region, which is the most susceptible area to ice accretion, could not provide sufficiently high surface temperature and a uniform temperature distribution to prevent icing. Experimental results implied that for the applied power level to the leading edge region, critical spacing between wires on this area was 2.5mm to have a uniform surface temperature distribution for preventing ice build-up. The applied powers to the thermal elements should be decreased from the leading edge to the trailing edge to save power. In cold dry conditions, the temperature on the leading edge region should be ~60±3˚C and the minimum surface temperature of the airfoil should be kept at ~26˚C to prevent ice accretion for the tested conditions. The total power consumption of 118.7W of this system was lower than that of 131.8W input power to a similar aluminum airfoil at the same icing condition. This verifies that the novel electro-thermal system is a promising anti-icing method for polymer composite structures with lower power consumption.

A numerical thermal analysis was also performed to determine the power threshold in the anti-icing system, and model temperature distribution on the airfoil's surface. Thermal modeling was also used to explain some of the experimental observations. The numerical thermal analysis in cold (dry) conditions was in a good agreement with the experimental results. It can be used in designing the anti-icing system, including the thermal elements' spacing and location, and required input power to the discrete wires of the heating system.

A novel image analysis methodology based on IR imaging was introduced in Chapter 4. This method was developed for simultaneous monitoring of ice accretion and thermography of the composite airfoils equipped with the proposed electro-thermal anti-icing system. The methodology is based on automatic processing of a series of IR video frames with the purpose of detecting ice pattern evolution during an icing test. The methodology developed uses a computer algorithm to not only detect and quantify the ice covered areas, but also simultaneously measure surface temperature evolution of the airfoil during an icing test. The image processing scheme has been demonstrated to work successfully, since the optical images taken at the end of icing tests from the airfoils' surfaces agreed with the processed IR images detecting the ice grown outward from the airfoils' leading edge area.

Future work

The main subject of this research was developing the concept of an electro-thermal anti-icing system for polymer composite airfoils, and its thermal characterization. Issues related to mechanical strength, and possible effects of embedding thermal elements on mechanical performance of composite airfoils were not considered. The issues needing attention are: thermal stresses induced by heating of composite, low thermal conductivity of polymer composite materials, delamination possibility of composite structure, protecting the composite material from permanent damage due to overheating (e.g. by sensor development), and optimizing power consumption.

To address these issues, future work must be done in the following fields:

- Develop a conductive polymer matrix composite.
- Generate chemical bonding between thermal elements' surface and polymer matrix composite.
- Develop special sensors for protecting composite material.
- Advanced thermal analysis of the energized polymer composite airfoil, as a layered structure, in icing (wet) conditions.
- Develop a super hydrophobic coating for the polymer composite airfoils equipped with the anti-icing system to reduce power consumption.

Appendix A

A. Manufacturing of the Polymeric Composite Airfoils with the Electro-thermal Anti-icing System

A.1 Introduction

In this study, a commercially available aerospace–grade prepreg, i.e., Necote E-765 epoxy/fiberglass prepreg from Park Electrochemical Corporation Advanced Material Technologies was used to manufacture the polymer composite laminates. Prepregs are pre-impregnated reinforcing fibers with a partially cured polymer matrix resin. The polymer matrix in the selected prepreg is an epoxy resin, and the reinforcing phase is a woven fiberglass (E-glass) fabric. Prepregs are in the form of the rolled sheets which can easily be applied to fabricate the composite structures.

The proper grade of the prepreg was selected based on the required properties of the polymer composite airfoils. Since the anti-icing system of the composite airfoils, is an electro-thermal anti-icing system, the polymer composites are subjected to relatively high temperatures; so, thermal stability of the prepreg is important. The glass transition temperature of the selected prepreg is 165˚C with the maximum operating temperature of 137˚C in dry condition.

Type of the fiber-glass as the reinforcing phase of the prepreg is also important in determining the proper prepreg. The woven fiber-glass fabric was selected to have a composite structure with equal thermal conductivity and mechanical properties in both

directions of the fibers. Specification of the selected prepreg, provided by the manufacturer, is presented in Table A-1.

Table A-1-Physical properties of the prepreg as provided by the manufacturer (Park Electrochemical Corporation).

Prepreg	**Resin Solids (%)**	**Volatile Content (% Max)**	**Tg (by DMA) (°C)**	**Gel Time at 275F(min)**	**Void content (%)**	**Maximum wet service temperature (°C)**	**Maximum Dry service Temperature (°C)**
7781 E-Glass	38	1.5	165	5	< 2%	82	137

The electro-thermal anti-icing system is consisting of thermal elements in the form of wires. Constantan wire was selected as the thermal elements due to its relatively constant resistivity over a wide temperature range (0-100˚C). Constantan wires, i.e. SPCC-005-50 and SPCC-010-50 with the diameters of 0.13mm and 0.25mm, were used from Omega Engineering Inc. to make the anti-icing system of the composite structures. Physical properties of the selected wire are presented in Table A-2.

As discussed in [1], the diameter of the constantan wire does not affect its performance as a thermal element in the anti-icing system. Since working with a wire with the larger diameter of 0.25mm is generally easier than with a wire with smaller diameter of 0.13mm, the wire with the diameter of 0.25mm was selected for manufacturing the composite airfoils with the anti-icing system.

Table A-2- Physical properties of the thermal elements as provided by the supplier (Omega Engineering Inc.).

Type	Constantan T
Composition	45% Nickel, 55% Copper
Size (mm)	0.13 0.25
Melting point (˚C)	1220
Resistivity, μΩ. cm, at 0˚C &20˚C	48.9
Temperature coefficient of resistance, Ω/Ω/˚C, (0-100˚C)	-0.1×10^{-4}
Coefficient of thermal expansion, in/in. ˚C, (20-100˚C)	14.9×10^{-6}
Thermal conductivity at 100˚C, W/m. ˚C	21.115
Specific heat at 20˚, cal/g. ˚C	0.094
Density g/cm^3	8.92
Tensile strength (Mpa)	552

A.2 Manufacturing Process

The polymer composite airfoils were fabricated by making the composite laminates first, and then shape the composite laminate into the airfoil's profile, using the designed mold. The polymer composite laminates were fabricated by dry hand lay-up of six prepreg layers with total thickness of 1.4mm.

Before starting to make the composite component, the prepreg roll was taken out of the freezer and left in room temperature to reduce the viscosity of the resin. In the dry lay-up method, the prepreg sheet is cut into the desirable size and configuration, and then the prepreg layers are pressed together by rolling them as shown in Figure A-1. Each time a

layer of the prepreg was laid, it was rolled to remove the trapped air in between the layers and press them together.

Considering the final size of the composite airfoil, six layers of the prepreg were cut into rectangular sheets with dimension of 16.5cm (L) × 19cm (W). Three layers of the prepreg were deposited first, and then the wires with the specific pattern were affixed straight on the third layer, using a specially designed jig (see Figure A-2). Figure A-2 shows the specially designed jig with fixed and straight wires on the third layer of the composite laminate. Finally, another three layers of the prepreg were laminated on top of the elements. So, the constantan wires as the thermal elements were laminated in the middle of the composite flat sheet.

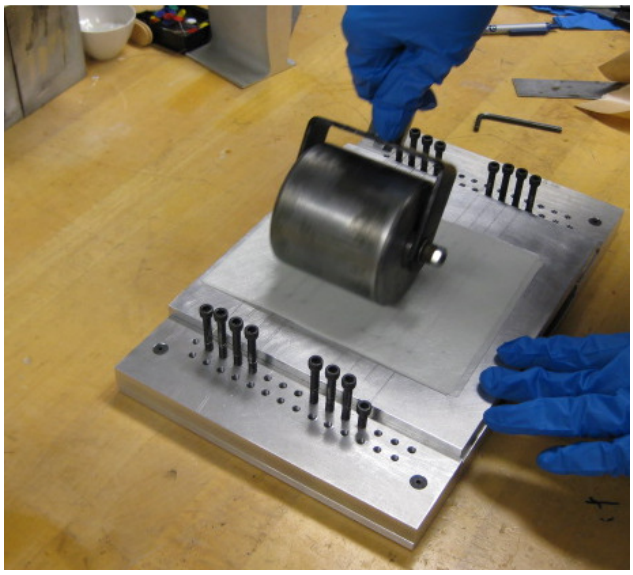

Figure A-1- Rolling the layers of the prepreg to make the polymer composite laminate.

As shown in Figure A-2, the bolts are placed at a specific distance from each other on the jig plate; and the wires can be kept straight with a specific spacing, using the bolts. The bolts have a hole to allow wires to go through and become affixed on the bolts. The wires are threaded into the thickness of the composite laminate, as shown in Figure A-3. Figure A-3 shows the schematic of the composite laminate thickness with the position of the threaded thermal element.

After fabricating the composite laminates with embedded thermal elements, the laminates were formed into the desired shape, using the appropriate mold, and then cured in an oven, using the vacuum bag molding. Vacuum bag molding was used for improving the consolidation of the fibers, and removing excess resin, air and volatile compounds from the composite laminate [2, 3].

Figure A-2- Especially designed jig to affix the wires straight inside the composite laminate for fabricating airfoil II.

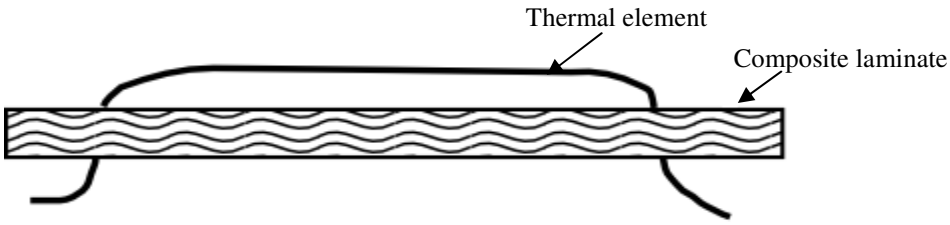

Figure A-3- Schematic of the composite laminate thickness and the threaded thermal element.

The first step in the composite materials molding is preparation of the mold surface. The surface of the mold should be well polished to assure a good surface finish of the composite part. Thermoset polymer matrixes such as epoxy resins are basically sticky. They will stick to the mold surface and removal of the composite part after curing may result in damage to the composite part or the mold. To prevent sticking the resin to the mold, release agents in the liquid form that can be spread over the mold surface, or in the form of release film should be used [3].

In this study, a water based semi-permanent release coating, i.e. MAC-860 from McLube division of McGee Industries, Inc. was used as the release agent. Two layers of the release agent were applied over the mold by spraying.

After preparing the mold surface, in the vacuum bag molding process, first, the composite laminate was placed on the mold surface and then a layer of peel ply, release film, breather and finally vacuum bag were covered the composite laminate, as shown in Figure A-4. Figure A-4 shows the lay-up assembly of different layers in the vacuum bag molding.

The peel ply layer is applied to add the release action and provide a texture for the surface of the part. The release film helps to remove the composite part from the mold. The breather layer allows volatiles such as water vapor and gases that are formed during curing process to release. As can be seen in Figure A-4, vacuum bag is the final layer which is applied on top of the whole assembly.

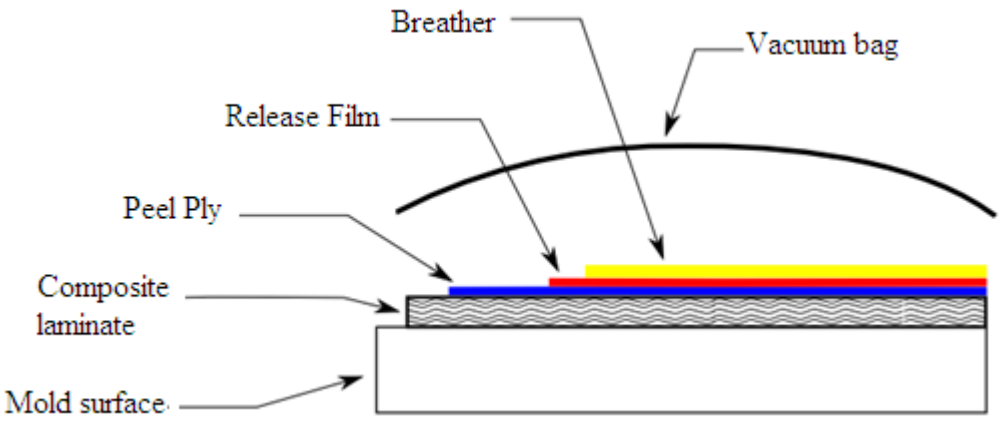

Figure A-4- The lay-up assembly of different layers in the vacuum bag molding.

The vacuum bag is used to consolidate the prepreg layers, and help to remove the volatiles that are produced during the curing process of the composite laminate. The vacuum bag also keeps the vacuum of the assembly at all times during the curing process in the oven.

In order to make the composite airfoil, the composite laminate with embedded thermal elements was shaped into the airfoil profile, using the airfoil mold shown in Figure A-5. Figure A-5 shows the two-part aluminum airfoil's mold. The mold was designed in two

parts which can be detached easily, to facilitate the removal of the composite airfoil out of the mold, after finishing the curing process.

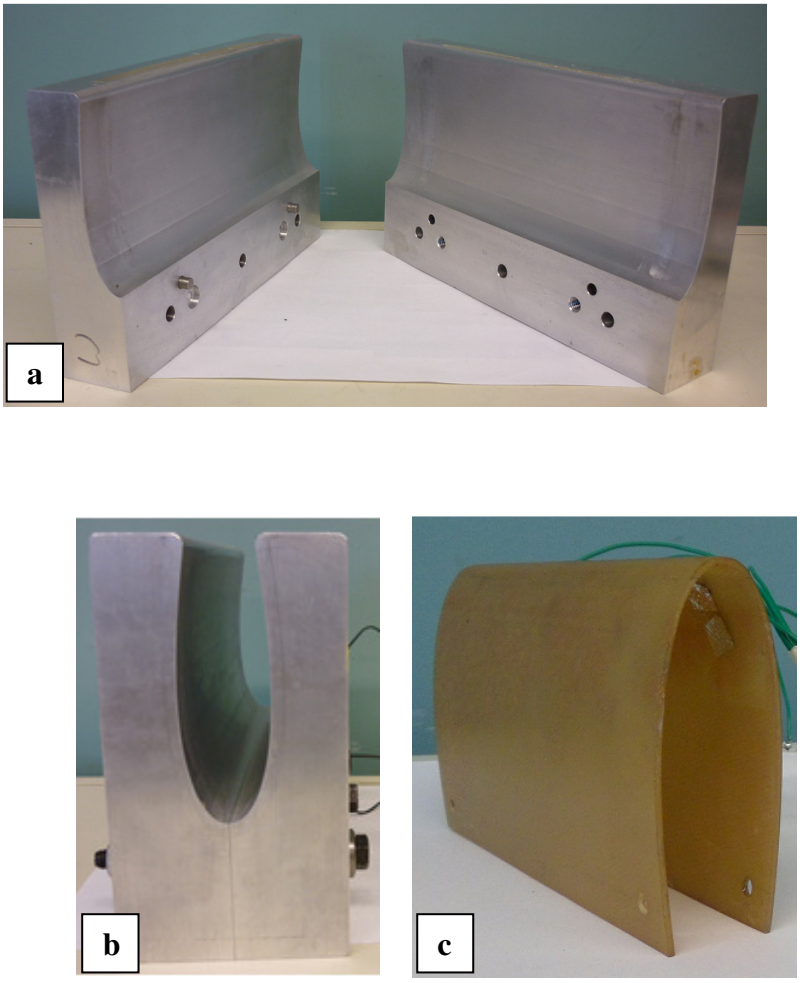

Figure A-5- Aluminum airfoil's mold, (a) two-part disassembled mold, (b) assembled mold, (c) the cured polymer composite airfoil.

Figure A-6 shows the position of the vacuum valve, and the sealant tape to apply the vacuum bag as the last layer on the composite laminate, which formed into the airfoil's shape. The lay-up assembly in the vacuum molding of the composite airfoil is the same as the composite flat sheet molding, shown in Figure A-4.

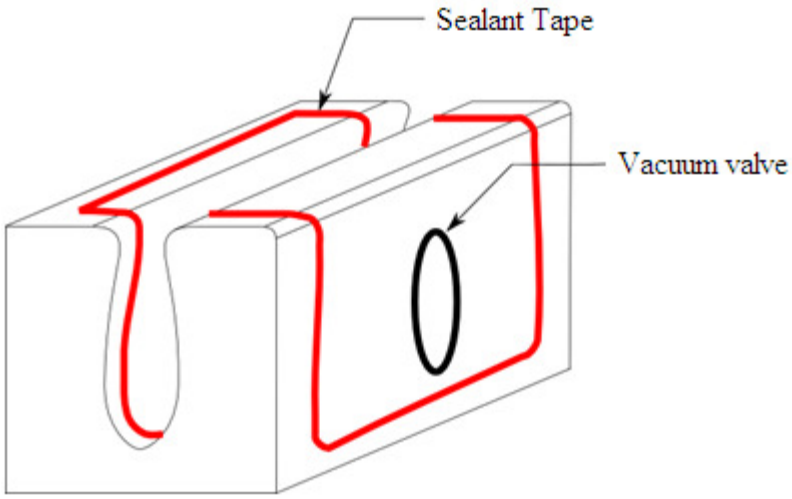

Figure A-6- Vacuum bag molding of the composite airfoil.

The whole assembly is consists of all layers on a mold surface, with vacuum connector (valve) and vacuum hose. The whole assembly was vacuumed for one hour prior to putting the whole layers into the oven, and the vacuum was kept on during the curing process and for one hour after end of the curing cycle. The amount of vacuum pressure and the curing cycle of the composite laminate were provided by the prepreg manufacturer. The composite laminate was cured in the mold for one hour at 82°C, followed by a two-hour cure at 135°C, in an oven applying a minimum vacuum pressure of 82kPa.

After curing the composite airfoil, it is cut to have the final dimension of 14.8cm (L) × 8.4cm (W) of the composite airfoil insert. The thermal elements were then connected to each other to form a serial or parallel circuit, depending on the required power scheme. The thermal elements in the anti-icing system were connected to the power supplies through conductive wires soldered to the thermal elements.

Then the prepared composite airfoil inset with embedded thermal elements was mounted in an aluminum fixture to shape the profile of the NACA 0021 airfoil with the chord length of 14.6cm. Figure A-7(a) shows the aluminum fixture used to mount the composite airfoil inset inside the wind tunnel of the experiment setup.

Figure A-7 shows the top and side views of the installed composite airfoil inset inside the transparent cavity of the wind tunnel. As can be seen in Figure A-7(b), the conductive wires are conducted to the outside of the transparent cavity through the holes on the sides of the aluminum fixture. The wires were then connected to the power supplies and/or power regulator for energizing the anti-icing system of the composite airfoil.

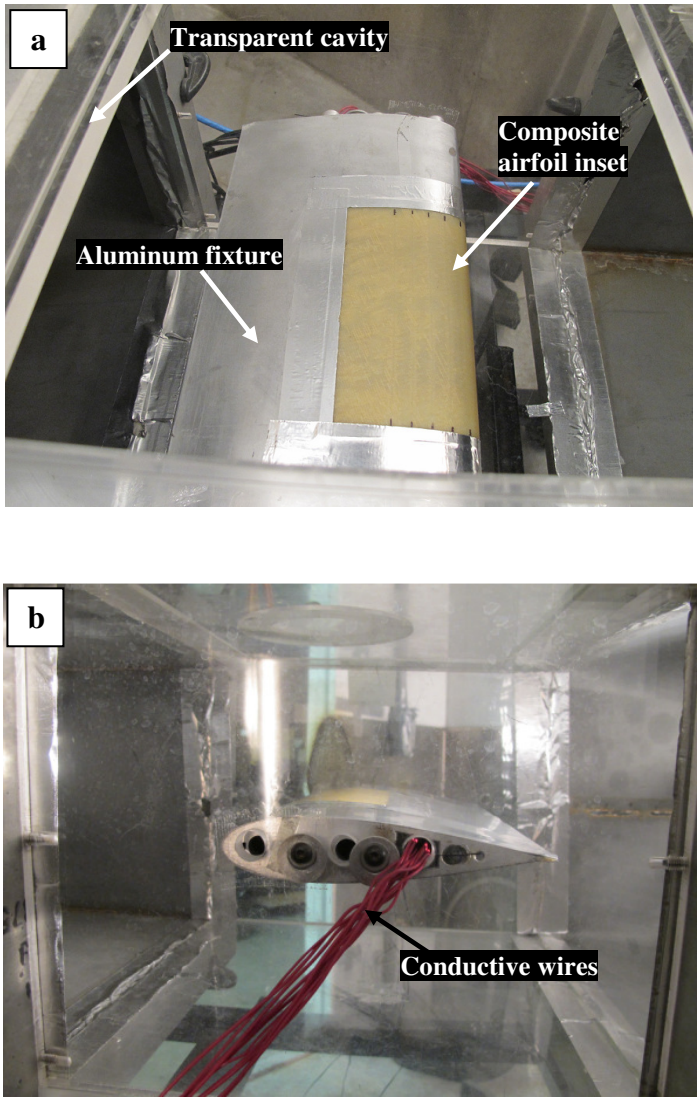

Figure A-7- The assembly of the composite airfoil inset in the wind tunnel of the experiment setup, (a) top view, (b) side view.

A.3 References

[1] M. Mohseni, P. Mertiny, A. Amirfazli, "Elctro-thermal icing mitigation system for polymeric composite airfoil", ASME 2010 International Mechanical Engineering Conference and Exposition, Nov. 12-18, 2010, Vancouver.

[2] G. Lubin, S. T. Peters, “Handbook of composites”, Chapman & Hall, 2th ed., 1998, Chap. 3.

[3] S. V. Hoa, “Principles of the Manufacturing of Composite Materials”, DEStech Publications, 2009, Chap. 4.

Appendix B

B. IR Camera Measurements of Surface Temperature of the Polymer Composite Airfoils with the Anti-icing System

B.1 Introduction

Infrared (IR) thermography or thermal imaging is recording the temperature and temperature distribution of an object through using IR radiation emitted from a surface [1]. An IR camera can detect the radiation of the electromagnetic (EM) spectrum with wavelengths approximately from 0.9μm to 14μm which is in the IR range, and convert it to visual image that shows thermal changes across an object's surface [2]. An A320 FLIR IR camera with a 10mm/45˚ lens, appropriate for our test conditions, plus FLIR Quickplot and ThermoVision ExaminIR software were used for thermal mapping and measuring surface temperature of the composite samples including the flat sheets and the airfoils.

In the IR camera's temperature measurement, the following characteristics of the experiment are important to be determined [1-4]:

1- Specification of the object surface: object's emissivity
2- Specification of the transmitting medium and surroundings: atmospheric attenuation of radiation between object and camera and background radiation reflection from the object. These specifications depend on the reflected apparent temperature, the distance

between the camera and the object, the relative humidity, and the temperature of the atmosphere.

3- Specification of the IR camera: errors caused by camera itself, such as the radiation caused by heating and cooling the camera in different operating conditions compared with the temperature in the factory condition.
4- External optics temperature and transmission. In this thesis, external optic is an IR window used in front of the camera.
5- The effect of composite airfoil curvature on the IR camera temperature measurement.

In order to have the correct temperature of the composite samples' surfaces, the camera's software needs the information of the composite material emissivity, atmosphere temperature and attenuation (reflected apparent temperature), surrounding's ambient temperature and IR window's transmittance and temperature.

B.2 Experimental setup

B.2.1 Test Conditions

Test conditions are very important in temperature measurements by an IR camera, and an accurate record of test conditions is necessary. Experiments were run in the room temperature (21˚C), cold room (dry) condition and icing (wet) conditions. Icing tests were performed in cold room condition with spraying water. All of the tests were run in a low speed wind tunnel under a maximum air flow of 27.7m/s. The tests conditions are provided in Table B-1.

Table B-1- Tests conditions.

Parameter	Laboratory conditions	Cold room conditions
Atmospheric temperature	21±1°C	-17±1°C
Relative humidity	Measured for each test	Measured for each test
Wind (water spraying) velocity	27.7m/s	27.7m/s
Reflected apparent temperature (surrounding ambient temperature)	23°C	-17°C
External window's transmission	0.7	0.7

In Table B-1, the reflected apparent temperature and the external window's transmission was measured using the method provided in the IR camera manual and IR windows producer guide, respectively [4, 5]. The provided information in Table B-1 must be imported into the IR camera software. Camera uses these data for making the following corrections [4]:

- Atmospheric transmission correction: automatic, based on inputs for distance, atmospheric temperature and relative humidity
- Reflected apparent temperature correction: automatic, based on input of reflected temperature
- External optics/windows correction: automatic, based on input of optics/window transmission and temperature

B.2.2 Actual Setup

Two sets up were designed for temperature measurement of the composite airfoils in the wind tunnel; one setup for measuring the temperature of the top surface of the airfoils, and one for measuring the surface temperature of the airfoils' leading edge. Figure B-1 and Figure B-2 represent the schematic and the actual images of the IR camera setup

inside the testing room for measuring the top surface temperature of the airfoil in cold (dry) and icing (wet) conditions.

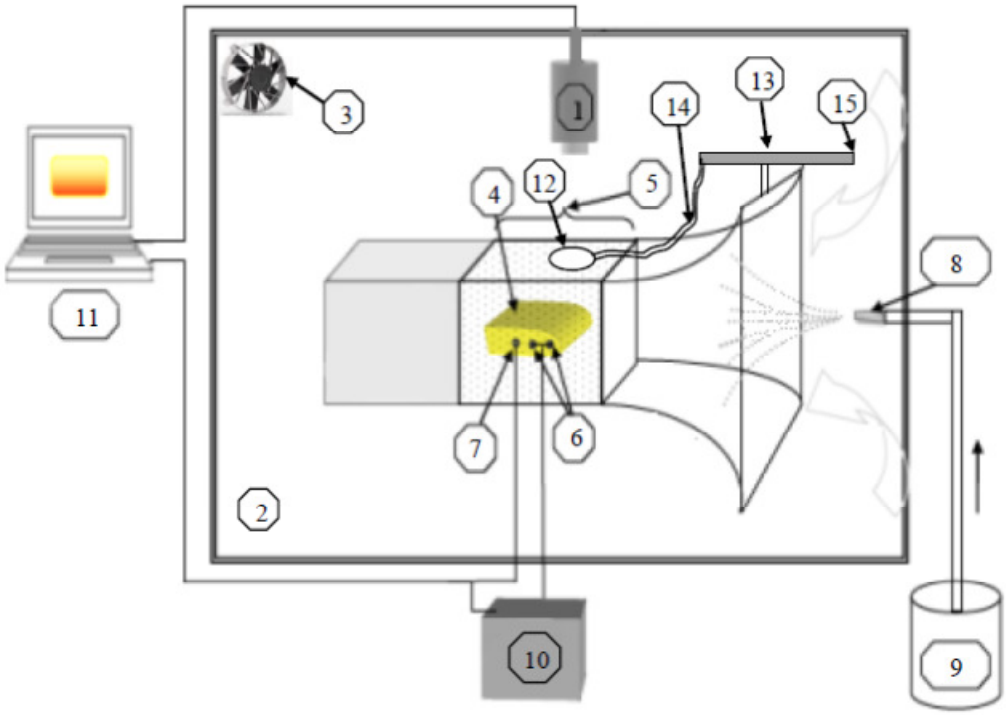

1- IR camera	5- Transparent cavity	9- water tank	13-IR window heater
2- Cold room	6- Heating system	10- Power supply	14- Heater connector tube
3- Fan	7- Thermocouples	11- PC	15- Heater inlet,
4-Polymer composite airfoil	8- Air atomizing nozzles	12- IR window	Connected to compressed air

Figure B-1- Schematic of the IR thermographic imaging for the polymer composite airfoil in the open icing wind tunnel.

As can be seen from Figure B-1 and Figure B-2, the airfoil is mounted inside an optically transparent cavity in the wind tunnel. The IR camera measures top surface temperature of the airfoil through an IR window, which is transparent to the IR radiation. As shown in Figure B-3, the IR window is mounted on the top surface of the optically transparent cavity of the wind tunnel. The IR camera is placed above the IR window at a distance of 20cm, i.e. minimum focus distance of the lens, using a tripod. It is connected to a PC for

gathering information and having thermal images and videos using the IR camera software.

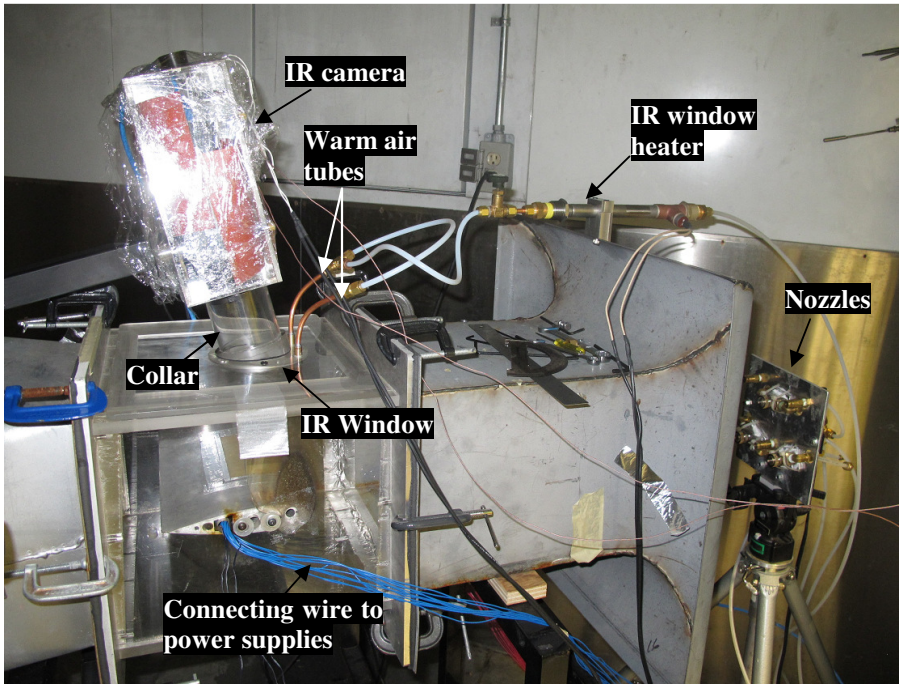

Figure B-2- Setup of the IR camera in the testing room to measure the surface temperature of the airfoil in cold (dry) and icing (wet) conditions. The camera is placed in a heated box to maintain it at the proper operating temperature and protected from any environmental issues, e.g. humidity or frost.

In icing (wet) conditions, the camera is placed in a heated box to maintain it at the proper operating temperature and protected from any environmental issues, e.g. humidity or frost. Also, the IR window should be ice free to have the thermal images of the airfoil by the IR camera. So, the IR window is protected from icing by a layer of warm air blowing over the IR window through two tubes and slots in the rim of the window; see Figure B-3. Moreover, as can be seen from Figure B-2, protecting the IR camera lens from water

condensation, and prevent ice accretion on the outer surface of the IR window in icing (wet) conditions, a collar is used to mount the IR camera above the transparent cavity.

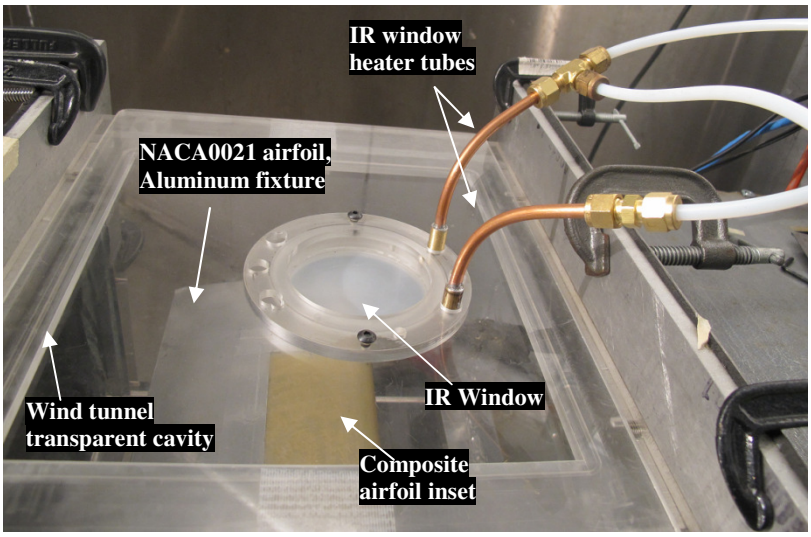

Figure B-3- Transparent cavity (test section) of the wind tunnel with the mounted IR window and the composite airfoil inset.

To measure the leading edge temperature of the airfoils, as shown in Figure B-4, the IR camera is positioned in the inlet of the wind tunnel in the same position of the spraying nozzles. The spraying setup is replaced by the IR camera, mounted on a tripod. As can be seen in Figure B-4, the IR camera is directly in the line of sight of the airfoil leading edge, and there is no need for an IR window.

Surface temperature of the composite airfoils' leading edge can only be measured in cold (dry) condition. Because, spraying water is not transparent to IR radiation, and the IR camera cannot "see" the leading edge of the airfoils during water spray operation in icing (wet) condition.

Figure B-4- Setup of the IR camera in the testing room to measure the surface temperature of the airfoil's leading edge in cold (dry) condition.

B.3 Emissivity Measurement of the Polymer Composite Material

The first step in finding the emissivity of the composite material (object) is measuring the reflected apparent temperature which is the surrounding radiation reflected in the object. According to the FLIR manual 3 [4], this parameter was measured at room temperature (21˚C), and was imported to the software of camera along with other parameters including relative humidity, atmospheric temperature and distance between lens and the object.

For emissivity measurement of the polymer composite material, a composite flat coupon, having smooth and rough surfaces, was used. Since the emissivity changes with the roughness of the surface, emissivity measurements were done on both surfaces.

As recommended by the camera manufacturer [4], a piece of a 3M Scotch Super 88 vinyl electrical tape with the known emissivity of 0.95±0.05 [6] was placed on a part of the composite coupon to provide a surface with known emissivity. Since the emissivity of the composite material should be measured at temperatures at least 20˚C higher than the room temperature, the flat coupons were heated using a hot plate. The emissivity of the coupon was measured at two temperatures of ~45˚C and ~60˚C of the composite coupon's surface. Since surface temperature of the coupon should be reasonably even [4], the coupons' surface temperature uniformity was checked on the tape surface and other parts of the coupon's surface using T-type thermocouples.

As shown in Figure B-5, the IR camera was focused on the composite coupon surface including the parts with and without the electrical tape. Figure B-5 is IR image of the composite flat coupon on a hot plate; numbers 1 and 3 mark the temperature of the tape on the composite surface and numbers 2 and 4 represent the composite coupon surface temperature without the tape.

Average surface temperature of the tape on the composite surface was measured by the IR camera by setting the tape emissivity, i.e. 0.95, into the camera software. This temperature was recorded as the composite surface temperature measured by the IR camera. Then surface temperature of the composite coupon without the tape was measured by the IR camera. Since surface temperature of all parts of the coupon should be the same, the emissivity setting in the IR camera software was changed till we read the same temperature for both parts of the coupon with and without the electrical tape. The

emissivity of the composite material was found as 0.96±0.01 for the rough surface and 0.94±0.01 for the smooth surface.

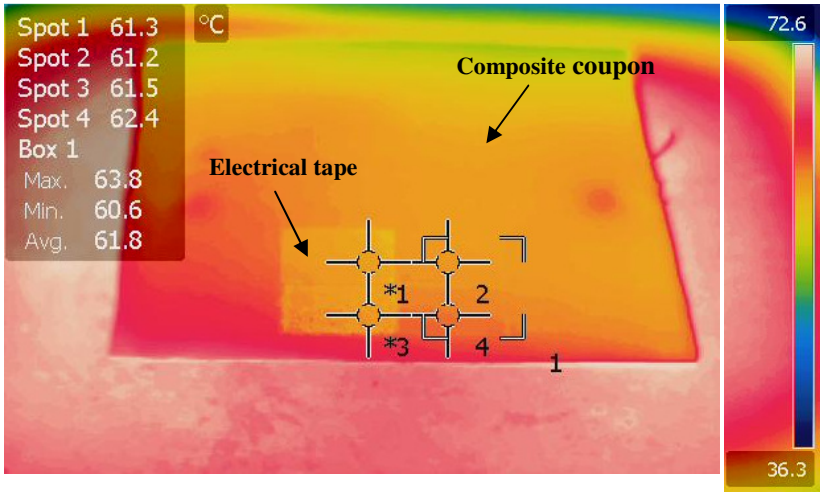

Figure B-5- Emissivity measurement of the polymer composite flat coupon.

B.4 IR Camera Calibration

B.4.1 Calibration in Room Condition

IR cameras are calibrated in the factory; besides, an IR camera automatically corrects the temperature measurement based on the imported information of the test condition and object emissivity. However, it can be calibrated in the experiment using a blackbody, which is an object with high emissivity and known temperature.

In this study, to calibrate the camera, a cup of water with controlled temperature was used. In order to measure surface temperature of water in the cup, a piece of a 3M Scotch Super 88 vinyl electrical tape with the known emissivity of 0.95 was placed on the water surface, and it was let to reach the steady-state temperature of the water. Figure B-6

shows the IR image of the cup of water with the electrical tape on the surface of water. The temperature of the water was verified using T-type thermocouples and a thermometer. As can be seen in Figure B-6 (see the legend box), the IR camera measures relatively the same temperature for different spots on the tape surface, considering that the thermal accuracy of the IR camera is 2˚C. Comparison of the measured average tape temperature by the IR camera, i.e. 45.5˚C, with the water temperature measured by the thermocouples, i.e. 45.6˚C, and the thermometer, i.e. 46.6˚C, showed that the accuracy of the IR camera measurement is in its thermal accuracy range.

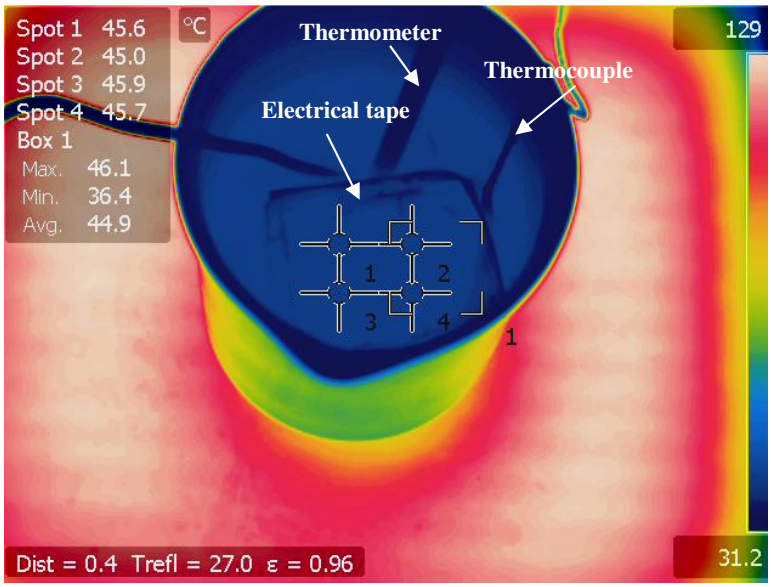

Figure B-6- IR image of the water cup with the electrical tape on the water surface.

Also, the surface temperature of the composite flat coupon was measured by the IR camera as described in Section 3; and the results were compared with the temperature measurements by the T-type thermocouples mounted on the corresponding points on the composite surface. The temperature measurements showed that the IR camera reads about 2˚C higher than the thermocouples measurements. Considering the thermocouples'

accuracy of 1˚C, this discrepancy between the IR camera measurement and the thermocouples' is in the range of thermal accuracy of the IR camera.

B.4.2 Effect of the Airfoil's Profile on the Temperature Measurement

Object emittance is an important parameter in the temperature measurements by an IR camera; and it varies with the viewing angle of the camera, i.e. the angle between the normal to the object surface and the line of sight for the camera [7]. The IR radiation intensity from a surface depends on the curvature of the surface and/or the viewing angles of the IR camera. For most of the materials, the directional influence of the emmitance is not considerable for viewing angles less than 55˚ [7]. Nevertheless, the curvature of the object and the direction of the viewing IR camera should be determined in the experiment setup for a correct temperature measurement by the IR camera.

A method was developed for measuring the temperature of the airfoil such that the curvature of airfoil does not affect the measurement by the IR camera. In this method, as shown in Figure B-7, the inside of the composite airfoil was heated by an electric strip heater. The strip heater is mounted inside the airfoil with a conductive paste to have an intimate contact with the airfoil's surface and produce a uniform temperature on the airfoil's surface. The IR camera was installed on an adjustable tripod, which can be rotated, to change the direction of the viewing camera (see Figure B-7).

Temperatures of the specific points on the airfoil's surface were measured at different viewing angles. Comparing temperatures of the corresponding points on the airfoil's

surface at different viewing angles showed that the maximum 50˚ angle between the normal to the object and the direction of the viewing camera does not affect the temperature measurement. In the other word, up to 50˚ viewing angle, the temperature of a specific point on the airfoil's surface is relatively the same with a maximum discrepancy of about ±1˚C over the 50˚ viewing angle, which is in the IR camera accuracy range.

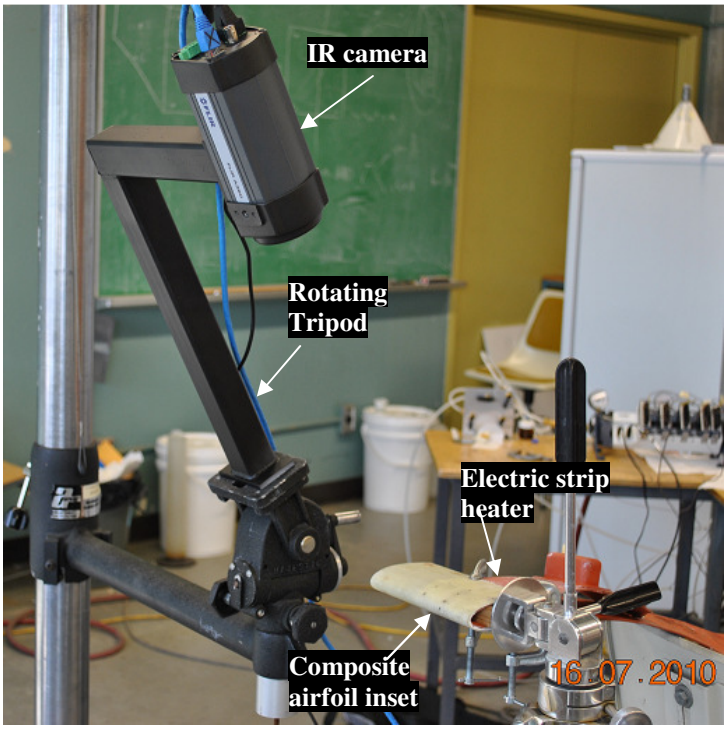

Figure B-7- Calibration of the IR camera for the airfoil's curvature.

B.4.3 Implementation of the IR camera in the Cold (dry) and Icing (wet) Condition

In this study, the experiments were conducted at -17±1˚C which is less than the minimum operating temperature of the IR camera. So, the IR camera was placed inside a heated box, as can be seen from Figure B-8 and Figure B-9. This was to protect the camera from the cold condition and water vapor condensation. The temperature of the heated box was

monitored by two T-type thermocouples placed in the top and bottom sections of the box, and connected to the data acquisition system. The average temperature of the box was kept at about 20˚C by controlling the applied power to the electric strip heaters placed on the walls of the box. To protect the IR camera lens from water vapor condensation, a collar was used to mount the IR camera above the IR polymer window shown in Figure B-3 and Figure B-8.

B.4.3.1 IR Camera Viewing Angle

To investigate the best viewing angle of the IR camera to measure the airfoil's surface temperature correctly in the cold and icing conditions, different IR camera sets up were tested. In these experiments, the surface temperature of the unenergized composite airfoil in the wind tunnel was measured by the IR camera at different testing room temperatures.

In the first set of tests, the IR camera was positioned perpendicular to the airfoil's surface and the IR window, as shown in Figure B-8. In the second tests setup, as shown in Figure B-9, the camera was tilted (backwards) by a 15º with respect to normal. When the IR camera is tilted, it can view only a part of the composite airfoil inset. So, to have a complete IR image of the composite airfoil inset, the IR window was positioned at the "upstream" and the "downstream" locations as shown in Figure B-9(a) and B-9(b), respectively. In the upstream location of the window, the IR camera can view the top surface of the airfoil which is beyond the leading edge region; and in the downstream position, the IR camera views the top surface of the airfoil including the trailing edge region.

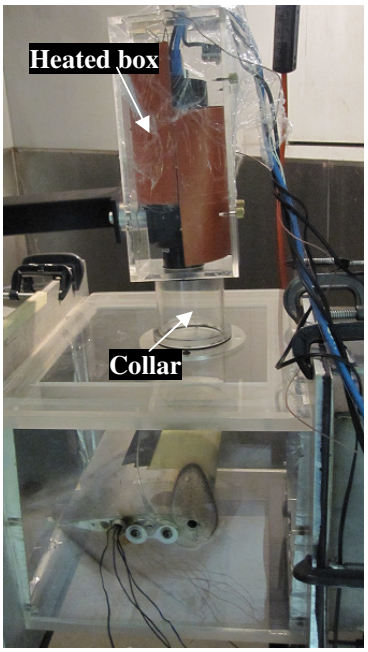

Figure B-8- IR camera setup in the testing room, perpendicular to the airfoil's surface and the IR window.

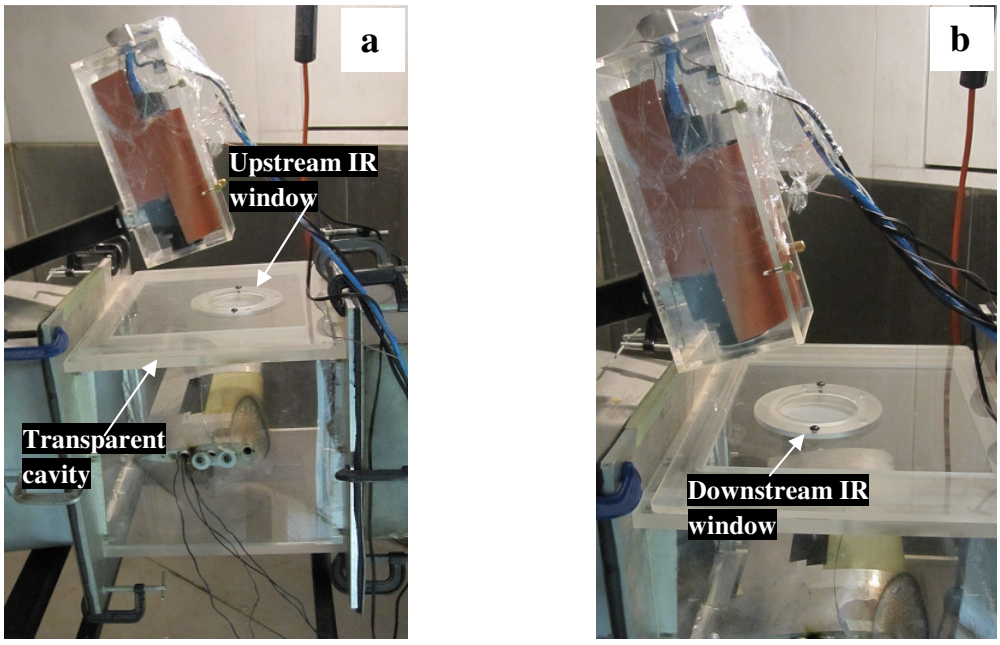

Figure B-9- IR camera setup in the chamber, viewing the airfoil at the angle of 15˚, (a) "upstream", (b) "downstream" positions.

The chamber temperature was changed from 24˚C to -17˚C, and all of the experiments were conducted at steady-state room temperatures. Since the airfoil was unenergized, surface temperature of the airfoil at thermal equilibrium was the same as the test chamber temperature.

Steady-state surface temperature of the airfoil at the test chamber temperature was measured by the thermocouple, mounted on the top surface of the airfoil, and the IR camera to compare the IR camera and the thermocouple measurements. Three tests were done for every chamber temperature (see Table B-2). In Table B-2, the measured surface temperature of the airfoil by the thermocouple and the IR camera at the perpendicular and the 15˚ viewing angle positions, at different test chamber temperatures is compared.

Table B-2- IR camera and Polymer window calibration data at different test chamber temperatures; three tests were done for every chamber temperature, and the measured temperatures were the same in each set of the tests.

Test chamber temperature (ºC)	**Airfoil's surface temperature-thermocouple (ºC)**	**Airfoil's surface temperature-IR camera at the perpendicular position (ºC)**	**ΔT (˚C) (normal to the airfoil and the window)**	**ΔT (˚C) (at a 15˚ viewing angle to the normal position)**
24	24	27	3	3
20	20	23	3	
15	15	19	4	
10	10	14.8	4.8	
5	5	10.5	5.5	
0	0	5.5	5.5	
-5	-5	1.5	6.5	
-10	-10	-3	7	
-15	-15.5	-8.5	7	
-17	-17	-10	7	

As can be seen in Table B-2, when the camera position is normal to the airfoil and the IR window, the difference between the reading from thermocouple and the IR camera increases by decreasing the test chamber temperature. The measured surface temperature by the IR camera is always higher than the temperature of the airfoil. But, at different test chamber temperatures above 15˚C, the IR camera measurements are 3ºC higher than the airfoil's temperature and it is constant in this range of test chamber temperature. Table B-2 also shows that when the camera is tilted at an angle of 15˚ to the normal, the difference between the temperature measurements of the airfoil surface by the thermocouples and the IR camera is 3˚C at different test chamber temperatures. This difference between the results in the last two columns of Table B-2 will be discussed next.

To investigate the effect of the IR camera's viewing angle on the temperature measurement, the IR images of the airfoil's surface were compared at the normal and tilted position of the IR camera. Figure B-10 shows the IR image of the unenergized airfoil's surface at -17˚C test chamber temperature; the IR camera is mounted normal to the airfoil' surface and the polymer widow.

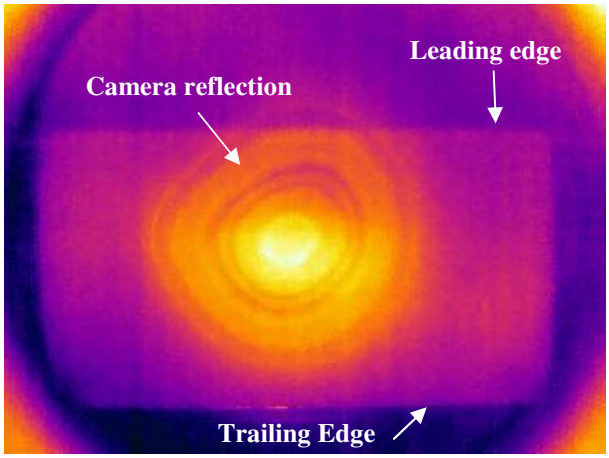

Figure B-10- IR image of the unenergized airfoil at -17ºC in the normal position of the IR camera to the airfoil's surface and the polymer window.

As can be seen in Figure B-10, the IR camera can view its own reflection from the window. The round circles in this image have the same shape of the camera head and its lens. Since the camera is hot compared to the testing room temperature, and the IR polymer window has a high reflectivity of about 21% [5], the hot camera is visible in the IR images and it disturbs the measurements. As can be seen from Table B-2, by decreasing the testing room temperature, the temperature difference between the hot camera and the testing room increases and the effect of the IR camera reflection from the IR window becomes more predominant. This leads to higher errors in temperature measurements. Lens of the IR camera is transparent to the IR radiation and lets out IR range waves (radiation) from inside of the hot camera, which then being reflected from the IR window. So, the camera somewhat superimposes its own temperature on the measurements of the airfoil's surface temperature.

In order to verify that the errors in temperature measurements in cold (dry) conditions are due to the camera reflection from the window, another IR window with lower reflectivity was used in the experimental setup. Calcium fluoride IR window (CaF_2) which has lower reflection of 5% [5] was used in the cold (dry) condition at -17˚C for surface temperature measurement of the unenergized airfoil. The IR image of the airfoil using CaF_2 window is shown in Figure B-11.

The reflection image of the IR camera from the window in Figure B-11 is clearer than in Figure B-10. Since the IR polymer window is flexible, the reflection image of the camera on the polymer window was distorted. But, CaF_2 is a crystal window, so the shape of the camera head and its lens is clear in the reflection image of the camera. The observed image of the camera on the window verifies that there is a reflection of the hot camera from the IR window.

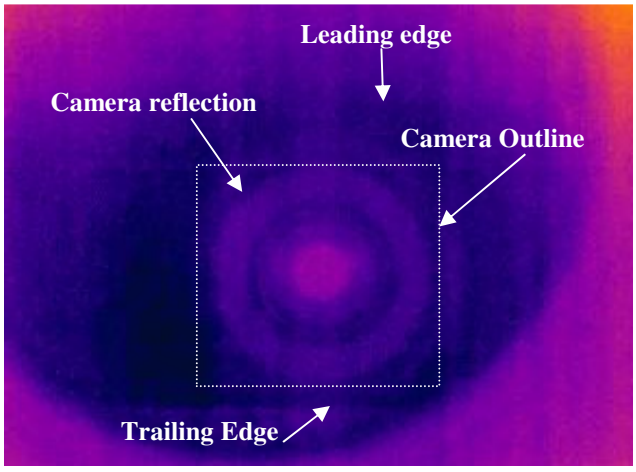

Figure B-11- IR image of the unenergized airfoil at -17ºC in the normal position of the IR camera to the airfoil's surface and the CaF_2 window; the dotted line is added for graphical clarity.

One of the best ways to overcome the problem of the IR camera reflection from the window is to avoid looking straight into the IR window. The maximum recommended tilting angle of the camera is 30˚ to the normal position [5]. In the experimental setup in this study, the camera was tilted by an angle of 15º to the perpendicular position, as shown in Figure B-9.

The IR image of the airfoil with the tilted camera with the viewing angle of 15˚ is shown in Figure B-12. Figure B-12 shows the IR image of the unenergized airfoil at -17ºC, with the upstream position of the window. As can be seen in Figure B-12, the image of the camera reflection was transferred to the outside of the IR window region.

The calibration data in Table B-2 shows that in the tilted position, the IR camera reads the temperature 3˚C higher than the temperature of the airfoil at different test chamber temperatures. In the tilted position of the camera, the errors of the temperature measurements are the same at different testing temperatures, which implies that the effect of camera reflection on temperature measurements has been removed by tilting the camera to an angle of 15˚ to the normal position. The data in Table B-2 show that in the cold (dry) condition tests, the temperature measurements by the IR camera should be reduced by 3˚C to have a correct surface temperature of the composite airfoil.

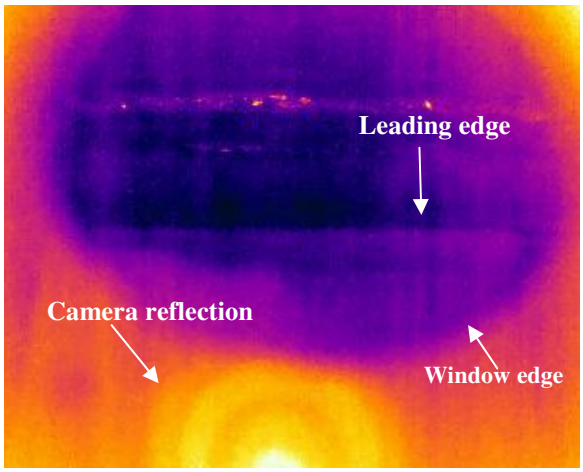

Figure B-12- IR image of the unenergized airfoil at -17ºC, with tilted camera at an angle of 15˚, and the upstream position of the window.

The accuracy of the tilted IR camera measurements, at two window positions on the upstream and downstream of the wind tunnel transparent cavity, was also investigated by testing the energized airfoil at -17˚C in cold (dry) condition. The anti-icing system of the airfoil, i.e. airfoil I (see paper "A Novel Electro-thermal Anti-icing System for Fiber-reinforced Polymer Composite Airfoils"), was symmetric, consists of 5 thermal elements on top side, 5 on bottom side, and 1 on leading edge of the airfoil (wire 1) with 10mm spacing. Surface temperature of the energized airfoil was measured at two power densities of 47.2kW/m^2 and 56.6kW/m^2. Power density is defined as the amount of power applied to a unit area of the thermal element's surface; it considers the length and diameter of the thermal element.

The IR images of the energized airfoil at 56.6kW/m^2, at two positions of the window setup are shown in Figure B-13 and Figure B-14. In both upstream and downstream positions of the window, the IR camera cannot measure the surface temperature of the

leading edge region of the airfoil. As can be seen in Figure B-13, in the upstream position, the camera can only measure surface temperature of top side of the airfoil up to the fifth thermal element (the last one on the top surface).

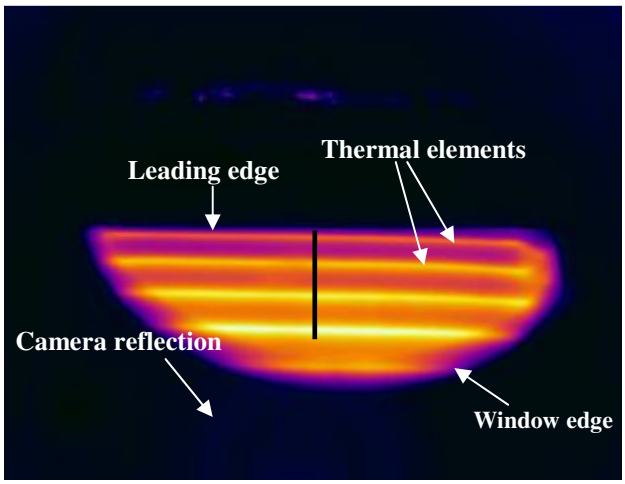

Figure B-13- IR image of the energized airfoil at 56.6kW/m^2 at -17ºC, tilted camera at an angle of 15˚ at the upstream position of the window. The local temperature measurements are shown with the vertical black line.

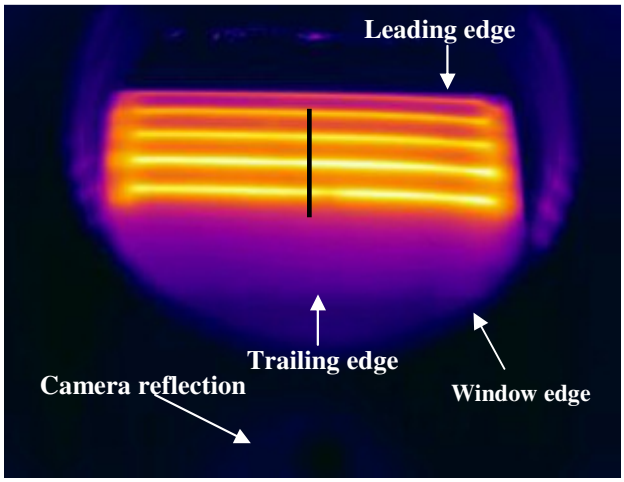

Figure B-14- IR image of the energized airfoil at 56.6kW/m^2 at -17ºC, tilted camera at an angle of 15˚ at the downstream position of the window. The local temperature measurements are shown with the vertical black line.

To measure surface temperature of the airfoil beyond the fourth thermal element, the window was positioned at the downstream position as shown in Figure B-9(b). Figure B-14 shows the IR image of the energized airfoil at the downstream position. As can be seen from Figure B-13 and Figure B-14, the camera reflection from the window is moved to the outside of the window region, and it does not disturb the temperature measurement of the airfoil's surface. In the downstream position, the camera cannot view clearly the first thermal element, but it can measure the airfoil's top surface temperature beyond the first thermal element to the end of the composite airfoil inset.

Surface temperature of the airfoil from the leading edge to the trailing edge was measured by the IR camera at two positions of the up and down stream, along the vertical black lines shown on the IR images in Figure B-13 and Figure B-14. The vertical lines on both IR images show the locations of corresponding surface temperature measurement of the airfoil.

Figure B-15 represents the surface temperature of the airfoil, measured from the IR images in Figure B-13 and Figure B-14. In Figure B-15, the peaks show temperature of top surface of the airfoil on the thermal elements and the valleys are surface temperatures on the thermal elements' midpoints.

In Figure B-15, the airfoil's surface temperature up to wire 3, was measured from the IR image at the upstream position; and the temperatures beyond wire 5 up to the end of the composite airfoil inset was measured from the IR image at the downstream position.

Surface temperatures from wire 3 till wire 5 region, i.e. between the dashed lines, were measured from both of the IR images in Figure B-13 and Figure B-14.

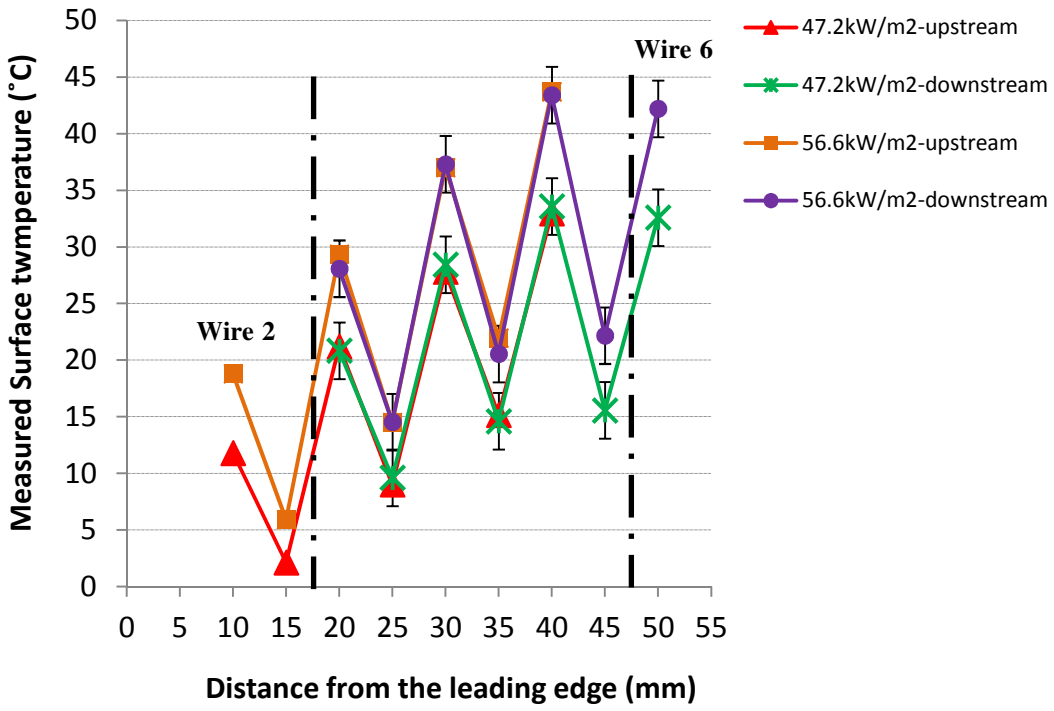

Figure B-15- Surface temperature of the airfoil at different power levels; measured from the IR images taken at the upstream and downstream positions of the IR window, between the dashed lines were measured from both positions of the IR window. Lines are to guide the eye.

Surface temperature of the airfoil from wire 3 till wire 5, i.e. the region that can be seen by the IR camera at both upstream and downstream positions, is the same in the experiments at different power levels. This implies that the temperature data measured from both upstream and downstream positions of the window is accurate and reliable.

B.4.3.2 Spatial Resolution of the IR Camera in the Experimental Setup

The spatial resolution of the IR camera in the experimental setup was obtained by the ratio of FOV (field of view) to the detector resolution of the camera. The detector of the IR camera has a pixel resolution of 320×240 (H×V). The FOV in horizontal (HFOV) and vertical (VFOV) directions, was obtained from the specification of the lens and the distance of the camera from the target (the airfoil) at the perpendicular position with respect to the target. Since the camera is tilted at an angle of 15˚ to the normal of the airfoil's surface, the HFOV normally does not change, while the VFOV should be multiplied by 1.5 to consider the effect of the camera's tilting angle [5]. According to [5], varying viewing angle to 30˚ from perpendicular increases the FOV by a factor of 3.

As a result, the spatial resolution of the IR camera in the experimental setup should be 0.49mm/pixel in the horizontal direction, and 0.73mm/pixel in the vertical direction. But, we realized that the spatial resolution in the horizontal and vertical directions is the same as 0.73mm/pixel due to the IR camera software adjustments.

B.4.3.3 Airfoil's Curvature

As described in Section 4.2, curvature of the airfoil's profile affects the surface temperature measurements by the IR camera. The airfoil's profile, drawn using Solid Works software, was used to determine the region of the airfoil's surface, including the leading edge and the top surface that can be measured by the IR camera correctly in our experimental setup.

Figure B-16 shows the airfoil's profile and the region of the airfoil's surface, i.e. top surface and the leading edge area, which is reliable to be measured by the IR camera. In Figure B-16(a), surface temperature of the region between the dashed line and the leading edge region of the airfoil cannot be measured by the IR camera. When the IR camera is positioned at an angle 15˚ to the normal of the airfoil's surface, it cannot measure the correct temperature at locations up to 3.42% of the airfoil's chord length.

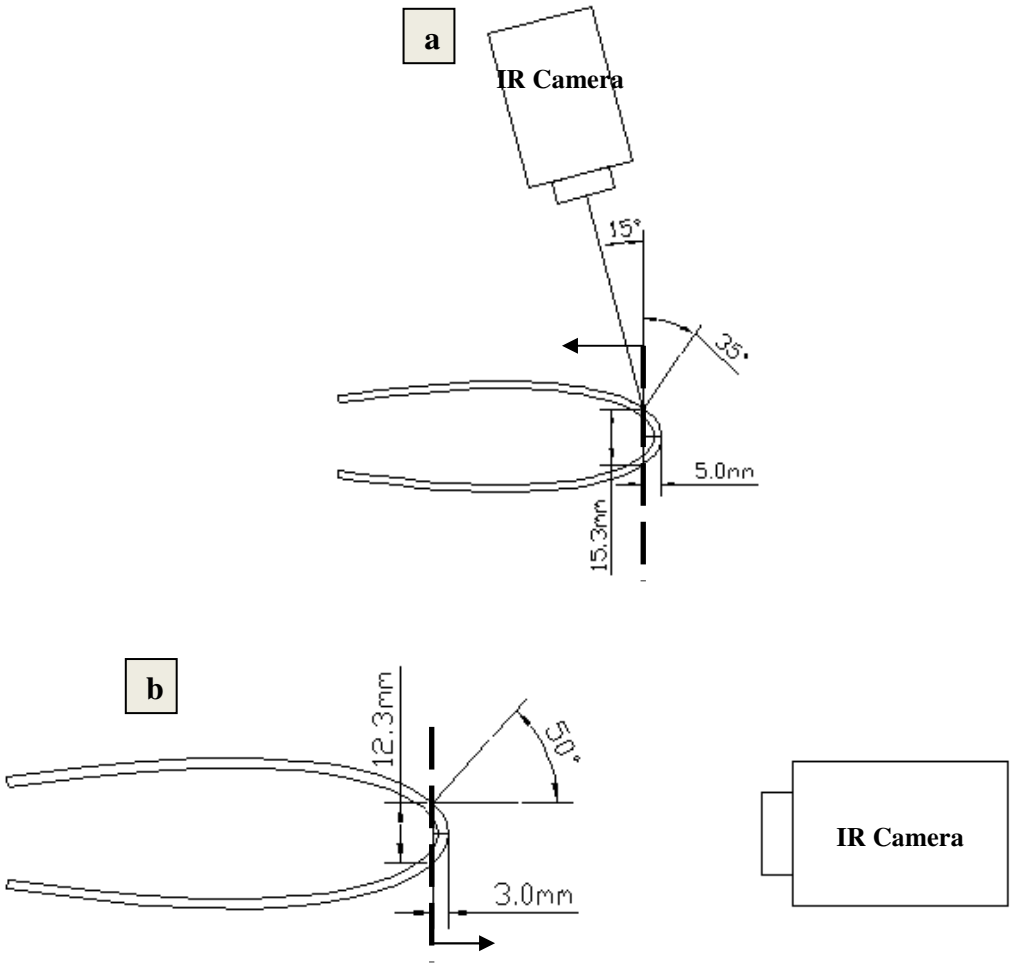

Figure B-16- The airfoil's profile, drawn in Solid Works, shows the region of the airfoil's surface that can be measured by the IR camera, (a) top surface of the airfoil: surface temperature of the left side of the dashed line can be measured, (b) leading edge of the airfoil: surface temperature of the right side of the dashed line can be measured.

When IR camera is positioned in the line of sight of the airfoil leading edge to measure the surface temperature of the leading edge region, as shown in Figure B-16(b), the IR camera can only measure the correct temperature at locations up to 2.05% of the airfoil's chord length, which is shown by the dashed line. Beyond the dashed line in Figure B-16(b), the measured temperatures are not accurate and reliable.

B.5 Calibration of the IR Window

The appropriate IR window for the icing conditions should have stable transmission rate at different temperatures and when they exposed to humidity and water spray. It should be durable in humid and cold conditions and its transmission rate should be consistent over time. Considering such properties, a polymeric IR window, i.e. VPFR-75, from IRISS, inc., was selected to be used in the cold (dry) and icing (wet) conditions. The transmittance of the IR polymer window is relatively constant at different target temperatures; and its specification in different environments is relatively stable over time [5, 6, 8].

In Table B-3, the properties of common materials used as IR window are given. As can be seen in Table B-3, the IR polymer is proper for long wavelength IR radiation, and it is not soluble in water, which is important in the icing condition. Also, in comparison with the most common materials used in IR windows, i.e. CaF_2 and BaF_2, which are crystal, IR polymer is not brittle.

Table B-3- Properties of common materials used as IR window [5].

Material	Chemical Symbol	Wavelength µm	Reflection (Two surfaces)	Knoop Hardness	Soluble in H_2O
Calcium Fluoride	CaF_2	0.13-10	5%	158	Yes
Sapphire	Al_2O_3	0.15-5.5	14%	2000	No
IR Polymer	N/A	0.15-22	21%	N/A	No
Germanium	Ge	1.8-23	53%	780	No
Zinc Selenide	ZnSe	0.5-22	29%	120	No
Barium Fluoride	BaF_2	0.15-12.5	7%	82	Yes

When using an external optic such as IR windows, the IR camera software compensates for transmission losses from the IR window. So, the transmission rate of the IR window should be measured for temperature measurement corrections by the IR camera.

Since the transmittance of an IR window depends on the IR camera sensor range, target temperature, window temperature and window material and thickness, the transmittance of the specific IR polymer window in our experimental setup should be measured by our IR camera [6]. Since the transmittance of the IR polymer window is relatively constant in different environments, the window transmittance was measured at room (~21˚C) condition, using the coffee cup test [5]. In this method, as shown in Figure B-17, a cup of warm water with temperature of ~55˚C with a high emissivity tape on the cup is used as the target (the water/cup temperature is about 35˚C hotter than the IR window, which is in room temperature). Since the temperature of the tape is known, the transmittance of the IR window is obtained through measuring the tape temperature with and without window. When measuring the tape temperature through the IR window, the transmittance

of the IR window in the camera software should be changed until the adjusted temperature is the same as the original temperature of the tape.

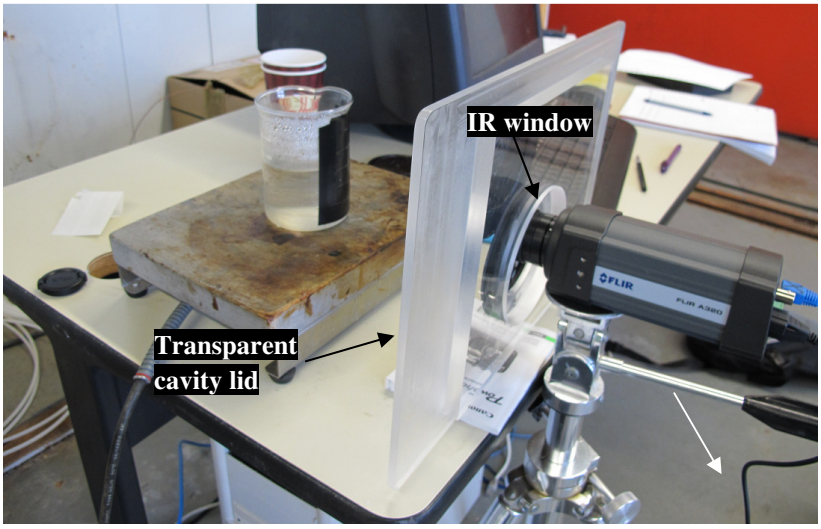

Figure B-17- Measurement of the IR polymer window transmittance using “coffee cup method”.

Although the transmittance of the IR polymer window is relatively independent of the target temperature [5, 6], but, for more accurate measurements, the IR polymer transmittance was measured for several target temperatures from ~50˚C to ~78˚C. The IR polymer transmittance changes from 0.76 to 0.73 in the target temperature range of ~50˚C to ~78˚C, respectively. In most cases for high emissivity targets, which is applicable for the composite material with the emissivity of 0.94 in this study, this transmittance changes should not be a problem [6]. So, the transmittance of the IR polymer window was considered 0.75 at different test conditions.

The IR polymer window was also calibrated for the testing conditions in the wind tunnel for cold (dry) and icing (wet) conditions at -17±1˚C. To calibrate the IR window for the

dry tests condition without water spray, surface temperature of the airfoil was measured at different testing room temperature (see Table B-2), as described in Section 4.3.1.

In icing (wet) condition, as described in Section 2, to protect the IR window from icing, warm air was blown over the inside surface of the IR window. To investigate the effect of the blowing warm air on the IR window and the IR camera measurements, two tests were conducted on the energized composite airfoil, i.e. airfoil I, in cold (dry) condition at -17±1˚C; once with blowing warm air over the IR window, and once without blowing warm air over the IR window. The test conditions and the applied power to the anti-icing system of the airfoil in the two tests were kept the same.

Figure B-18 and Figure B-19 show IR images of the energized composite airfoil surface, captured by the IR camera through the IR polymer window, without and with blowing warm air over the window, respectively. Surface temperature of the airfoil was measured at different points along the black lines on the IR images in Figure B-18 and Figure B-19. The locations of the selected points on the images were the same in Figure B-18 and Figure B-19, to compare the temperature of the corresponding points.

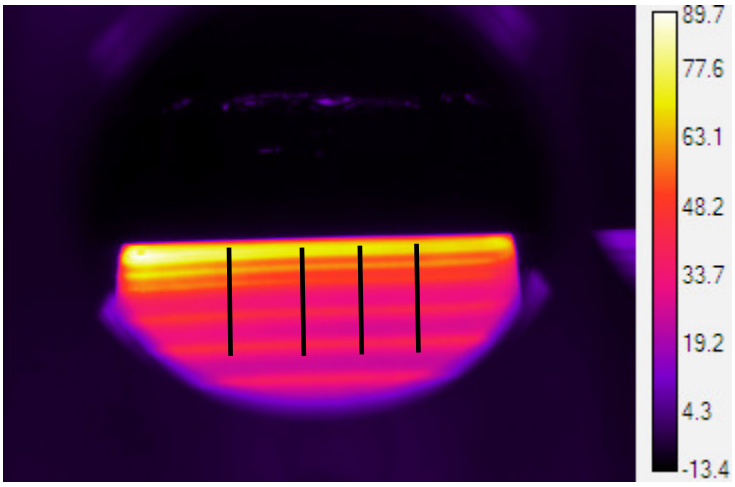

Figure B-18- IR image of the energized composite airfoil's surface in cold (dry) condition, without blowing warm air over the IR window; surface temperature was measured along the vertical black lines on the IR image.

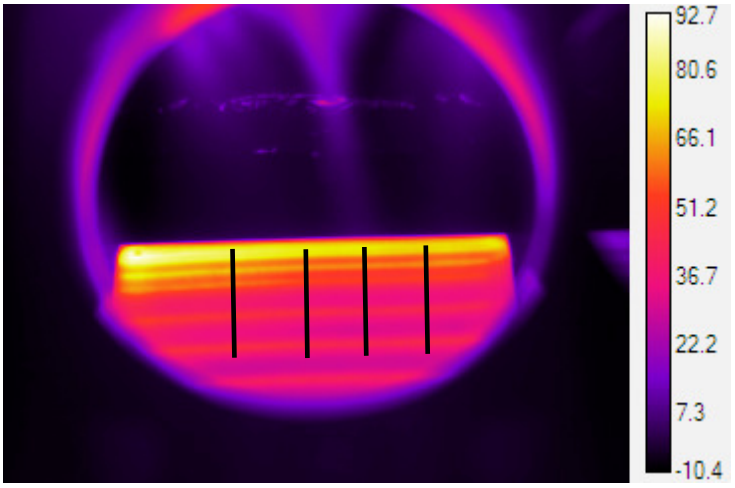

Figure B-19- IR image of the energized composite airfoil's surface in cold (dry) condition, with blowing warm air over the IR window; surface temperature was measured along the vertical black lines on the IR image.

The yellow (light colored) lines in the IR images in Figure B-18 and Figure B-19 represent the embedded thermal elements' locations in the composite airfoil. Temperatures of the selected points on top of the thermal elements and at their midpoints on the airfoil surface were compared in Figure B-18 and Figure B-19. Comparison of the airfoil's surface temperature in Figure B-18 and Figure B-19 showed that the measured airfoil's surface temperature with blowing warm air over the IR window is about 3˚C higher than that of without the warm air.

Considering the effects of the IR window and the warm air on the IR camera temperature measurements, calibrated surface temperature of the airfoil in icing (wet) condition is 6˚C lower than the measured surface temperature by the IR camera. In this study, we did deduct 6˚C in all of the relevant data presented in Chapters 3 and 4 of the thesis.

B.6 References

[1] J. H. Tan, E. Y. K. Ng, U. R. Acharya, C. Chee, 2009, "Infrared thermography on ocular surface temperature: A review", Infrared Physics Technol., 52, pp. 97-108.

[2] FLIR Systems, Inc., "The Ultimate Infrared Handbook for R&D Professionals".

[3] D. Wei, C. Jing, A. Ying, 2009, "Analysis of working range in IR camera measurement", Proc. of SPIE Vol. 7283, 728341, pp.1-6.

[4] FLIR Systems, Inc., "User's manual for FLIR A320 & A325", 2008.

[5] IRISS, Inc., "10 things you need to know about infrared windows", 2009.

[6] R. P. Madding, 1999, “Emissivity measurement and temperature correction accuracy considerations”, SPIE conference on Thermosense XXI, Vol.3700, Florida.

[7] C. Öhman, 2001, “Measurement in Thermography”, FLIR Systems AB, Publ. Nos. FLIR: 1 557 498 Rev. A – ITC: 1 560 055 Rev. A.

[8] J. DeMonte, 2009, “Transmission stability and infrared windows: the effects of transmissivity on data accuracy”, http://www.iriss.com/, Accessed October 7, 2011.

Appendix C

C. Thermal Analysis of the Polymer Composite Airfoil with the Anti-icing System

C.1 Introduction

The anti-icing system for the composite airfoil inserts consists of electrical thermal elements in the form of wires embedded inside of a woven fiber-glass/epoxy composite in the form of flat sheets. The composite flat sheets were then cured in a mold to shape the composite airfoil NACA 0021 insert, shown in Figure C-1. The composite insert is mounted into an aluminum fixture, shown in Figure C-1, to shape the NACA 0021 airfoil with the chord length of 146mm.

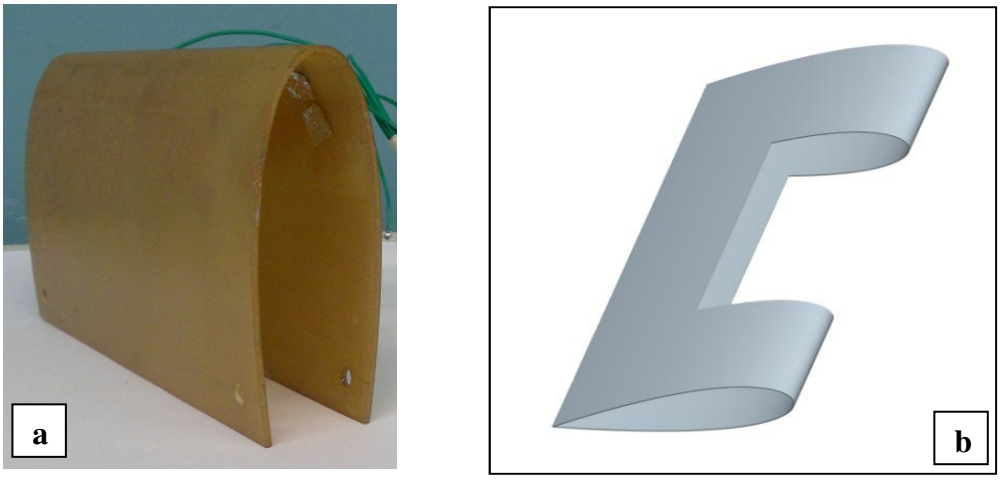

Figure C-1- (a) polymer composite airfoil insert; (b) aluminum fixture for mounting composite airfoil insert [1].

In the present application of polymer composite materials with embedded thermal elements, the composite materials may potentially be subjected to high temperatures due to the powering of the heating system (wires). When polymer composites, which inherently have low thermal conductivities, are exposed to high temperatures above or close to their maximum service temperature, their properties change, and they irreversibly be damaged. So, knowing the thermal elements' surface temperature inside the composite structure is important to prevent degradation in the material's properties due to the overheating.

Temperature distribution on the airfoil's surface and uniformity of surface temperature distribution are other important parameters. This information is used in determining the thermal elements' spacing and location to prevent ice formation on the airfoil's surface and minimizing the power consumption.

In this appendix, surface temperature of the embedded thermal elements and temperature distribution inside the composite airfoil insert as well as its surface temperature distribution were numerically simulated by a steady-state two-dimensional thermal model. The simulation with ABAQUS 6.9 student version from SIMULIA® has been performed for thermal analysis of the composite airfoil with the anti-icing system in cold (dry) condition at -17˚C, i.e. there was no icing.

C.2 Heat transfer model

To model the heat transfer for the airfoil, only half of the airfoil was modeled due to symmetry in the airfoil's shape and heat transfer conditions. The entire airfoil was modeled as a flat plate for simplicity and realizing that we are interested in ideas principally. A steady-state, two-dimensional (*x*-*y*) heat conduction equation has been solved for the thermal elements in a rectangular coordinate system:

$$\frac{\partial}{\partial x}\left(k_x \frac{\partial T}{\partial x}\right) + \frac{\partial}{\partial y}\left(k_y \frac{\partial T}{\partial y}\right) = 0 \tag{1}$$

Figure C-2 shows a schematic of the coordinate system of the composite flat plate with embedded thermal elements. The origin of *xy* coordinate system is at the left corner and mid thickness of the plate in Figure C-2. The heat transfer from the top surface of the airfoil is mainly by forced convection (ignoring radiation heat transfer), and the bottom surface is assumed to be insulated, since it is the inside surface of the airfoil which is constrained [2]. So, the boundary conditions on the top and bottom surfaces of the flat plate were considered forced convection and isolation, respectively. The boundary conditions for the other two sides of the rectangle were considered adiabatic due to the symmetry of the system. The heat transfer rate at the top and bottom surfaces and the adiabatic conditions are given by:

$$q_y = -k_y \frac{\partial T\left(\frac{b}{2}\right)}{\partial y} = -h\,(\mathrm{T_S} - \mathrm{T_\infty}) \qquad \text{(Top surface)} \tag{2}$$

$$q_y = -k_y \frac{\partial T\left(-\frac{b}{2}\right)}{\partial y} = 0 \qquad \text{(Bottom surface)} \qquad (3)$$

$$q_x = -k_x \frac{\partial T(0)}{\partial x} = 0 \qquad \text{(Left Corner)} \qquad (4)$$

$$q_x = -k_x \frac{\partial T(a)}{\partial x} = 0 \qquad \text{(Right Corner)} \qquad (5)$$

where, q_x is heat flux in x direction (W/m^2), q_y is heat flux in y direction (W/m^2), k_x is thermal conductivity of the composite flat plate in x direction (W/m.K), k_y is thermal conductivity of the composite flat plate in y direction (W/m.K), h is convection heat transfer coefficient (W/m^2.˚C), T_∞ is ambient room temperature (˚C), T_S is surface temperature of the composite plate (˚C), a is the length of the rectangular flat plate (m), b is the flat plate (airfoil) thickness (m).

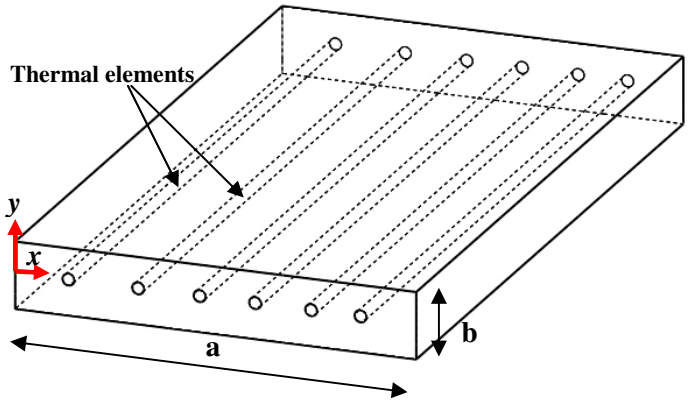

Figure C-2- Schematic of composite flat plate with embedded thermal elements.

Modeling the entire airfoil as a flat plate is an acceptable simplification since calculating convection heat transfer coefficient is done through using flat plate approximation [3], as

will be explained next. Also, we will verify the flat plate simplified model through comparing experimental results with the modeling ones.

C.2.1 Convection heat transfer coefficient of the airfoil

There are two methods for calculating the heat transfer coefficient over an airfoil: the "flat plate" approximation and the "wedge flow" approximation [3, 4]. The results from the "flat plate' approximation appears to be satisfactory for thin airfoils, and for most purposes [4]. In this study, the "flat plate" approximation was used to calculate the convection heat transfer coefficient over the surface of the composite airfoil insert.

In the "flat plate" approximation, the airfoil surface was considered as a combination of a cylinder on the leading edge and a flat plate beyond the leading edge. The known equations for the heat transfer from a cylinder and a flat plate will then be applied for the airfoil surfaces [3, 4].

The composite airfoil inserts' dimension is shown in Figure C-3. The leading edge with the radius of curvature, R, is considered as a cylinder with radius of R; R is used in heat transfer equations for a cylinder. The leading edge region was considered as 2.46% of chord length, and its end point is shown in Figure C-3 by the arrow and the angle. The region between the leading edge end point and the dashed line in Figure C-3, which is the end point of the composite airfoil insert, was considered as the flat plate. The end point of the leading edge and its dimensions was obtained from the Solid Works drawing of the airfoil in this study. Considering the thermal elements position shown in Figure C-4, the

leading edge region was considered from wire 1 up to wire 2; i.e. half of wire 1 (at the stagnation point), wires 1-1, 1-2, and 1-3.

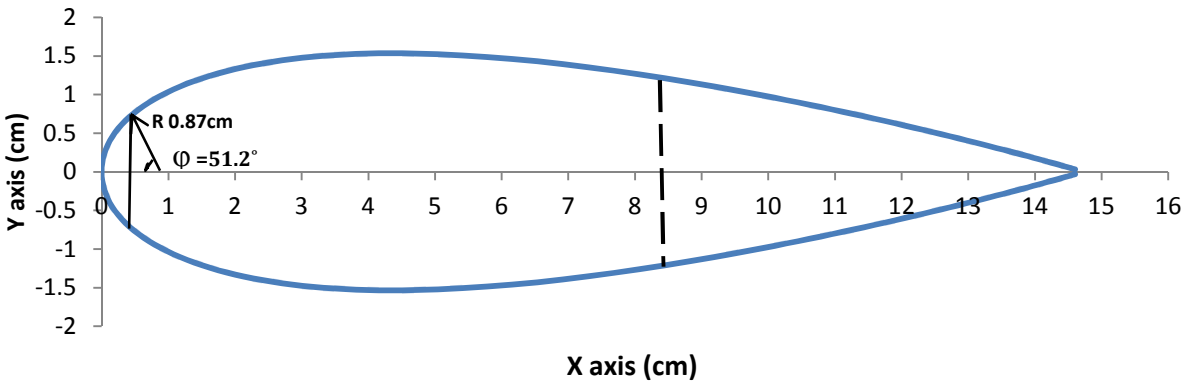

Figure C-3- NACA 0021 airfoil dimension used for making composite airfoil inserts, dashed line shows the end of insert.

It should be mentioned that the flow over the airfoil is laminar due to the maximum Reynolds number of about 1.5×10^5, and assumption that there is no significant turbulence in the wind tunnel. The convection heat transfer coefficient of different regions of the composite airfoil, used in ABAQUS simulation, was calculated for the airfoil tested in cold (dry) condition, i.e. no icing, with ambient temperature of -17˚C and wind tunnel air velocity of 27.7m/s.

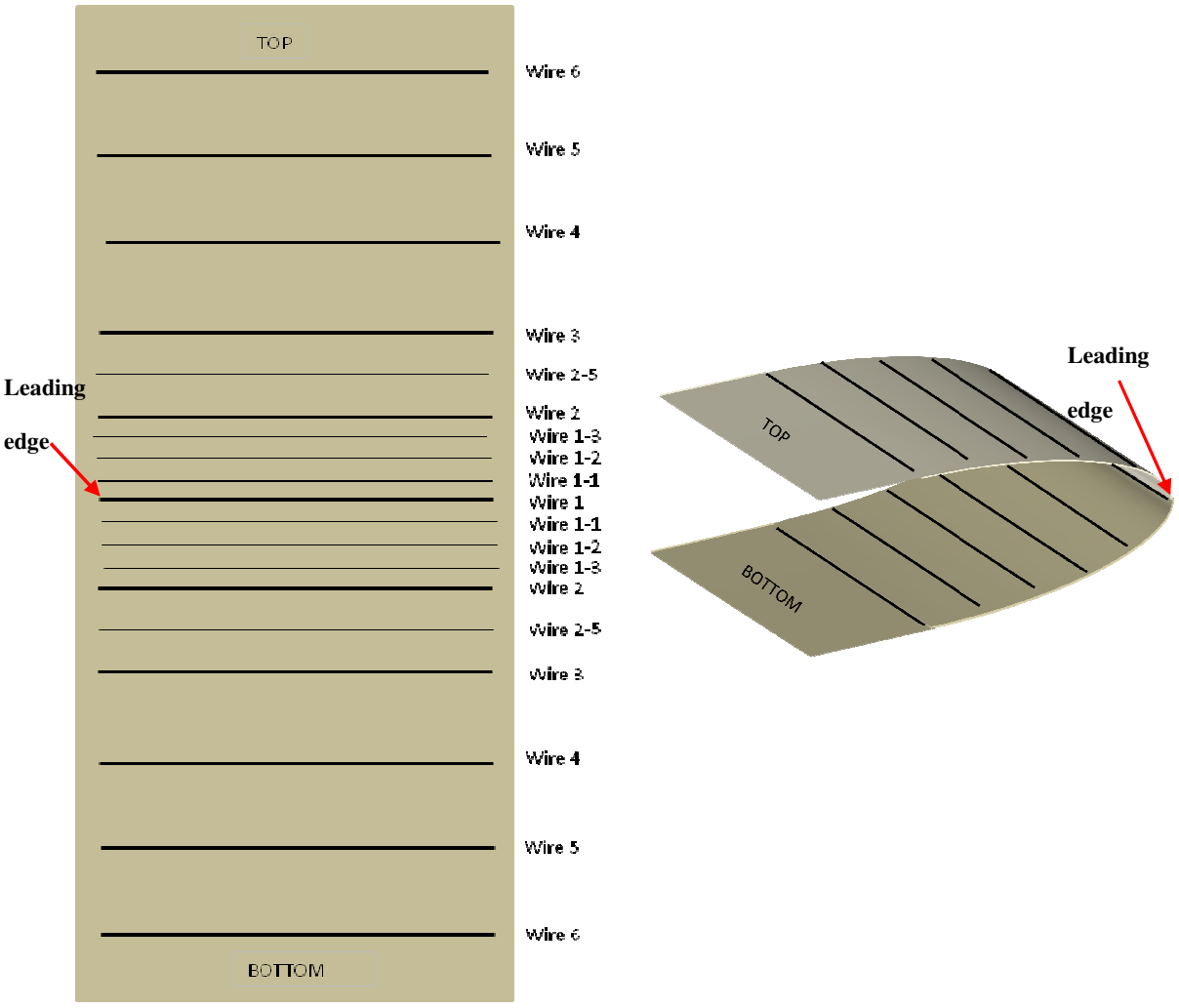

Figure C-4- Left: Thermal elements' spacing before the airfoil has been shaped; right: schematic of the composite airfoil with a total of 19 embedded thermal elements. The four thermal elements from wire 1 till wire 2 were placed with 2.5mm spacing from each other, and a thermal element, i.e. wire 2-5, was placed in the middle of wires 2 and 3. The spacing between the rests of the thermal elements, beyond thermal element 3, is 10mm. Pattern of the thermal elements on the bottom side of the airfoil is similar to the top side.

The convective heat transfer coefficient changes across the leading edge from the stagnation point, in Figure 3 where φ=0, to the end point of the leading edge where φ=51.2˚. To have an average convective heat transfer coefficient over the leading edge

region, Nu numbers of different points on the leading edge were calculated as follows [3]:

$$Nu_{stag} = 1.14\ Pr^{0.4} Re_D^{0.5} \quad (6)$$

$$Nu_{\varphi} = hD/k = 1.14\ Pr^{0.4} Re_D^{0.5}\ [1-(\varphi/90)^3] \quad (7)$$

$$Re_D = UD/v \quad (8)$$

$$\varphi = (360/\pi)\ (s/D) \quad (9)$$

where, Nu_{stag} is the Nusselt number on the stagnation point of the cylinder (φ=0), Nu_{φ} is the local Nusselt number over the cylinder at φ, Pr is Prandtl number, Re_D is Reynolds number of the cylinder with diameter of D, h is the local convective heat transfer coefficient over the cylinder (W/m^2.˚C), k is thermal conductivity of the air (W/m.K), φ is central angle of cylinder measured from stagnation point, U is the airflow velocity outside the thermal boundary layer (free stream velocity), v is dynamic viscosity of the air (kg/m.s), s is the curvilinear length over the airfoil measured from stagnation point on the leading edge region.

An average convective heat transfer coefficient "$h_{average}$" is calculated for the leading edge region of the airfoil by [5]:

$$h_{average} = \frac{1}{S} \int_S hdx = \sum_{i=1}^{3} h_i\ \Delta s_i \quad (10)$$

where, S is total length of the circumference of leading edge region, h_i is the local convection heat transfer coefficient of the selected points (i) on the leading edge surface,

Δs_i is the difference between curvilinear lengths of two consecutive points over the airfoil measured from stagnation point on the leading edge region.

In equation 10, four points on the leading edge region of the airfoil was selected to calculate the average convection heat transfer coefficient. The properties of air were obtained at the average film temperature which is given by:

$$T_f = (T_s + T_\infty)/2 \quad (11)$$

where, T_f is the average film temperature of a specific surface which are the cylinder (leading edge) and the flat plate (beyond the leading edge) surfaces, T_s is the designated surface temperature on the airfoil (leading edge / beyond the leading edge) which is measured by the IR camera, T_∞ is the air temperature (ambient, cold room temperature = -17˚C).

The average $h_{average}$ value for the leading edge region of the airfoil, up to wire 2 of the anti-icing system, was calculated using the equations 6-11 as 254.1W/m^2.˚C. Heat transfer from the remainder of the airfoil, after the leading edge region, in the laminar flow, was calculated by considering the equations of a flat plate as follows [6]:

$$Nu_{ave.} = hL/k = 0.664\ Re_L^{0.5}\ Pr^{1/3} \quad (12)$$

$$Re_L = UL/\nu \quad (13)$$

where, $Nu_{ave.}$ is the average Nusselt number over the entire plate, L is the length of the flat plate.

Considering the equations 11-13, the average convection heat transfer coefficient was calculated as 71.9W/m^2.˚C for the region from wire 3 to wire 6. Values of different parameters used in calculating the convection heat transfer coefficient for different regions of the airfoil is presented in Table C-1.

Table C-1- Parameters for convection heat transfer coefficient calculation of the airfoil.

Parameter	**Leading edge region**	**Flat plate region**
U (m/s)	27.7	27.7
D (m)	0.0174	-
L (m)	-	0.08
ν (m^2/s)	1.562×10^{-5}	1.470×10^{-5}
Pr	0.7296	0.7323
Re	30856.6	150748.3
$Nu_{ave.}$	-	232.4
Nu_{stag}	175.7	-

Also, a transition region was considered on the airfoil from the leading edge region to the flat plate region, including wires 2 and 2-5 of the anti-icing system. The average convection heat transfer coefficient for this region was considered as the average *h* values of the end point of the leading edge (at $\varphi = 51.2^{\circ}$) and the flat plate region. The *h* value for the transition region was calculated as 141W/m^2.˚C.

C.3 Geometry, Modeling Parameters and Boundary Conditions

The schematic of the side view of half of the airfoil which was considered as a flat plate, and more detailed schematics of different regions are shown in Figure C-5. It should be mentioned that the spacing between thermal elements are different at different regions,

shown in Figure C-4; 2.5mm space between adjacent wires on the leading edge region, 5mm space between wires in the transition region and 10mm space between wires in the beyond transition region.

The modeling for the area beyond transition region was done only for wires 3 and 4, and wires 5 and 6 were not considered in the modeling. Because, heat transfer for wires 4, 5 and 6 is symmetric due to the same amount of input power for the wires of 4 to 6, equal spacing between these wires, and the same amount of h value . Since an average Nusselt number was assumed in h value calculation, the h value can be considered constant over the area beyond transition region.

The boundary conditions of the top and bottom surfaces of the plates, as mentioned earlier, are forced convection, and isolation, respectively. The boundary conditions for the other two sides of the rectangles were assumed adiabatic ($q_x = 0$). The boundary conditions for the thermal element surfaces were considered as constant heat flux representing the power density, i.e. the amount of power applied to a unit area of the thermal element's surface, for each thermal element. The amount of applied power and power density of the heating system of the airfoil is provided in Table C-2. These amounts of power are the minimum required power for the anti-icing system with the specific pattern, to provide an ice free surface of composite airfoil under the icing (wet) conditions.

Item No.	Part Number
1	Wires 3 and 4 region
2	Wires 2, 2-5 region
3	Leading edge region
4	Wire
5	Wire 1(half)

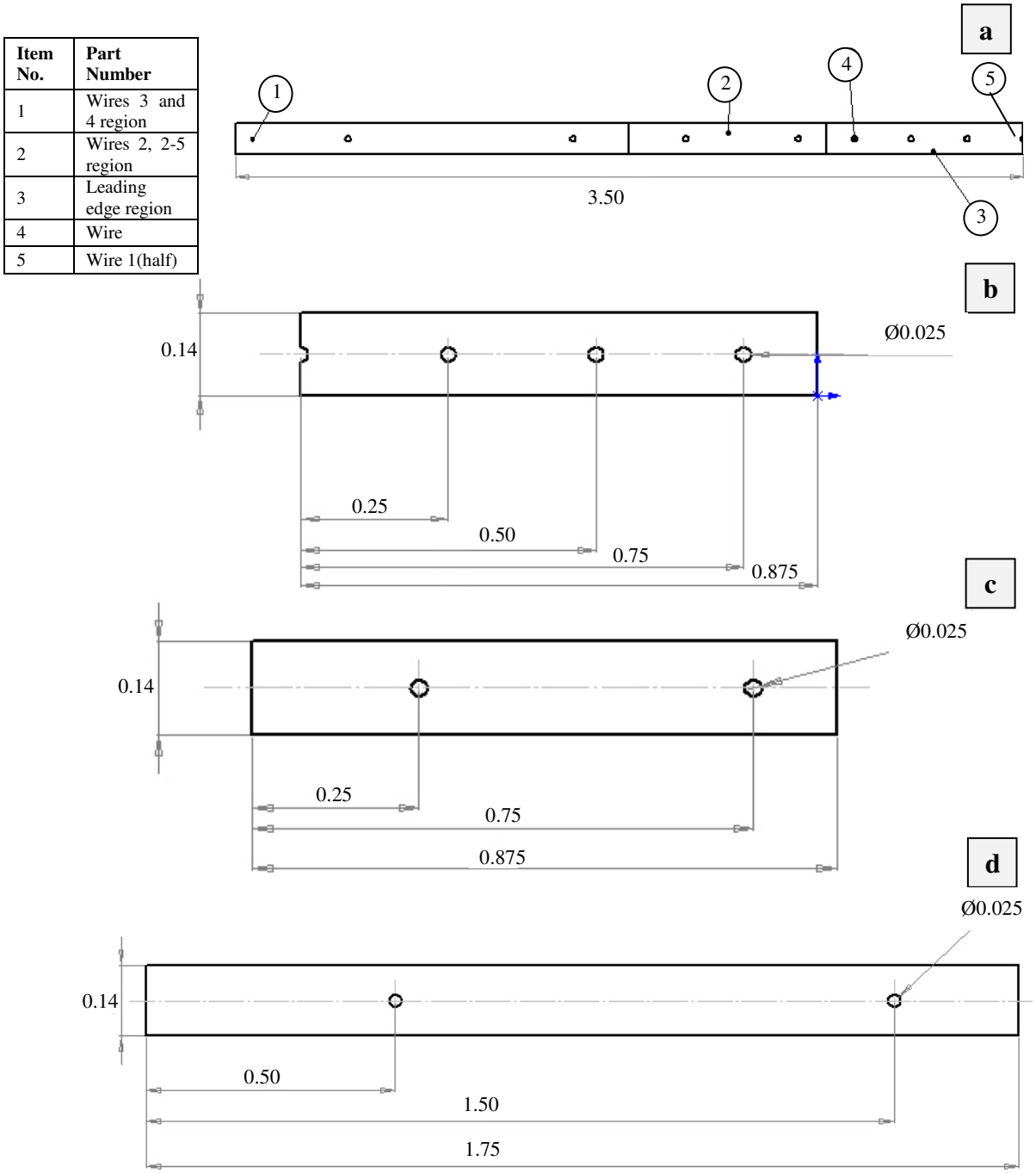

Figure C-5- Schematic of the side view of the airfoil modeled as a flat plate with embedded thermal elements, (a) upper part of the composite airfoil insert up to wire 5, (b) leading edge consisting wires 1(half), 1-1, 1-2 and 1-3, (c) transition region consisting wires 2 and 2-5, (d) beyond transition region consisting wires 3 and 4 (The dimensions are in cm). Figures (b) to (d) are detailed view of stuff in (a).

Table C-2- Applied power to the heating system of airfoil (II) in cold dry and wet conditions, to attain the stated powers, current and voltage were in the range of 2.1-3.7A and 1.4-4.5V, respectively

Thermal element	Power scheme 2 (W)	Power density (kW/m^2)
1 (Leading edge)	10.1	89.0
1-1, 1-1’	9.1	79.9
1-2, 1-2’	8.7	76.6
1-3, 1-3’	5.6	49.0
2, 2’		
2-5, 2-5’		
3, 3’	4.9	43.4
4, 4’		
5, 5’		
6, 6’ (Trailing edge)		
Total power	118.7	
Average power intensity (kW/m^2)	8.3	

C.3.1 Thermal conductivity of the composite material

In this research, polymer composite laminates were manufactured from a commercially available aerospace-grade fiberglass/epoxy prepreg, i.e., Necote E-765 epoxy/fiberglass prepreg (7781 E-Glass). The reinforcing phase in this prepreg is woven fiberglass (E-glass) fabric. The specification of the selected prepreg is provided in Appendix A (fabrication of the composite airfoil).

Transverse thermal conductivity of the composite was calculated using Rayleigh, Springer and Tsai, and Halpin-Tsai models. Longitudinal thermal conductivity was obtained based on mixing rule. These models are described in the “Introduction Chapter” of this thesis. Since thermal conductivity of the resin is not provided by the supplier, it is

determined using literature values [7, 8]. Thermal conductivity of an aromatic epoxy resin cured with amine curing agent which is similar to the resin in the prepreg used, is 0.24W/m.K at 25˚C [7]. This value was considered as the epoxy resin thermal conductivity. Since composite materials are orthotropic materials which have different properties in different directions, two main thermal conductivities in longitudinal and transverse direction of fibers were calculated.

In the above mentioned models for calculating thermal conductivities, volume fractions of the resin (matrix) and the fiber are required. Fiber volume fraction of an unknown glass fiber composite can be measured by burning the composite. It is calculated by:

$$V_f = (\rho_c / \rho_f) W_f \quad (14)$$

$$W_f = m_f / m_c \quad (15)$$

$$\rho_c = \rho_f V_f + \rho_m (1 - V_f) \quad (16)$$

where, V_f is fiber volume fraction, ρ_c is composite density, ρ_f is fiber density, ρ_m is resin (matrix) density, W_f is fiber weight fraction, m_f is weight of fiber in a composite sample, m_c is weight of composite sample.

A burning experiment was done. By measuring the fiber and resin volume fractions of the polymer composite materials, and using the above mentioned models, the thermal conductivities of the material were calculated as shown in Table C-3.

Table C-3- Thermal conductivities of the polymer composite material.

Parameter	Value	Parameter	Value
W_f	0.62	$k_{c,22}$ (transverse) (Rayleigh), (W/m.K)	0.45
V_f (%)	44	$k_{c,22}$ (transverse) (Halpin-Tsai), (W/m.K)	0.44
k_p (W/m.K)	0.24	$k_{c,22}$ (transverse) (Springer and Tsai), (W/m.K)	0.42
k_f (W/m.K)	1.3	$k_{c,22}$ (transverse) (average), (W/m.K)	0.43
$k_{c,11}$ (longitudinal), (mixing rule), (W/m.K)	0.71		

In Table C-3, k_p, k_f and k_c represent the thermal conductivities of polymer (resin), fiber and composite, respectively. The calculated transverse thermal conductivities by Rayleigh, and Halpin-Tsai models are in good agreement with the experimental results obtained by Y. Gowayed *et al.* [9] for fiber glass woven composites. Thermal conductivities of the composite material, in longitudinal (*x*) and transverse (*y*) directions were calculated as 0.71W/m.K and 0.43W/m.K, respectively.

The composite material in this study was considered as a single layer, due to its woven cloth fibers which have the same direction in different layers. It was also assumed that the transverse heat flux is continuous at ply interfaces. To model heat transfer in the composite material, thermal behavior (conductivity) must be defined in the materials section of ABAQUS. An orthotropic material with two thermal conductivities in *x* (k_x= 0.71) and *y* (k_y= 0.43) directions was defined.

C.4 Mesh, Steps and Analysis in the ABAQUS Modeling

An element type DC2D4: 4-node linear heat transfer quadrilateral has been used for meshing the model. The selected approximate global size is 150μm (see section 5.1). It should be noted that finer mesh was not possible due to limitation of ABAQUS Student Edition. The analysis was done in one step which was "heat transfer" type, and the "steady-state" option was selected for analysis. Convective heat transfer on the top surface of the composite sheet was defined using "Interaction" option, defining convection heat transfer coefficient (h) as the "Film coefficient", and ambient room temperature (T_∞) as the "Sink temperature". In ABAQUS software, heat flux boundary conditions in the heat transfer problems should be defined as a load; so, all of the other four boundary conditions, which are heat fluxes, were defined as loads in the system.

Temperatures of different nodes inside and on the top surface of the composite flat plates were recorded as a function of their relative distance from the bottom surface, i.e. inside surface of the airfoil. Simulated surface temperature profiles of the flat plates were also compared with the measured surface temperature of the airfoil by the IR camera.

C.5 Results and Discussion

The airfoil's surface temperature distribution and maximum temperature of the thermal elements are important parameters in designing the heating system. Temperature distribution should be as uniform as possible in-between the wires. The surface temperature of the thermal element must be less than the maximum working temperature

of the composite material, i.e. 137˚C, to prevent permanent damage of the composite material.

The ABAQUS simulated temperature distribution profile of the composite flat plate for the leading edge, transition and beyond transition region are shown in Figure C-6. As can be seen from Figure C-6, in all regions of the airfoil, surface temperature of the embedded thermal elements is the highest within the region. The minimum temperature is observed on the top surface of the flat plates, which are representing the midpoints of the two consecutive thermal elements in the composite airfoil.

Looking at the right panel of Figure C-6, one can see that the maximum surface temperature of the thermal elements is 127.6˚C in the leading edge region of the airfoil. This temperature is less than the maximum working temperature of the composite material, i.e. 137˚C. It means that the applied powers, i.e. power scheme 2 (Table C-2), to different thermal elements in all of the airfoil regions were safe enough to prevent permanent damage of the composite material due to the overheating and burning. The minimum surface temperature of the airfoil, from different regions, is ~22˚C which is observed in Figure C-6(c), between wires 3 and 4, and wires 4 and 5 (not shown here) with 10mm spacing.

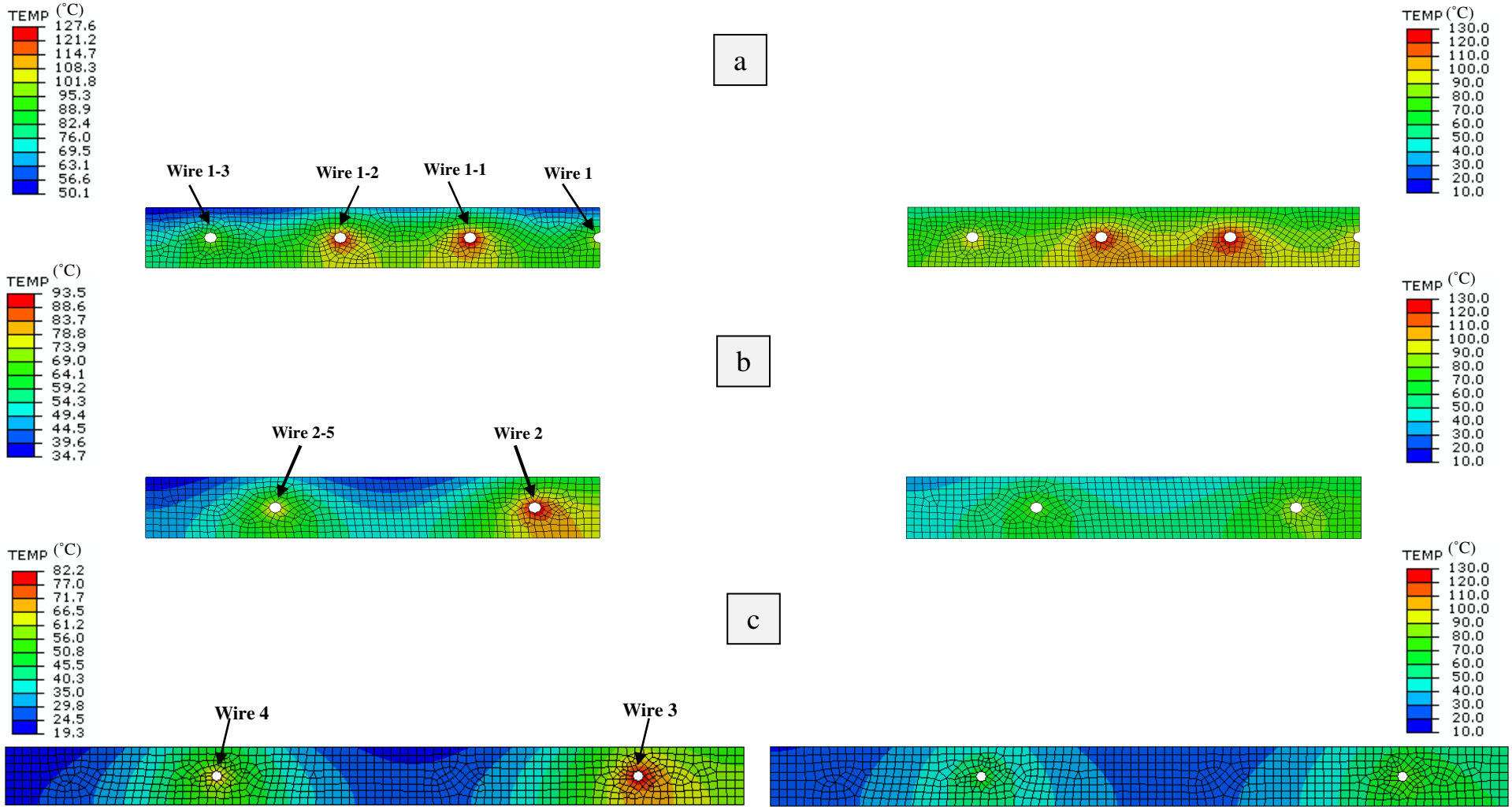

Figure C-6- Temperature distribution profile of the composite airfoil insert, (a) leading edge region, (b) transition region, (c) beyond transition region; panels in the left show temperature distributions with individualized, coloring scale to give details; whereas, panels on the right have the same coloring scale to facilitate temperature comparisons between different regions.

Figure C-6 also shows that for each region with a specific *h* value, the surface temperature of the wires is proportional to the amount of the applied power and their spacing. The wires with higher power, as well as the ones positioned closer to each other (smaller wires' spacing) show higher surface temperature than those with lower power input or embedded further from each other.

Figure C-6(a) shows that the temperature difference between the hottest and coldest points on the airfoil surface on the leading edge is ~ 19˚C; while for the transition region shown in Figure C-6(b), this temperature difference is ~24˚C, and for beyond transition region of the airfoil is ~31˚C in Figure C-6(c). This shows that surface temperature distribution is more uniform on the leading edge, and the temperature uniformity decreases from the leading edge to the trailing edge of the composite airfoil insert. This is because of the size of the spacing between thermal elements; smaller spacing on the leading edge region leads to more uniform surface temperature distribution; while larger spacing in the transition region and beyond that results less uniform temperature distribution on the airfoil surface.

In Figure C-6(b), the amount of applied power to wires 2 and 2-5 is equal, but the airfoil surface temperature on top of wire 2 is higher than that of wire 2-5. This is because of the smaller spacing between wire 2 and its adjacent wire 1-3 (2.5mm) than that of wire 2-5 and wire 3 (5mm).

In Figure C-7, temperature distributions along the plates' thickness are shown at two selected points for each region; one at the wires and one at the midpoint of adjacent wires. As can be seen in Figure C-7, the inside temperature of the plates at the midway of neighbor wires decreases by moving from the bottom surface of the plates to the top surface, which, forced convection heat transfer exists. Temperature of the plates' bottom surface for different regions, are higher than that of the top surface, since the bottom surfaces represent the inside surface of the airfoil which assumed to be insulated.

Also, Figure C-7 shows temperature is the maximum on the wires' surface and it decreases by moving from the wires' surface to the top surface of the airfoil. The peaks of the graphs represent the wires' surface temperature for different regions at wires location. Temperature profiles inside the composite plates also show that the slope of graphs decreases from the leading edge region with highest convection heat transfer coefficient to the beyond transition region with the least heat transfer coefficient.

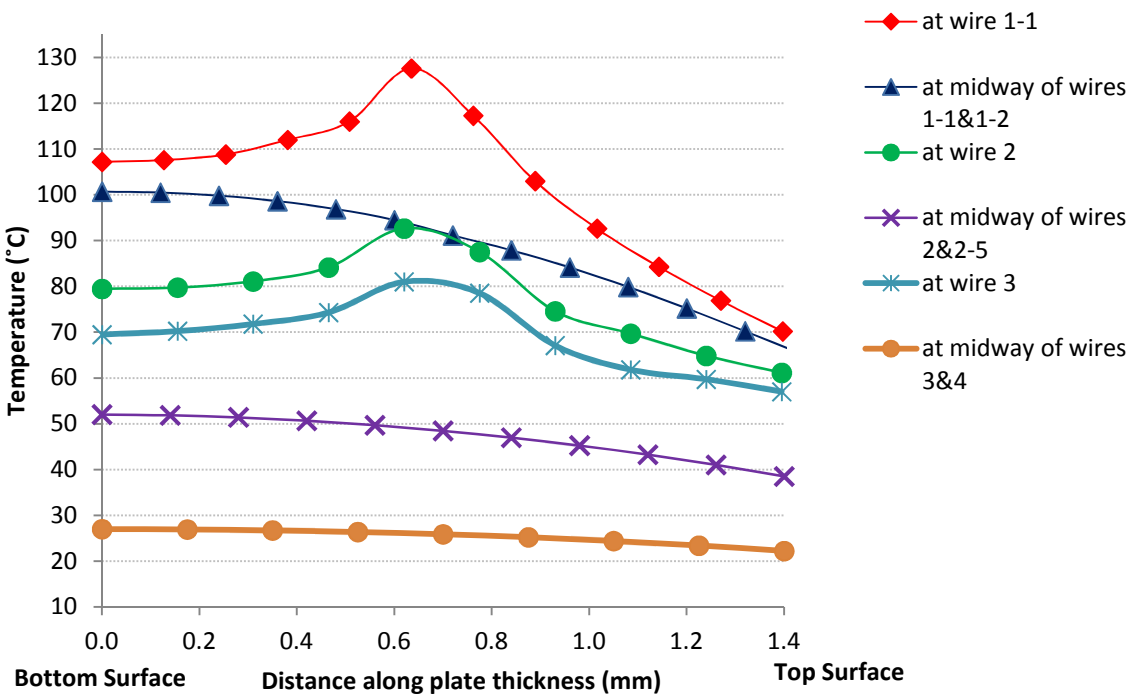

Figure C-7- Temperature distribution along the composite plate thickness for different regions.

Figure C-8 shows the resultant heat flux distribution inside the flat plate for the leading edge region. As can be seen the maximum heat flux is observed around the thermal elements and it decreases by moving from heating source to the outside. The heat fluxes vectors for two other regions of the airfoil are similar to Figure C-8, and are not shown here.

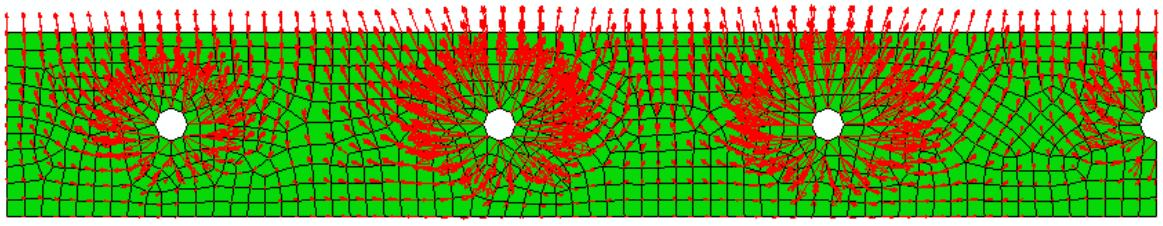

Figure C-8- Heat flux vectors at integration points of the leading edge region of the composite airfoil insert.

C.5.1 Effect of the Mesh Size

The effect of the mesh size on resultant temperature distribution was investigated for the transition region of the composite plate, using different mesh sizes of 440μm, 300μm, 200μm and 150μm with 8 mesh number around the thermal elements. Also, the effect of number of meshes around the thermal elements was studied. Figure C-9 shows the temperature profile of the transition region with the mesh size of 150μm and 16 meshes around the wires. Mesh number around the wires in Figure C-9 was doubled compared to that of in Figure C-6(b).

Temperature distribution along the thickness of the transition region at the location of wire 2 was measured for the bottom and top surfaces of the plate, and on the surface of wire 2 for different mesh sizes, presented in Table C-4 as well as Figure C-10. Also, temperature changes of three different points of the composite plate, i.e. bottom surface, top surface and wire 2 surface, are shown in Figure C-11and Figure C-12 as a function of the mesh size and the number of mesh around the wires, respectively. The mesh size in Figure C-12 is 440μm.

It can be seen from Table C-4 and Figure C-10 and Figure C-11 that the resultant temperature values at different points do not change considerably with the mesh size, when the number of meshes around the wires is the same. But, as shown in Figure C-12, when the number of mesh around the wires increases, temperature of different points of the plate increases. Temperature of different points converges within ~1% for 16 and higher number of mesh around the wires.

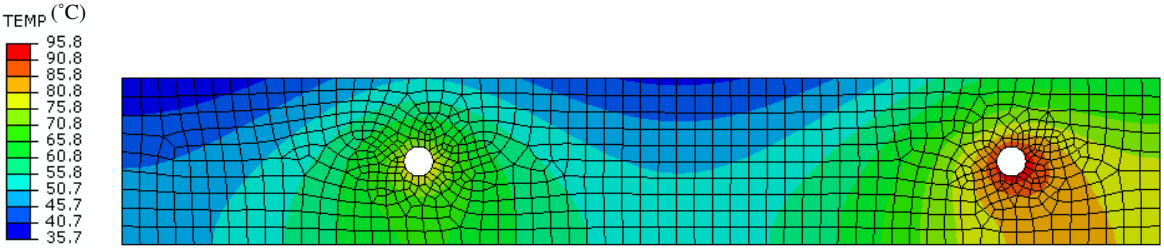

Figure C-9- Temperature profile of the transition region of the composite airfoil insert with 16 meshes around the thermal elements.

Table C-4- Effect of the mesh size on temperatures of the bottom, and top surfaces as well as wire surface for the transition region at the location of wire 2.

Mesh size (µm) / Distance from the bottom of plate(mm)	Temperature (˚C)						
	440µm	**300µm**	**200µm**	**150µm**	**150µm-16 mesh around wires**	**440µm-30 mesh around wires**	**440µm-16 mesh around wires**
0.0 (bottom surface)	78.7	79.4	79.5	79.5	81.6	81.2	80.5
0.8 (wire surface)	92.4	93.1	92.9	93.5	95.7	95.9	94.9
1.4 (top surface)	60.4	61.0	61.1	61.1	62.8	62.2	61.6

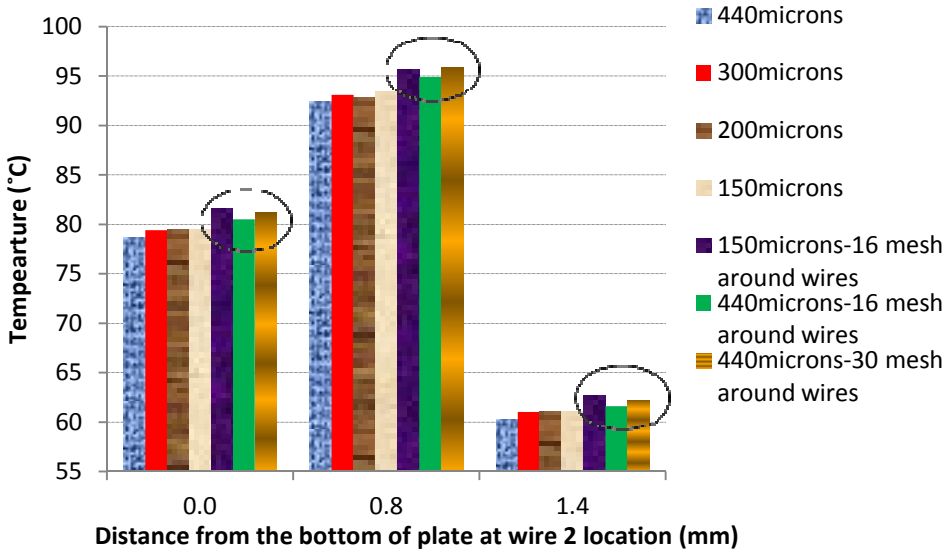

Figure C-10- Effect of the mesh size on temperatures of the bottom, and top surfaces as well as wire surface for the transition region at the location of wire 2.

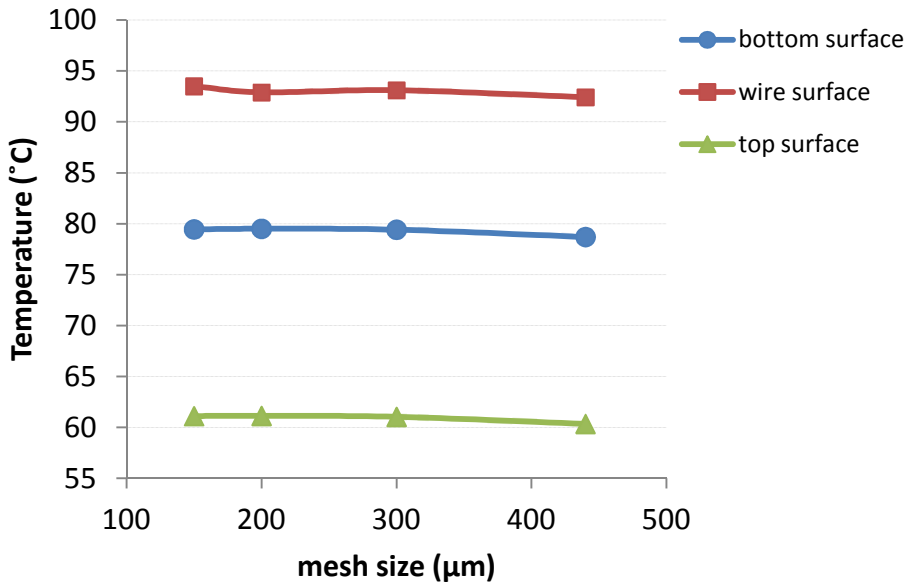

Figure C-11- Temperature changes of the bottom and top surfaces as well as wire surface with the mesh size for the transition region at the location of wire 2 (mesh number around the wires is 8).

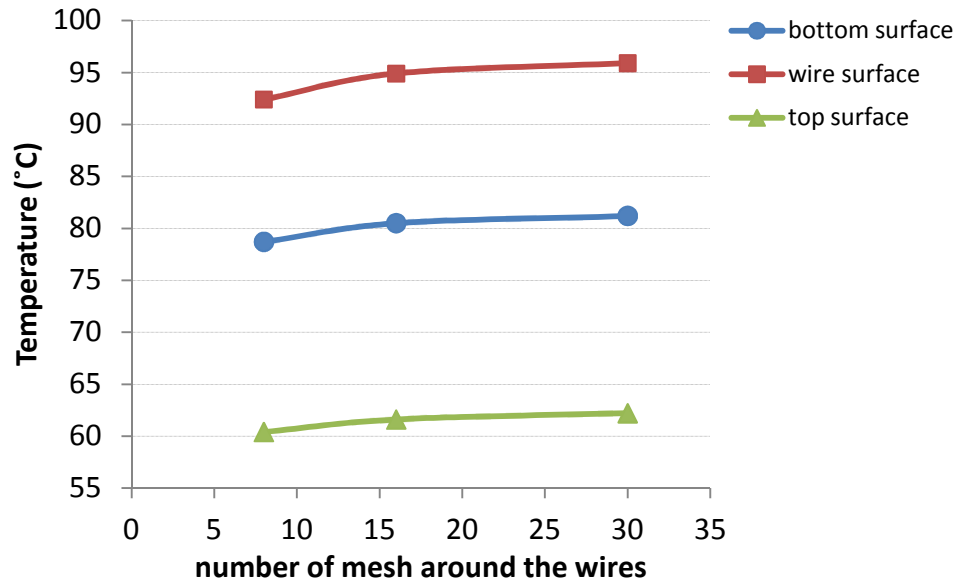

Figure C-12- Temperature changes of the bottom and top surfaces as well as wire surface with the number of mesh around the wires for the transition region at the location of wire 2 (the mesh size is 440µm).

Effect of mesh size on the temperature distribution of the transition region at the midpoint of wires 2 and 2-5, is presented in Table C-5 and Figure C-13 - Figure C-15. Table C-5 provides the temperature of the bottom and top surfaces, and mid thickness of the plate at the midway of wires 2 and 2-5. Temperature distributions along the plate thickness at midpoint of wires 2 and 2-5 is also presented in Figure C-13 for different mesh sizes. Figure C-14 and Figure C-15 represent the temperature changes of three points of the composite plate, i.e. bottom surface, mid thickness and top surface, as a function of the mesh size and the number of mesh around the wires, respectively. The mesh size in Figure C-15 is 440μm.

As can be seen in Table C-5 and Figure C-13 and Figure C-14, the mesh size does not affect the temperature distribution along the plate thickness. Figure C-15 shows that at the specific mesh size of 440μm, temperature of the three selected points of the plate increases by increasing the mesh number around the wires. Temperature of different points converges within ~0.7% for 16 and higher number of mesh around the wires.

Table C-5- Effect of the mesh size on temperatures of the bottom, and top surfaces as well as mid thickness of the plate for the transition region at the midpoint of wires 2 and 2-5.

Mesh size (μm) / **Distance from the bottom of plate(mm)**	**Temperature (˚C)**						
	440μm	**300μm**	**200μm**	**150μm**	**150μm-16 mesh around wires**	**440μm-30 mesh around wires**	**440μm-16 mesh around wires**
0.0 (bottom surface)	52.1	52.0	52.0	52.0	53.4	53.7	53.7
0.7 (mid thickness)	48.2	48.4	48.6	48.5	50.0	50.1	49.8
1.4 (top surface)	38.6	38.6	38.5	38.5	39.7	39.9	39.6

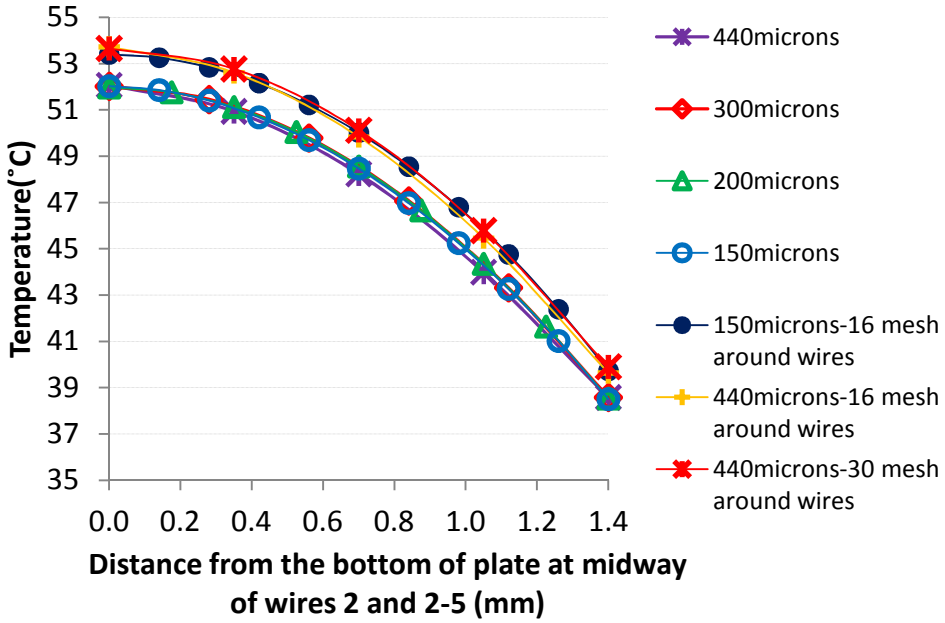

Figure C-13- Effect of the mesh size on temperature distribution along the thickness of transition region at the midpoint of wires 2 and 2-5.

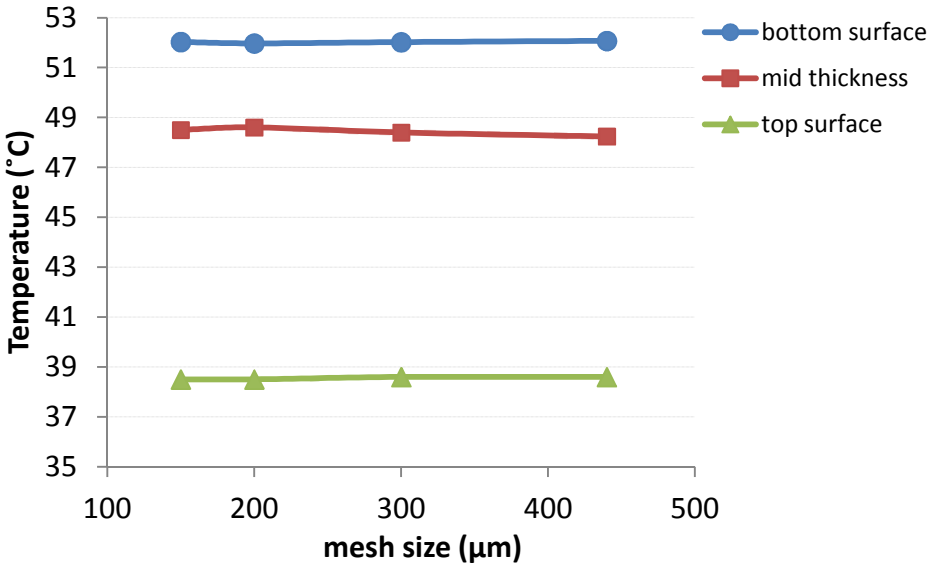

Figure C-14- Temperature changes of the bottom and top surfaces as well as mid thickness of the composite plate with the mesh size for the transition region at the midpoint of wires 2 and 2-5 (mesh number around the wires is 8).

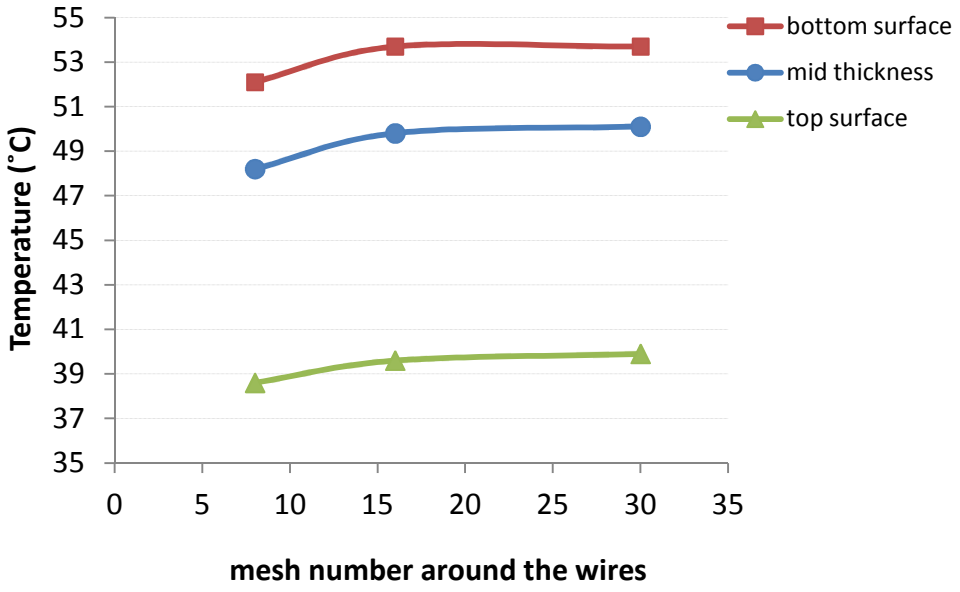

Figure C-15- Temperature changes of the bottom and top surfaces as well as mid thickness of the composite plate with the number of mesh around the wires for the transition region at the midpoint of wires 2 and 2-5 (the mesh size is 440μm).

The same results were observed for the modeled leading edge and beyond transition regions with different mesh sizes. These results show that the mesh size does not affect the temperature of the composite plate; and the temperature of different points converges within maximum ~1% for 16 and higher number of mesh around the wires.

C.6 Effect of the embedded thermal elements' position on the surface temperature distribution of the airfoil with anti-icing system

To investigate the effect of the thermal elements' position on the temperature profile, surface temperature distribution of the airfoil and temperature of the thermal elements' surfaces, a simulation was performed for the airfoil with embedded thermal elements positioned close to the airfoil surface. In these simulations, all the modeling parameters are the same as before, and only the positions of the thermal elements were changed from

the middle of the airfoil thickness to the possible closest location to the airfoil's surface, i.e. 105μm under surface.

The modeled temperature profiles of the three regions of the airfoil with the new position of thermal elements are shown in Figure C-16. The left panels in Figure C-16 show temperature distributions with individualized, coloring scale to give details; whereas, panels on the right have the same coloring scale to facilitate temperature comparisons between different regions.

By comparing the temperature information from Figure C-16 with Figure C-6, it can be seen that the temperature of the thermal elements' surfaces decreases when the thermal elements are positioned close to the airfoil surface. The hottest point of the thermal elements' surface is 104.6˚C in the leading edge region shown in Figure C-16(a), in comparison with 127.6˚C in Figure C-6(a).

As can be seen in Figure C-16, the temperature difference between the hottest and coldest spots on the airfoil surface at different location of each of the three regions is ~46˚C for the leading edge, ~45˚C for the transition region, and ~52˚C for beyond the transition region of the airfoil, respectively. Comparing the above temperature differences with those of Figure C-6, in which the thermal elements located at the mid plate of airfoil thickness, shows that surface temperature distribution is less uniform in the airfoil with the thermal elements positioned close to the airfoil surface. This is verified by comparison of modeled surface temperature of composite airfoil with different locations

of thermal elements relative to the airfoil's surface, presented in Figure C-17. In Figure C-17 the peaks represents the surface temperature on top of the wires and the valleys show the surface temperature of the midpoints between the wires. Diamond and star symbols represent the location of thermal elements in the mid thickness of the airfoil and close to the airfoil's surface, respectively. As can be seen in Figure C-17, surface temperature of the airfoil on top of the wires increases by locating the wires close to the airfoil surface; while, airfoil surface temperature on the midpoints between the wires relatively decreases for the airfoil with the wires close to the surface.

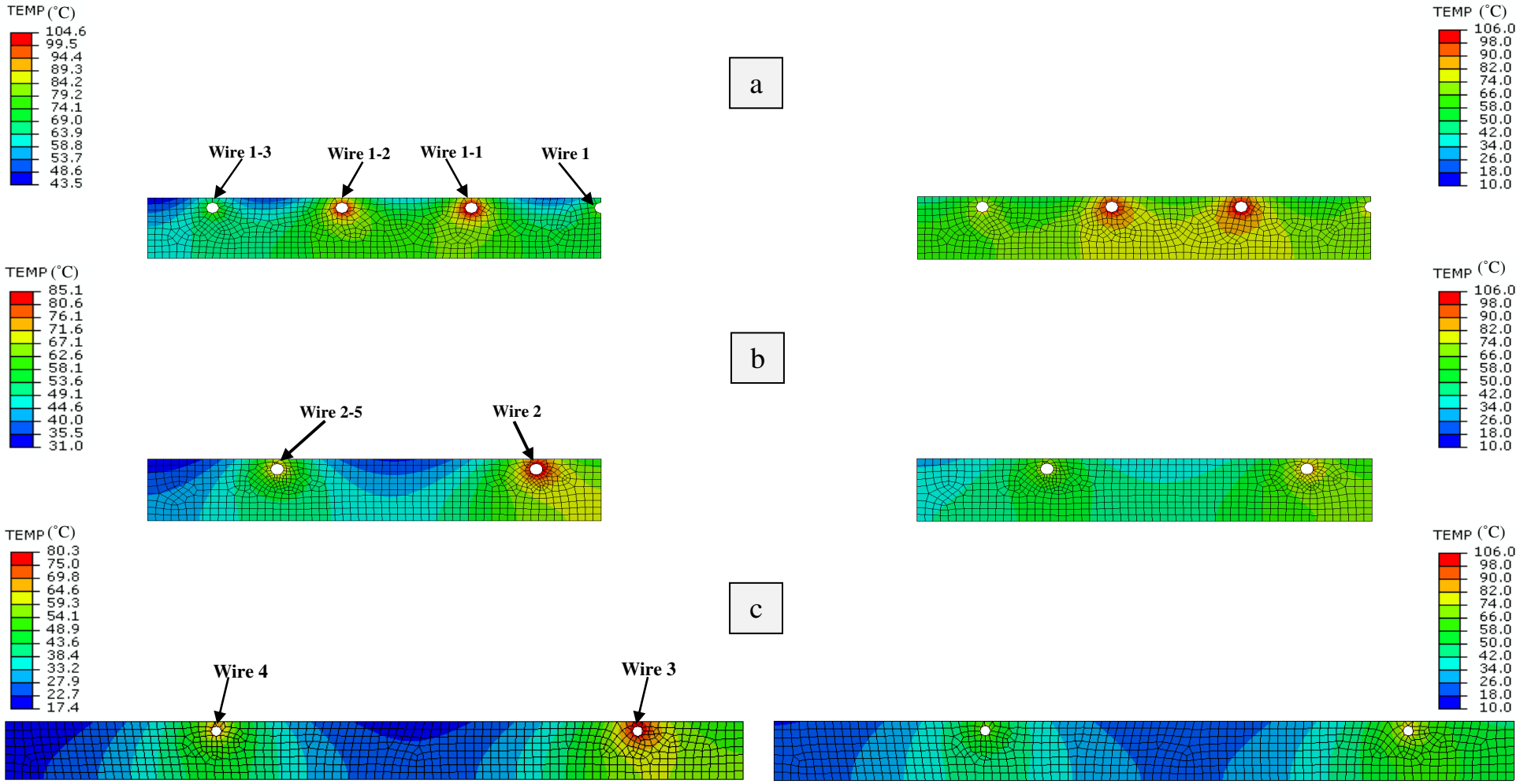

Figure C-16- Temperature distribution profile of the airfoil insert with thermal elements close to the airfoil's top surface, (a) leading edge region, (b) transition region, (c) beyond transition region; panels in the left show temperature distributions with individualized, coloring scale to give details; whereas, panels on the right have the same coloring scale to facilitate temperature comparisons between different regions.

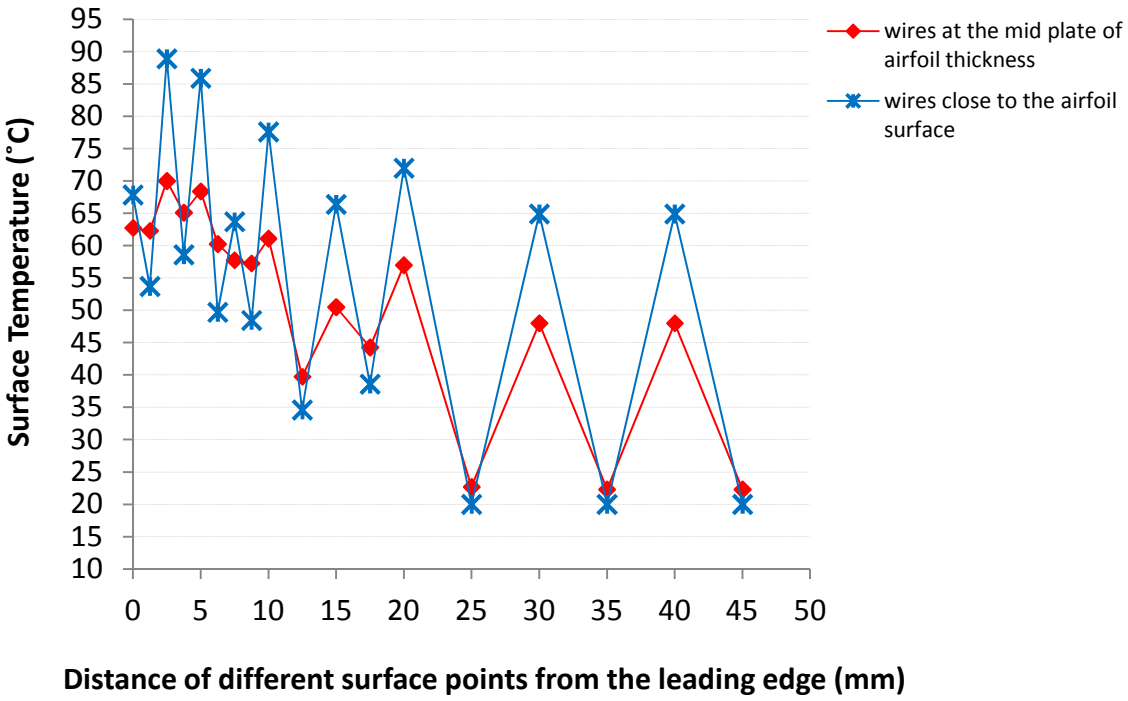

Figure C-17- Comparison of modeled surface temperature of composite airfoil with different locations of thermal elements relative to the airfoil's surface; diamond and star symbols represent the location of thermal elements in the mid thickness of the airfoil and close to the airfoil's surface, respectively. Lines are to guide the eye.

Generally, embedding the thermal elements close to the airfoil surface decreases the thermal elements temperature, which is safer for polymer composite material. But it provides a less uniform surface temperature with hot and cold spots on the airfoil's surface, which deteriorates the performance of the anti-icing system of the composite airfoil.

C.7 Conclusion

The simulated temperature profile of the composite airfoil with the ant-icing system is in a good agreement with the experimental data, and they are in the range of the measured

surface temperature of the airfoil in the experimental setup. So, this modeling can be used to model the behavior of the anti-icing system with different patterns and power levels; which can lead to optimize the thermal elements' pattern and amount of power level applied to the anti-icing system.

The modeled temperature profile of the anti-icing system can also be used to determine the power threshold in cold (dry) condition to prevent thermal degradation of the polymer composite due to the overheating. The simulated surface temperature of the thermal elements with different input power levels showed that all of the applied powers to different thermal elements in the anti-icing system are below the maximum working temperature of the composite material, and they are safe for the polymer composite airfoil.

The surface temperature distribution of the composite airfoil with the embedded thermal elements close to the airfoil surface is less uniform than the airfoil with the thermal elements in the middle of the airfoil thickness. So, an airfoil, with the anti-icing system embedded in the middle of the airfoil thickness, has a better performance in icing conditions.

In general, ABAQUS modeling of the composite airfoil with the anti-icing system showed that surface temperature of the airfoil can be controlled by thermal elements' pattern (spacing and location) and power input. The simulated temperature obtained in ABAQUS modeling was used to optimize the thermal elements' pattern and power input

in order to have a more uniform airfoil's surface temperature, and prevent overheating of the composite material.

C.8 References

[1] T. Horn, "Phenomenological investigation of the influence of superhydrophobic surfaces on icing", Institute of Technical Thermodynamics, Department of Mechanical Engineering, Technical University of Darmstadt, Conducted under the supervision of Prof. Alidad Amirfazli, Department of Mechanical Engineering, University of Alberta, MSC thesis, 2008.

[2] R. Elangovan, R. F. Olsen, 2008, "Analysis of layered composite skin electro-thermal anti-icing system", 46th AIAA Aerospace Science Meeting and Exhibition, Reno, Nevada, Paper No. AIAA-2008-0446.

[3] H. Sogin, "A design manual for thermal anti-icing systems", WADC Technical Report 54-313, December 1954.

[4] L. M. Boelter, L. M. Grossman, R. C. Martinelli, E. H. Morrin, "Investigation of aircraft heaters: comparison of several methods of calculating heat losses from airfoils", NACA TN 1453, 1948.

[5] X. Wang, "Convective heat transfer and experimental icing aerodynamics of wind turbine blades", University of Manitoba, PhD thesis, August, 2008.

[6] Y. A. Çengel, "Heat and mass transfer: a practical approch", McGraw-Hill, 3rd ed., 2007, Chap.7.

[7] G. Lubin, S. T. Peters, "Handbook of composites", Chapman & Hall, 2th ed., 1998, Chap. 3.

[8] M. J. Assael, K. D. Antoniadis, I. N. Metaxa, 2009**,** " Measurements on the enhancement of the thermal conductivity of an epoxy resin when reinforced with glass fiber and carbon multiwalled nanotubes", J. Chem. Eng. Data*,* 54, pp. 2365–2370.

[9] Y. Gowayed, J. C. Hwang, 1995, "Thermal conductivity of composite materials made from plain weaves and 3-D weaves", Composites Eng., 5, pp.1177-1186.

Appendix D

D. Contextualization of the Test Conditions, Power Consumption and Similitude

D.1 Icing condition

For a particular application, conditions where icing can take place are wide and varied. Also, type of application, i.e. in either aviation or wind turbine industry, is a compounding factor which leads to even more possible conditions were icing can occur. The main goal of our study was to develop a new anti-icing system for composite airfoils regardless of their application; and investigate their performance in an icing condition where ice forms, regardless of what conditions has led to formation of the ice.

There are different icing test conditions for wind turbine blades and aircraft wings in literature [1- 6]. We selected an icing condition representing a very severe icing event (see FAR29, Appendix C-Icing certification for icing condition requirements) to investigate the anti-icing performance in harsh icing condition. The icing condition used in our experiments can be representative of a very severe icing condition for wind turbine blades.

Icing conditions depend on meteorological events and change annually in different parts of the world. So, type of ice accumulation changes due to these weather changes. There are different types of atmospheric icing condition related to wind turbine including in-

cloud icing, icing precipitation including wet snow and freezing rain, and frost [1, 2, 7]. Ice accretion and type of ice depends on many different parameters such as liquid water content (LWC), drops size (median volume diameter-MVD), air temperature, wind speed, barometric pressure, and altitude. Also, the ice that forms on a wind turbine blade is dependent on the chord length of the blade, and temperature of the blade surface [1, 7]. In our particular icing test setup, the icing parameters were selected based on the operational limits of the test facility and limitation of the airfoil test specimen geometry.

D.2 Power consumption

The amount of power consumption of the icing mitigation techniques depends on the type of the mitigation system, i.e. anti-icing or de-icing systems, and the icing condition, as well as the airfoil profile and type of application of the airfoil either in wind turbine or aerospace industries. The total power applied to composite airfoil (II) in this study was ~118.7W, and the power intensity was ~8.3kW/m^2. The total applied power to airfoil (II) is lower than the 131.8W input power to heat an aluminum airfoil with the same dimension at the same icing condition to prevent ice accretion [8].

Elangovan and Olsen [5] modeled a layered composite skin electro-thermal de-icing system on a 36 inch chord NACA0012 airfoil. They modeled the system in two icing conditions at -6.7˚C and -17.8˚C under the air velocity of 89.4m/s and 0.39g/m^3 LWC. They found that the average power requirement for de-icing at -6.7˚C ambient temperature was ~5kW/m^2, and the average power requirement at -17.8˚C ambient temperature was ~7.8kW/m^2 [5].

Fortin et al. [9] used Kapton heating elements with a wattage density of 15.5kW/m^2 as a de-icing system for Aeronautics 63-415 airfoil with 0.2m of chords to simulate a 1.8MW wind turbine blade. They tested the airfoil with de-icing system in an icing condition with 0.2g/m^3 LWC, and 0.22microns MVD at air temperature of -10˚C and wind speed of 8m/s. The authors found that the energy required for de-icing the leading edge is twice than that of trailing edge; and 3.7 more power is required to de-ice the leading edge at the tip of blade than at the hub. They reported that the required power to de-ice the leading and trailing edges of three specific sections of the blade are 7.3 watts an hour per square meter (27% of the rotor radius), 13.7 watts an hour per square meter (43% of the rotor radius) and 24.3 watts an hour per square meter (56% of the rotor radius) which corresponds to 13.7% of the produced energy by the wind turbine [4].

Recent studies show that the power consumption of an electrical anti-icing system for 100-220kW wind turbines is between 6% and 12% of the nominal power output [7]. Other studies reported even lower level of power consumption for de-icing systems for wind turbines as low as 2% of nominal power output with a maximum of 6% of the nominal power [3, 7].

D.3 Dynamic similarity

As mentioned before, the main focus of this study was developing a new anti-icing system for a composite airfoil, without the initial tension of scaling the obtained results for actual wind turbines or aircraft's wing. Nevertheless, it is possible to determine how the results of this study can be scaled up to a full-scale wind turbine blade.

Dynamic similarity for airfoils exists when the Reynolds numbers and Mach numbers of the experimental and actual conditions are equal. For wind turbine blades the maximum Mach number is lower than 0.3 [3, 4, 9], so one can assume an incompressible flow for wind turbine analysis. As a result, Mach number does not need to be considered, and only Reynolds number is important for dynamic similarity. In the Reynolds number, only characteristic length should be compared between the experimental and actual conditions. Since the experimental conditions simulate a harsh actual condition for a wind turbine blade, so the parameters for the air conditions would be equivalent in the experimental and actual conditions. Comparing the approximated average chord length of an actual wind turbine blade, 1.68m [1], with the chord length of the airfoil test specimen in our experiments, 0.146m, shows that the airfoil test specimen is scaled down 11.5 times smaller than the actual turbine.

Therefore, for existing dynamic similarity for our experiments, i.e. equivalent Reynolds number, the air velocity in the wind tunnel in the experimental conditions, i.e. 27.7m/s, should be reduced by a factor of 11.5 to represent the actual wind velocity for the actual turbine. So, the evaluated anti-icing performance of the airfoil in the icing condition in the wind tunnel at 27.7m/s would actually represent the performance of the anti-icing system at wind speed of 2.41m/s on actual wind turbine blade.

D.4 References

[1] A. G. Kraj, E. L. Bibeau, 2010, "Phases of icing on wind turbine blades characterized by ice accumulation", Renewable Energy, 35, pp. 966-972.

[2] X. Wang, "Convective heat transfer and experimental icing aerodynamics of wind turbine blades", University of Manitoba, PhD thesis, August 2008.

[3] G. Fortin, J. Perron, 2009, "Wind turbine icing and de-Icing", 47th AIAA Aerospace Sciences Meeting, Orlando, Florida, Paper No. AIAA-2009-274.

[4] G. Fortin, C. Mayer, J. Perron, Sep. 2008, "Icing wind tunnel study of a wind turbine blade deicing system", Sea Technol., 49, pp. 41-44.

[5] R. Elangovan, R. F. Olsen, 2008, "Analysis of layered composite skin electro-thermal anti-icing system", 46th AIAA Aerospace Science Meeting and Exhibition, Reno, Nevada, Paper No. AIAA-2008-0446.

[6] C. Antonini, M. Innocenti, T. Horn, M. Marengo, A. Amirfazli, 2011, "Understanding the effect of superhydrophobic coatings on energy reduction in anti-icing system", Cold Reg. Sci. Technol., 67, pp. 58-67.

[7] O. Parent, A. Ilinca, 2011, "Anti-icing and de-icing techniques for wind turbines: critical review", Cold Reg. Sci. Technol., 65, pp. 88-96.

[8] M. Innocenti, "Superhydrophobic coating for mitigating icing of airfoils", University of Bergama, M.Sc. thesis, March 2009.

[9] O. Ceyhan, 2012, "Towards 20MW wind turbine: high Reynolds number effects on rotor design", 50th AIAA ASM Conference, Nashville, Tennessee, USA.

Appendix E

E. Image Processing

As mentioned in Section 4.2.2.2, an algorithm in MATLAB was developed to process the IR images automatically for detecting ice on the airfoil surface during icing test period. We have done an investigation where a number of images have been compared with one another when processed using different strategies and image processing functions as described in Section 4.2.2.2.

In the image processing procedure steps, it was found that applying median filtering is effective in reducing noises in the IR images. The effectiveness of median filtering is shown in Figure E-1 which shows a comparison of the edge detected IR images with and without applying median filtering. As shown in Figure E-1(b), detected edges due to IR image noises were decreased by applying median filtering, compared with Figure E-1(a).

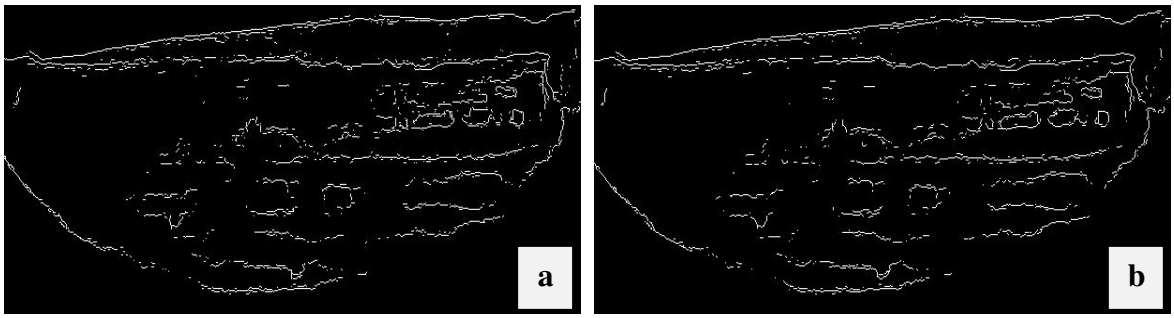

Figure E-1- Effect of median filtering on the edge detected IR image of airfoil (I) surface at 110th second of icing test period: (a) without applying "medfilt2" function, (b) with applied "medfilt2" function.

For removing the IR images noises, we applied two filters of “medfilt2” and “imfilter”. As mentioned in the image processing procedure steps, “medfilt2” function was more effective in removing noises than “imfilter” function. This is shown in Figure E-2. A comparison between the output images, as depicted in Figure E-2, showed that edge detected IR images with applied “medfilt2” function (Figure E-2 (a))has less noises than images with “imfilter” function (Figure E-2 (b)). This implies that “medfilt2” function was more efficient in removing noises than “imfilter” function.

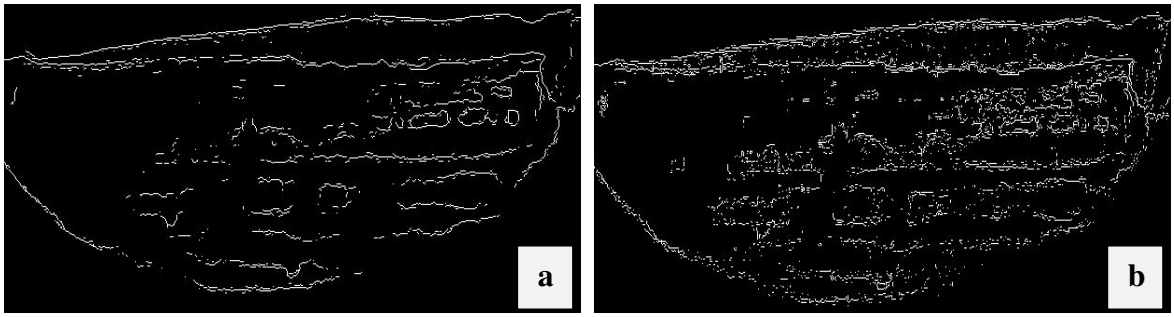

Figure E-2- Comparison of different filtering functions applied to the IR image of airfoil (I) surface at 110th second of icing test period: (a) edge detected with applied “medfilt2” function, (b) edge detected with applied “imfilter” function.

As mentioned in Section 4.2.2.2,the IR images contrast were enhanced using two image enhancing functions of “histeq” and “imadjust”. A comparison between the output edge detected images from the enhanced IR images by “histeq” and “imadjust” functions is depicted in Figure E-3. As can be seen in Figure E-3 (a) and (b), “histeq” function is more effective in enhancing IR image contrast than “imadjust” function; as such, the boundary of major icing was detected better in the IR images enhanced by “histeq” function.

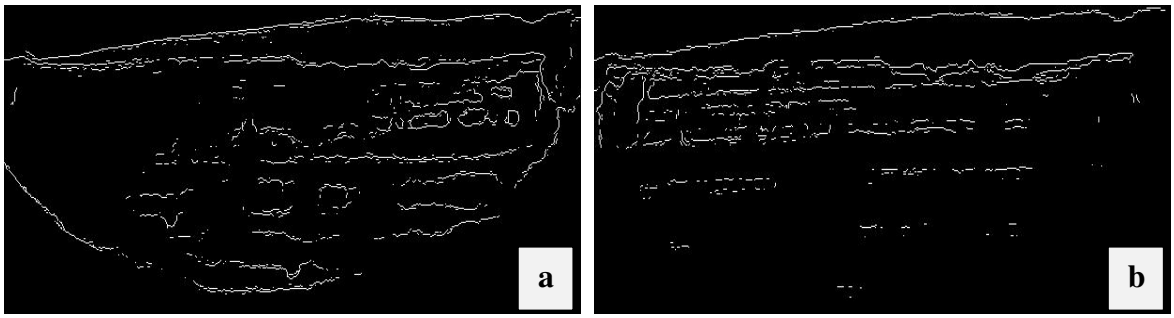

Figure E-3- Comparison of different image enhancing functions applied to the IR image of airfoil (I) surface at 110th second of icing test period: (a) edge detected enhanced image with "histeq" function, (b) edge detected enhanced image with "imadjust" function.

As explained in Section 4.2.2.2, for detecting iced regions on the IR images, different edge detection operators including Roberts, Canny, and Sobel were used. IR image of airfoil (I) surface at 110th second of icing test period was processed using different edge detection operator to compare their effectiveness in detecting the boundary of major icing (Figure E-4). As can be seen in Figure E-4 (a), where Roberts operator was applied, the detected edges due to noises is more than that of Figure E-4 (b) and (c) which verifies that Roberts operator is sensitive to noises. In Figure E-4 (b) all types of edges, i.e. strong and weak edges, were detected by Canny operator. As a result, the boundary of major icing on leading edge region of the airfoil is not as clear as Figure E-4 (c) (Sobel operator), since Canny operator detects both the strong and weak edges. Comparison of images in Figure E-4 shows that Sobel operator (Figure E-4 (c)) can provide a cleaner edge detected image than that of Roberts and Canny operators ; and it can detect the boundary of major icing better in noisy IR images than the other edge detection operators.

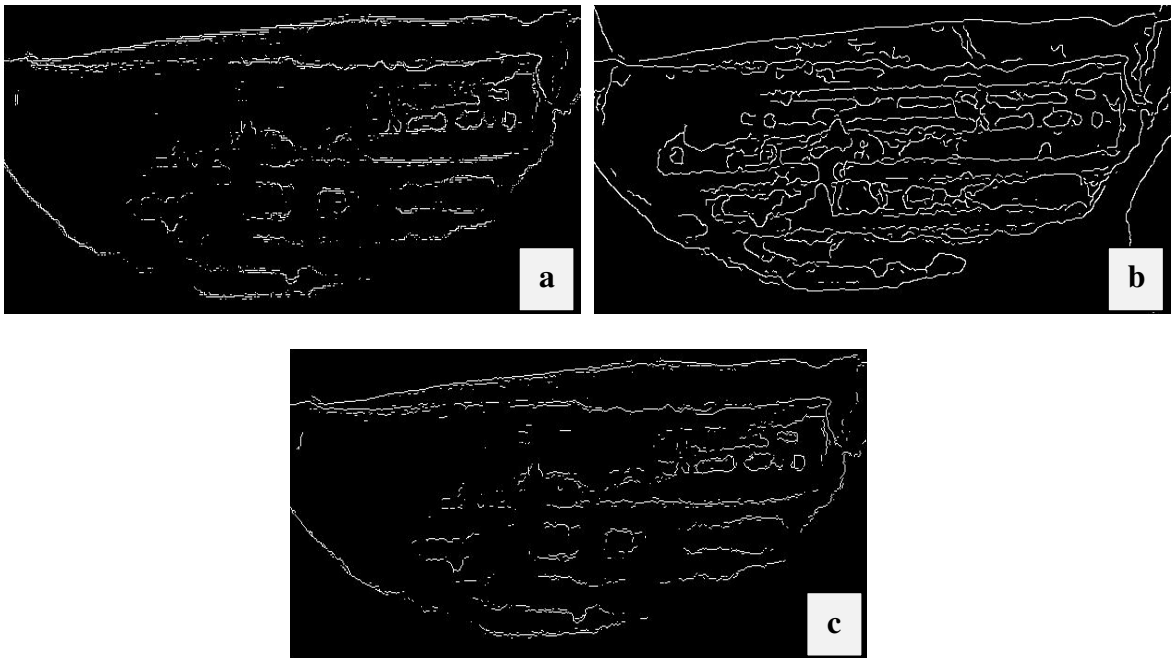

Figure E-4- Comparison of different edge detection operators applied to the IR image of airfoil (I) surface at 110th second of icing test period: (a) Roberts operator, (b) Canny operator, (c) Sobel operator.

Appendix F

F. Mold Drawings

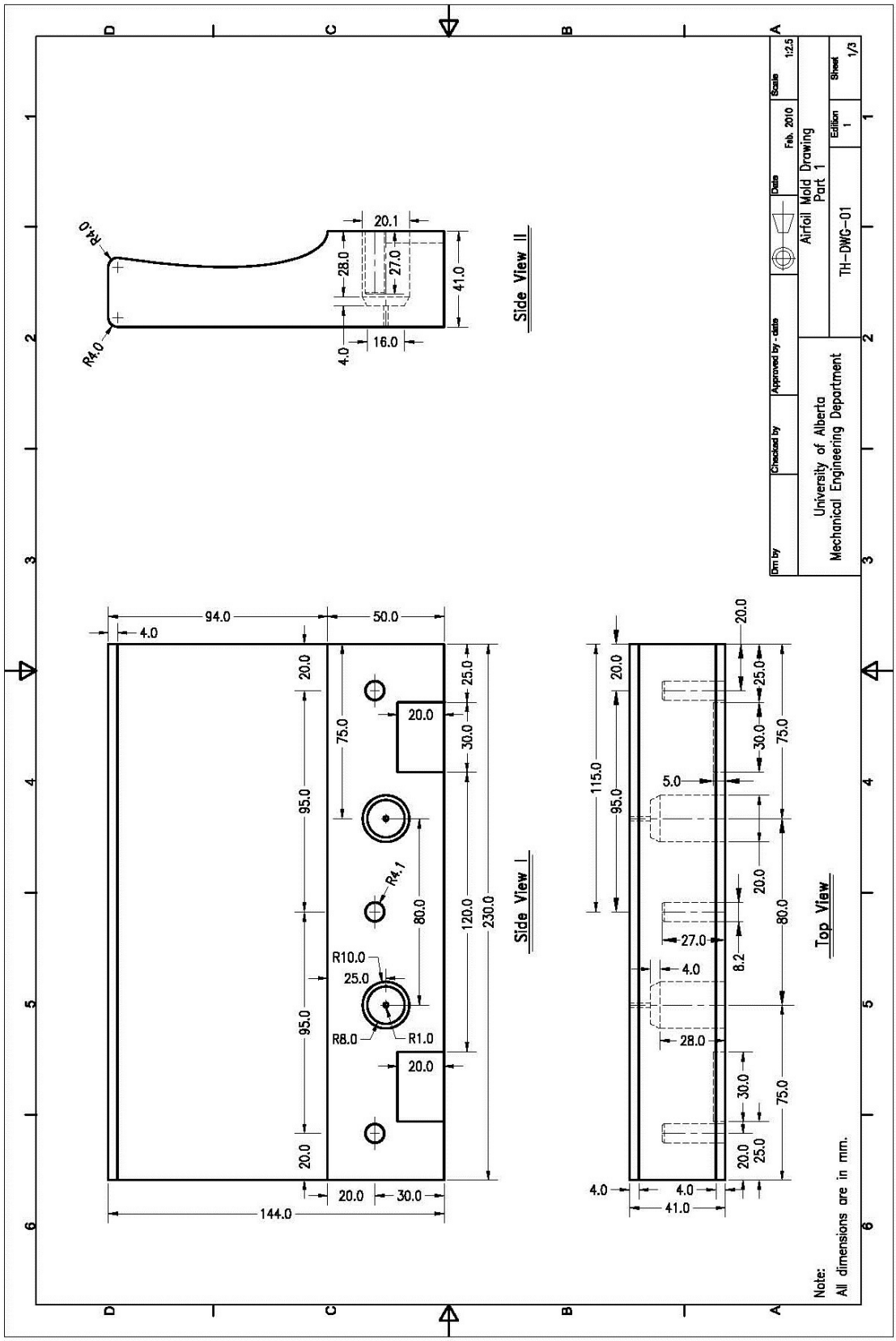
Side View II
Side View I
Top View
Airfoil Mold Drawing
Part 1
TH-DWG-01
University of Alberta
Mechanical Engineering Department
Note:
All dimensions are in mm.

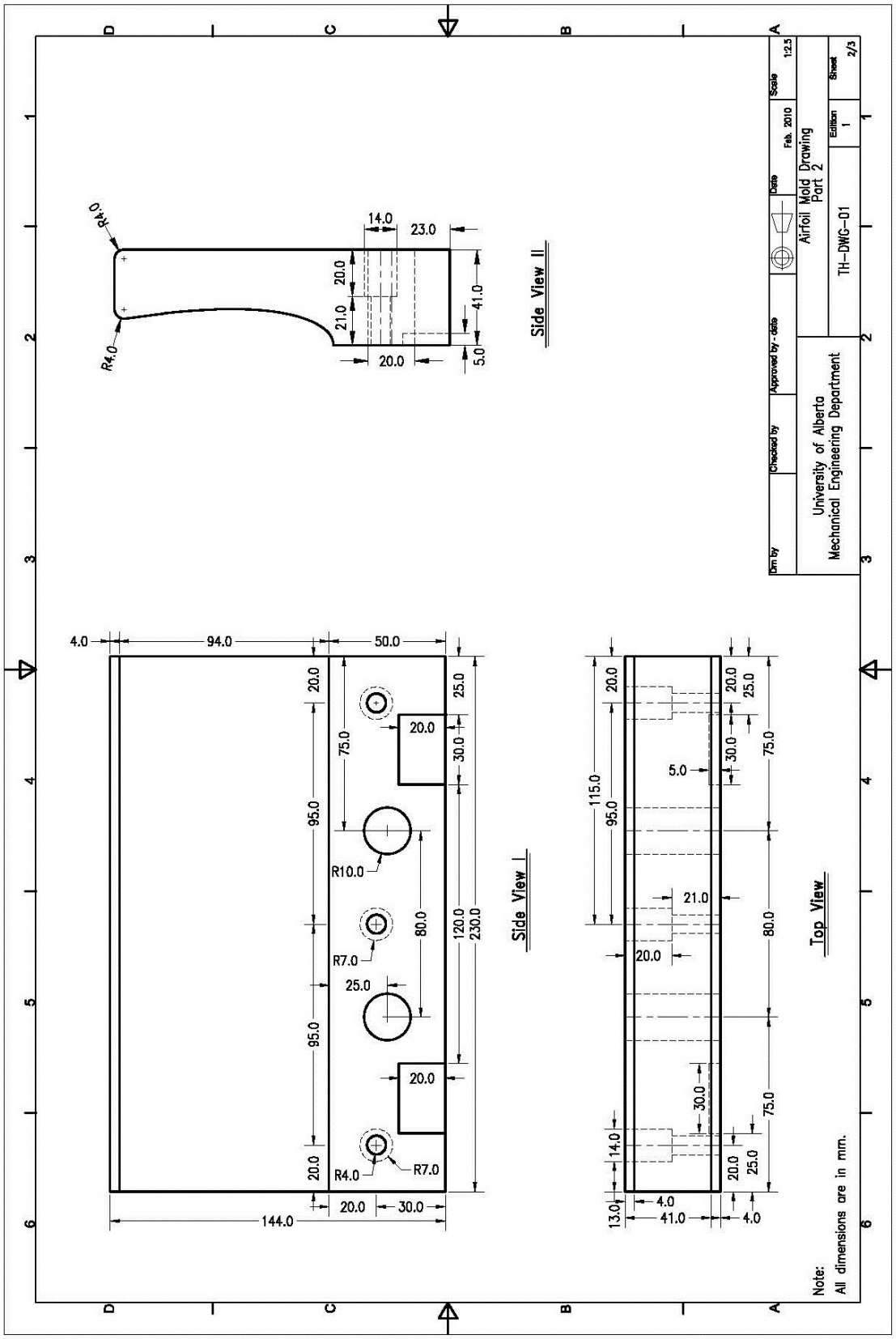
Side View II
Side View I
Top View
Airfoil Mold Drawing
Part 2
TH-DWG-01
University of Alberta
Mechanical Engineering Department
Note:
All dimensions are in mm.

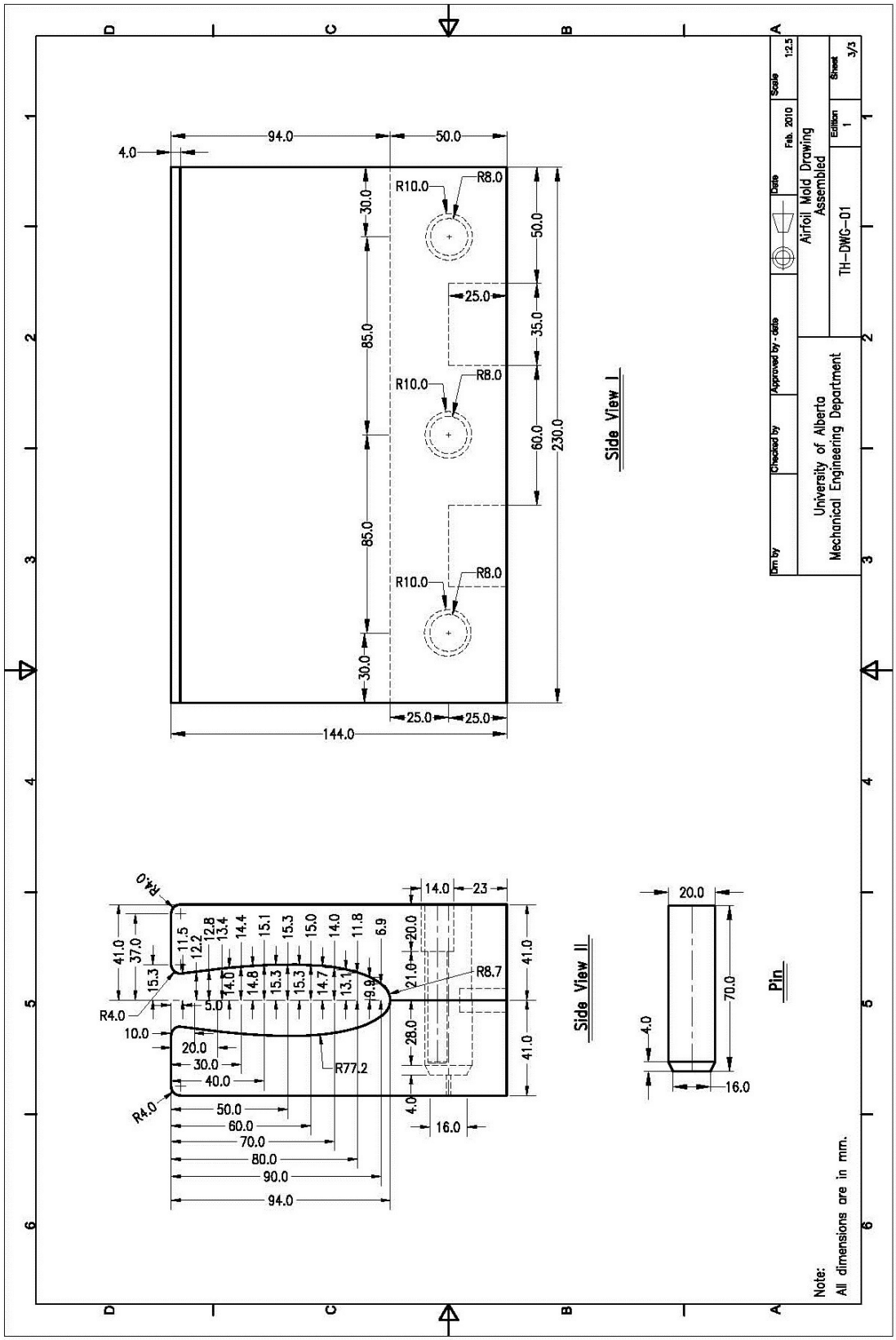
Airfoil Mold Drawing
Assembled
University of Alberta
Mechanical Engineering Department
TH-DWG-01
Scale 1:2.5
Date Feb. 2010
Edition 1
Sheet 3/3
Dm by
Checked by
Approved by - date
Side View I
Side View II
Pin
Note:
All dimensions are in mm.